CONSTITUENT PHASES AND THEIR STABILITY IN A MULTI-PRINCIPAL ELEMENT ALLOY FILLER FOR BRAZING OF NICKEL-BASE SUPERALLOYS

by

Benjamin T. Schneiderman

A thesis submitted to the Faculty and the Board of Trustees of the Colorado School of Mines in partial fulfillment of the requirements for the degree of Doctor of Philosophy (Metallurgical and Materials Engineering).

Golden, Colorado

Date _____

Signed: _____

Benjamin T. Schneiderman

Signed: _____

Dr. Zhenzhen Yu
Thesis Advisor

Golden, Colorado

Date _____

Signed: _____

Dr. Ivar Reimanis
Professor and Department Head
Metallurgical and Materials Engineering

ABSTRACT

Brazing is one alternative for joining and repair of nickel-base superalloys, in which only a filler material is melted, and filling of a joint-gap or crack is accomplished via surface wetting and capillary action while the base material remains solid. Design constraints on melting temperature and chemical compatibility with the base material guide the selection of a filler alloy composition. An ideal filler should minimally alter the microstructure of the nickel-base superalloy component at the braze site, particularly avoiding the introduction of potentially detrimental non-native constituent phases. The most common filler alloys in contemporary industrial use employ boron and silicon as melt-point depressants, which often introduce embrittling boride and/or silicide particles, and therefore fall short of this objective.

A multi-principal element alloy (MPEA) filler was investigated in this work as a novel alternative. Through a suite of computational strategies considering melting temperature, calculated phases, and interactions with nickel-base superalloy substrates, this MPEA was selected from a composition subspace that is robust in the stability of a single, disordered FCC solid solution. It was therefore hypothesized that use of this filler would render the introduction of detrimental non-native phases to the braze-repair site avoidable. To evaluate this hypothesis, it was important to consider the filler's tolerance to compositional change driven by dilution (i.e., mixing with the base material) at the immediate point of brazing, as well as the thermal phase stability following both short-term and long-term exposures to high-temperature operating conditions.

Synchrotron X-ray diffraction is ideally suited to assess and map constituent phases in a complex brazed microstructure because it offers site-specific structure characterizations at the micron-scale and can detect low volume-fraction constituents. Nevertheless, an MPEA filler as a complex, concentrated alloy exhibits deviations from powder-pattern intensities in as-solidified microstructures and stoichiometric deviations from pure phases, leading to significant challenges in assessing the microconstituents using a conventional Rietveld refinement or strategies based in the powder diffraction file. To overcome these challenges, a novel analytical methodology was developed that synthesizes thermodynamic simulations, existing literature data for crystal structures, and experimental diffraction data coupled with supplemental scanning electron microscopy characterizations.

Employing this methodology, experimental investigations were conducted using both Alloy 600 and Alloy 738LC as base materials, to respectively highlight brazing of a solid solution

strengthened nickel alloy and a precipitate strengthened nickel alloy with greater industrial relevance. The major constituent phase in either braze was a single, disordered FCC solid solution. The absence of intermetallic phases indicated tolerance of the filler to dilution-driven compositional changes, despite the introduction of seven new elemental species to the filler in the case of the Alloy 738LC braze. The only non-native phases introduced to the as-brazed microstructures of either base material were oxides of Al, Cr, and Mn. The source of oxygen introduction was traced back to the laboratory-scale manufacturing conditions at the original MPEA casting step, indicating that oxide introduction is mitigable by employing more advanced manufacturing processes with better control of atmospheric elements. The only phase evolution detected during short-term high-temperature exposures was the precipitation and growth of additional Cr_2O_3 oxides, indicating that the MPEA filler possesses short-term thermal phase stability if its dissolved oxygen content can be reduced in manufacturing. Predictive assessments of the long-term phase stability of the MPEA filler using thermodynamic simulations indicated that the filler material is expected to outperform the base material in the long-term suppression of topologically close packed intermetallic phases.

Despite the presence of contaminant oxides, the as-brazed ductility of Alloy 600 brazes using the MPEA filler was ten times greater than that offered by a conventional boron-containing filler, with comparable strengths between the two fillers. Variations in total elongation among individual specimens were attributed to variations in the oxide size and distribution. Alloy 738LC brazes using the MPEA filler are also expected to exhibit ductile behavior due to the absence of brittle microconstituents, although the suppression of γ’ is expected to negatively impact strength. A mechanical performance assessment of Alloy 738LC brazes and the re-introduction of γ’ to this microstructure are identified as areas for future work.

TABLE OF CONTENTS

LIST OF FIGURES

LIST OF TABLES

LIST OF EQUATIONS

LIST OF SYMBOLS

Activation Energy ..... Q

Atomic Radius ..... r

Concentration C

Concentration – Base Material ..... C_{BM}

Concentration – Filler Zone ..... C_{FZ}

Concentration – Initial ..... C_0

Concentration – Liquidus ..... C_L

Concentration – Solidus ..... C_S

Configurational Entropy ..... ΔS_{config}

Diffusivity ..... D

Diffusivity Pre-Factor ..... D_0

Dilution ..... Dil

Enthalpy of Mixing ..... ΔH_{mix}

Entropy of Mixing ..... ΔS_{mix}

Gas Constant ..... R

Interlayer Half-Width ..... h

Interplanar Atomic Spacing ..... d

Lattice Parameter (Cubic) ..... a

Number of Elements ..... n

Number of Simulation Steps ..... N

Phase ..... ϕ

Phase Fraction ..... f

Position x

Reciprocal Lattice Vector ..... q

Temperature ..... T

Time ..... t

LIST OF ABBREVIATIONS

Active Braze Alloy ..... ABA
Advanced Photon Source ..... APS
Athermally Solidified Zone ..... ASZ
Body-Centered Cubic ..... BCC
Body-Centered Tetragonal ..... BCT
Boron and Silicon Suppressed Filler ..... BSSF
Complex Concentrated Alloy ..... CCA
Diffusion Affected Zone ..... DAZ
Digital Image Correlation ..... DIC
Energy Dispersive Spectroscopy ..... EDS
Face-Centered Cubic ..... FCC
Fully Melted ..... FM
Geometrically Close Packed ..... GCP
High Entropy Alloy ..... HEA
Inherently Low Melting Point ..... ILMP
Isothermally Solidified Zone ..... ISZ
Melting Point Depressant ..... MPD
Microvoid Coalescence ..... MVC
Multi-Principal Element Alloy ..... MPEA
Powder Diffraction File ..... PDF
Powder Metallurgy ..... PM
Scanning Electron Microscopy ..... SEM
Topologically Close Packed ..... TCP
Transient Liquid Phase ..... TLP
Ultimate Tensile Strength ..... UTS
Unmelted ..... UM
Vacuum Induction Melting ..... VIM
X-Ray Diffraction ..... XRD

ACKNOWLEDGEMENTS

This research was primarily supported by the National Science Foundation with Award No. 1847630. This research used resources of the Advanced Photon Source, a U.S Department of Energy (DOE) Office of Science User Facility operated for the DOE Office of Science by Argonne National Laboratory under Contract No. DE-AC02-06CH11357. Data was collected at Beamline 1-ID-E. Use of the Tescan S8252G SEM was supported by the National Science Foundation Division of Materials Research Award No. 1828454. PCC-Structurals, Inc. generously donated the nickel-alloy 738LC material used in this work.

I would like to extend my sincerest thanks to my thesis advisor, Dr. Zhenzhen Yu, for shaping my perspective on scientific research, and for her unlimited capacity to invest time and effort to help her students grow and succeed. She has been instrumental in the last five years of my development as a researcher. I would also like to thank the members of my thesis committee, Dr. Jonah Klemm-Toole, Dr. Amy Clarke, Dr. Kip Findley, and Dr. Garritt Tucker for their guidance and instruction. Other members of Mines faculty to whom I am grateful include Dr. Stephen Liu, for introducing me to the Center for Welding, Joining and Coatings Research, Dr. David Diercks and Dr. Brian Gorman, for their assistance in the electron microscopy laboratory, and Dr. Garrison Hommer, for his assistance in mechanical testing. Additional thanks are due to Scott Pawelka and Sarah Harling for their support on a variety of equipment issues. Outside of Mines, I offer very sincere thanks to Dr. Warren Miglietti for sharing his wealth of expertise pertaining to industrial braze repairs over the last year and his insights on the industrial impact of this project.

This work involved extensive use of the user facilities at Beamline 1-ID-E of the Advanced Photon Source, and support from the beamline staff was indispensably valuable. In particular, I would like to thank Dr. Andrew Chuang for his kind mentorship and collaborative feedback throughout the course of my graduate study. The assistance of Dr. Peter Kenesei and Dr. Jun-Sang Park was also greatly appreciated.

I would like to expressly thank all the students with whom I have collaborated directly on work in MPEA development. Particular thanks are due to Alex Hansen, whose industrial perspective and laboratory and management skill sets have been extremely valuable in this research and beyond. Other direct collaborations for which I am grateful include those with Olivia DeNonno, Abdelrahman Abdelmotagaly, Tushar Telmasre, and Aaron Wells. Additional

colleague relationships that I have cherished throughout my time in graduate school have been those with Michael Rupinen, Luc Hagen, Tim Pickle, Charles Smith, Rohit Bardapurkar, Dr. Ethan Sullivan, Dr. Cheryl Hawk, Dr. Byron McArthur, and Dr. Devon Gonzales, among many others.

Finally, I would like to thank all of my friends, teammates, coaches, and family that have made my 8.5 years as a student at Mines a wholeheartedly enjoyable and unforgettable experience. It is impossible to name all these people, but I'd especially like to acknowledge the 2019 Sacramento national champions Mines cross country team and everyone who was affiliated in the years before and since. And I owe the biggest thank you of all to my parents, Mary and Barry Schneiderman, and my brother Noah Schneiderman, for their enduring love and support.

CHAPTER 1
GENERAL INTRODUCTION

This chapter provides a brief overview of the relevance of phase stability considerations in the selection of candidate filler alloys for nickel-base superalloy braze repair and enumerates the hypothesis and research questions governing this thesis. For a more in-depth literature review of the industrial importance of this work and the current state-of-the-art in braze repair of nickel-base superalloys, the reader is referred to Chapter 2.

1.1 Relevance of Phase Stability in Ni-Base Superalloy Braze Repair Fillers

Nickel-base superalloys are an invaluable category of engineering materials that are often called upon for use in extreme operating environments. When Ni-base superalloy components suffer damage and/or cracking during operation, one possibility for salvage and return to service is braze repair, in which only a filler material is melted (*i.e.*, the base material remains solid) and crack filling is accomplished via surface wetting and capillary action. In commonly employed furnace brazing techniques, the entire assembly is held at a uniform temperature, offering the advantage of residual stress minimization. However, the necessity to melt the filler material at a temperature at which the base alloy is also fully solid requires the use of a filler of significantly disparate composition. Despite this compositional disparity, it is desirable to avoid the introduction of brittle, non-native microstructural constituent phases in braze repair, such that the thermomechanical performance of the repair site matches that of the base alloy as closely as possible. Ideally, it is also desirable that beneficial precipitate phases native to the Ni-base superalloy are retained in the braze. This set of constraints upon the behavior of a filler material necessitates careful consideration in the design of its composition.

Hypothetically, the introduction of non-native phases may occur as a direct result of the brazing process or as the result of continued microstructural evolution at the repair site at high temperatures following a return to service. As detailed in Chapter 2, transient liquid phase (TLP) processes represent the most widely adopted means to attempt to mitigate non-native phases at both of these potential points of introduction. Nevertheless, these processes, which employ fillers with boron and/or silicon as melt-point depressants, almost universally introduce some extent of brittle boride or silicide microconstituents directly during the brazing process. At least two

mechanisms exist by which this precipitation occurs, and one of these – diffusion affected zone formation – is particularly difficult to control. Among other brazing processes and filler categories, only brazing with gold-based filler materials consistently avoids non-native phase introduction, but the use of these fillers for high-volume industrial repairs is often cost-prohibitive.

Recent research has indicated *select* multi-principal element alloys (MPEAs) as potential filler materials for Ni-base superalloy braze repair. An important advantage of searching for filler compositions within the vast, largely unexplored MPEA composition space is the ability to tune the melting temperature range as desired by varying the identities and concentrations of the constituent elements. This ability renders the inclusion of extrinsic melt-point depressants such as boron and silicon unnecessary, such that boride and silicide phases are a non-issue. However, the propensity of an MPEA filler for the introduction of other non-native phases to the braze repair site must nonetheless be carefully evaluated and critically considered in composition selection. An MPEA subspace comprising 3d-transition metals as constituent elements has been argued to present manifestations of a hyper-dimensional face-centered cubic (FCC) single-phase field across a relatively broad set of compositions [1]. The FCC phase is most often a disordered solid solution exhibiting ductile behavior. The prototype $Mn_{35}Fe_5Co_{20}Ni_{20}Cu_{20}$ filler was designed from this composition subspace using a set of parameter-based criteria for phase selection, followed by a melting-temperature screening step using high-throughput solidification simulations [2, 3]. The objective of screening for an FCC solid solution is to match the FCC crystal structure of the γ constituent phase common to all Ni-base superalloys, and thus avoid the introduction of non-native phases.

To holistically evaluate the ability of an MPEA filler to avoid non-native phase introduction, it is necessary to consider the phase stability of the disordered FCC solid solution. In this context, *phase stability* is the ability of the solid solution to tolerate perturbations without precipitating (potentially detrimental) second phases. An important perturbation to consider is the introduction of additional elements to the filler and/or changes in the concentration of the original filler elements caused by interaction with the Ni-base superalloy substrate material. In other words, the ductile FCC solid-solution of the filler must be able to accommodate a *transit in composition space* while avoiding second-phase precipitation. Depending on the composition of the base material and the extent of filler/base interaction, this transit in composition space may be considerable. An additional perturbation that the solid-solution must tolerate is exposure to high-

temperature service conditions, at which any thermodynamically stable second phases may overcome kinetic barriers to precipitation. By assessing each of these phase stability considerations, it is possible to evaluate the extent to which an MPEA filler may offer enduring ductility in a Ni-base superalloy braze repair, which is uncommon among conventional fillers.

1.2 Governing Hypothesis and Research Questions

This thesis investigates critical aspects of the phase stability of the prototype MPEA filler in mock braze repairs of two significantly different Ni-base alloys: Alloy 600 and Alloy 738LC. To govern the work contained herein, the following hypothesis was proposed:

Hypothesis: The introduction of detrimental phases not native to Ni-base alloy materials is avoidable by the use of the selected MPEA filler, due to the extent of composition space favorable to the stability of a single, ductile disordered solid-solution phase over a broad temperature range (including fabrication, assembly, and service conditions).

To establish specific, targeted research aims, the following three research questions were developed:

Research Questions

1. Tolerance to Compositional Change: When brazing Ni-base alloys with the MPEA filler, how is the phase stability of the FCC solid solution affected by the *immediate* introduction of additional elements (i.e. composition-space transits) through interaction with the base materials?
2. Short-term Thermal Phase Stability: Over *short-term* (< 100 hr) exposures to industrially relevant operating temperatures, does precipitation of any non-native phases occur in the braze microstructures? If so, by what mechanisms?
3. Long-term Thermal Phase Stability: To what extent can thermodynamic modelling effectively predict constituent phases of the braze microstructures, and how does it characterize the relative ability of the filler and base materials to avoid detrimental phase precipitation in the *long term*?

The research questions are structured to acknowledge that falsification of the governing hypothesis could occur if second phase precipitation is observed across a range of time scales. The *immediate term* refers strictly to the brazing process itself, the *short term* refers to post-braze high temperature exposure on the order of 100 hours, and the *long term* refers to an appreciable fraction of the uptime of Ni-base superalloy engine components between maintenance cycles, which is on the order of 20,000 hours [4]. Both the immediate term and the short term lend themselves to experimental validation, while assessments of the long term must more heavily employ modelling techniques due to the resource-intensive nature of performing experiments of this duration.

1.3 Thesis Outline

Chapter 2 provides a comprehensive literature review of topics relevant to this thesis. The general categories of Ni-base alloys and the disparities between Alloy 600 and Alloy 738LC are noted, highlighting that brazes of Alloy 738LC represent a more industrially relevant case with relatively greater complexity. Braze repairs are compared to weld repairs for Ni-base alloys and the relative advantages of each are discussed. The existing categories of filler materials for braze repair are comprehensively reviewed, highlighting common failures in avoiding non-native phase introduction to the microstructure. A handful of studies taking alternative approaches to MPEA filler design are reviewed. Finally, the conceptualization of the prototype MPEA filler in this work is discussed in the context of the original 'high-entropy alloy' core postulates and current trends in metallurgical research pertaining to the diminishing acceptance of these postulates as universally applicable to MPEAs.

Chapter 3 contains work pertinent to Research Question 1 for brazes of Alloy 600. The effect of the immediate term composition-space transit on the MPEA filler phase stability is investigated by exploring tensile ductility in as-brazed specimens and examining fracture surfaces for potential second phase particles. For the sake of comparison, this work is presented alongside the same assessment for brazes employing a conventional boron- and silicon-suppressed filler, with key differences in the solidification mechanisms and resultant microconstituents between the two fillers discussed in depth.

Chapter 4 more completely addresses Research Question 1 for brazes of Alloy 600 and primarily focuses on Research Question 2 for these brazes. A more thorough constituent phase assessment is conducted in the as-brazed condition using site-specific synchrotron X-ray

diffraction (XRD) mapping, completing the assessment of the immediate term phase stability for the MPEA filler on Alloy 600. This same technique is employed, in conjunction with mechanical testing and fracture surface evaluation, on specimens subjected to short term high temperature exposures. In these experiments, the role of oxygen stemming from MPEA manufacturing conditions and its implications for Research Question 2 are evaluated.

Chapter 5 serves multiple functions within this thesis. On one level, this chapter provides a holistic methodology for characterizing the constituent phases present in any newly fabricated complex concentrated alloy composition. This category of alloys includes the MPEA filler alone, Ni-base alloy substrates alone, and mixtures of these materials in varying ratios. The methodology combines thermodynamic simulations with an approach to analyzing high energy synchrotron XRD data in non-powder patterns. This work is foundational for assessing the constituent phases of brazes in the as-brazed condition and following short-term heat treatments, and thus supports the evaluation of both Research Question 1 and Research Question 2 for brazes of both Alloy 600 and Alloy 738LC. Directly, this chapter also explores the introduction of Alloy 738LC elements to the MPEA filler by characterizing laser-welds between these two materials at varying dilution levels. This aspect of Chapter 5 serves to investigate Research Question 1 for brazes of Alloy 738LC, albeit under differing solidification conditions. Finally, because the methodology described in this chapter incorporates thermodynamic modelling and makes comparisons to experimental observations, the aspect of Research Question 3 that deals with the effectiveness of this modelling is also investigated.

Chapter 6 provides the most direct assessment of Research Questions 1, 2, and 3 for brazes of Alloy 738LC. Building upon the methodology presented in Chapter 5, a constituent phase assessment is presented for brazes of Alloy 738LC in the as-brazed condition and following short-term heat treatments, supporting Research Questions 1 and 2. The relative effects of liquid-phase dilution during brazing and solid-state interdiffusion during heat treatment in driving composition-space transits in the solid solution of the MPEA are compared. A high-throughput implementation of equilibrium thermodynamic modelling is used to explore the site-specific propensity for second-phase precipitation across the composition profile of the braze. This investigation focuses both on beneficial γ' phase and the detrimental σ phase and informs the relative propensity of both the base-material and filler zones to precipitate these phases given unlimited time. This probe relates directly to Research Question 3.

Chapter 7 re-visits the research questions and summarizes the key conclusions drawn from this work. Chapter 8 offers recommendations for several areas of future work necessary to further the understanding of the industrial applicability of an MPEA filler for Ni-base alloy braze repair.

CHAPTER 2
BACKGROUND AND LITERATURE REVIEW

This chapter provides a literature review of the industrial importance of Ni-base superalloy braze repair, an overview of both conventional and novel repair filler alloys, and a reflection on prior work conducted on a particular novel multi-principal element alloy (MPEA) filler, establishing the necessary context for the governing hypothesis and research questions posed in Chapter 1.

2.1 Nickel-Base Superalloys Background

Nickel-base superalloys are widely utilized for high temperature structural members that require good corrosion resistance. One of the most prominent applications for these alloys is in gas turbine engines employed in both the aerospace and power generation industries [5]. Figure 2.1 highlights some of the critical components in a typical gas turbine engine that require Ni-base superalloys [6]. Other applications include corrosion-sensitive components in the oil and gas industry [7], as well as cryogenic service [8, 9].

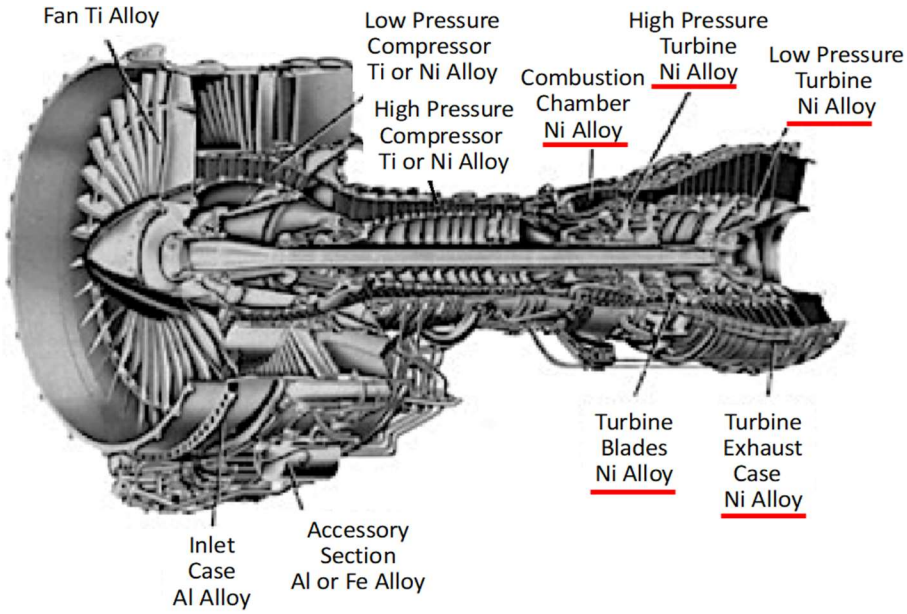

Figure 2.1: A drawing of a gas turbine engine with critical components requiring the use of Ni-base superalloys indicated [6].

Ni-base superalloys are sub-categorized based on their major strengthening mechanisms [5, 10, 11]. Solid-solution strengthened superalloys invoke a variety of substitutional elements as strengtheners [12], and their microstructures generally consist of a single face-centered cubic (FCC) phase (γ) with minor volume fractions of nitrides and/or carbides [10]. Alloy 600, consisting of a Ni-Cr-Fe matrix containing small amounts of titanium nitride and chromium carbide particles, represents one of the prototypical examples of a solid-solution strengthened Ni-base alloy [13].

While these alloys are valuable in certain applications, many industry-critical Ni-superalloys require precipitate-strengthened microstructures. Coherent strengthening precipitates, together with carbides in most superalloy microstructures, offer both direct strengthening contributions and high-temperature creep resistance by inhibiting grain boundary sliding and grain growth during service [12]. The two beneficial precipitates commonly employed are γ'', a body-centered tetragonal (BCT) ordered Ni_3Nb phase, and γ', an ordered cubic phase with the $L1_2$ sublattice and $Ni_3(Al, Ti)$ stoichiometry [10]. Alloy 718 is the most famous example of a γ''-strengthened superalloy [14]. Long considered the 'workhorse' alloy for aircraft engine components, Alloy 718 remains widely used in aerospace today, accounting for 34% of the weight of the average jet engine in 2018 [15]. The power-generation industry more frequently employs γ'-strengthened alloys, whose higher allowable operating temperatures (γ' has a much higher solvus temperature than γ'') offer improved power efficiency [16]. Common contemporary γ'-strengthened alloys include Alloy (Inconel) 738LC, Alloy (Inconel) 939, GTD-222, Mar-M-247, Rene 41, Waspaloy, Haynes 263, and Haynes 282, among others, [17-21]. A subset of these (Rene 41, Waspaloy, Haynes 263, Haynes 282) are wrought alloys that have compositions designed to promote a moderate γ' content of less than 25% to strike a balance between strength and fabricability [17]. Others (Alloy 738LC, 939, MAR-M-247) have compositions that target a γ' content near 50% or greater [18-20], and have limited formability, instead designed to be used as cast products. These alloys are most commonly used for land-based turbine blades and nozzle vanes [22]. Many superalloys for creep-critical applications are designed to be cast as a single crystal [23].

Precipitate-strengthened superalloys are often more compositionally complex than their solid-solution strengthened counterparts. Most precipitate-strengthened superalloys contain significant alloying additions of precipitate formers such as Ti, Al and Nb, as well as Mo, Ta, and other refractory elements to improve performance at high homologous temperatures, while solid-

solution strengthened alloys often have fewer alloying additions [23, 24]. For example, the superalloys directly investigated for braze repair in this work are solid-solution strengthened Alloy 600 and γ'-strengthened Alloy 738LC. Nominal compositions for these two alloys [13, 18] are compared in Table 2.1, demonstrating significantly more compositional complexity in Alloy 738LC.

Table 2.1: Nominal compositions for Alloy 600 and Alloy 738LC [13, 18]

Element	**Alloy 600 Concentration [wt. %]**	**Alloy 738LC Concentration [wt. %]**
Ni	72.0	Balance (61)
Cr	15.5	16.00
Co	-	8.50
Fe	8.0	Low As Possible
Ti	-	3.40
Al	-	3.40
Nb	-	0.90
Mo	-	1.75
Ta	-	1.75
W	-	2.60
Zr	-	0.05
C	0.015 max.	0.11
B	-	0.01
Mn	1.00 max.	Low As Possible
Si	0.50 max.	Low As Possible
S	0.015 max.	Low As Possible
Cu	0.50 max.	-

In the context of **Research Question 1**, it is important to consider the elements that each of these superalloy substrates are expected to introduce to the $Mn_{35}Fe_5Co_{20}Ni_{20}Cu_{20}$ MPEA filler through filler/substrate interactions. Based on the composition information in Table 2.1, the Venn diagrams in Figure 2.2 offer a concise pictorial summary of the major (>1 wt. %) substitutional alloying elements that are common and unique to each material in both filler/substrate pairs. This comparison clearly indicates that Alloy 738LC, while more industrially relevant, presents a far more chemically complex case for brazing. Alloy 600 is only expected to introduce Cr to the MPEA filler, while Alloy 738LC is expected to introduce seven elements, including Cr, Ti, Al, Nb, Mo, Ta, and W.

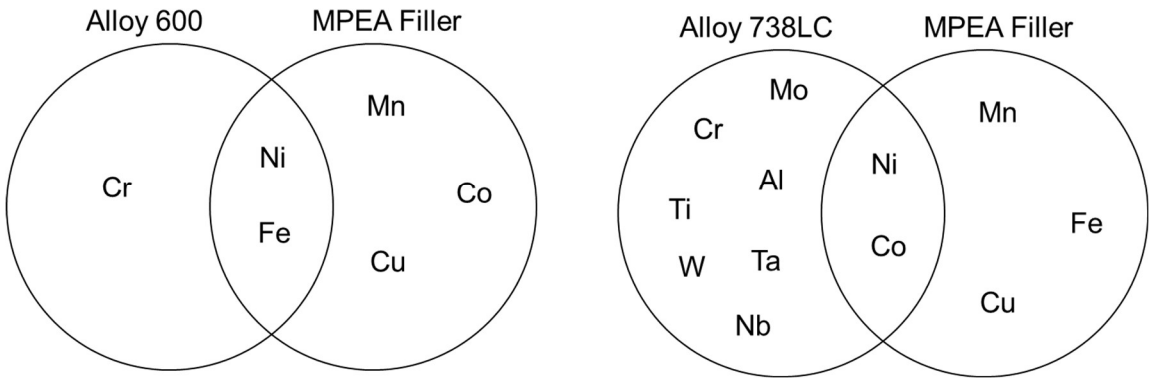

Figure 2.2: Venn diagrams comparing the major (>1 wt. %) substitutional alloying elements in the Alloy- 600/MPEA-filler pair and the Alloy-738LC/MPEA-filler pair, highlighting the additional elements that must be accommodated by the MPEA filler when brazing precipitate-strengthened alloys (*e.g.*, Alloy 738LC)

2.2 Braze Repair of Nickel Superalloys

Despite the exceptional properties of Ni-base superalloys, fatigue, creep, and surface corrosion can nonetheless cause damage and cracking during service [25, 26]. Figure 2.3(a-b) show examples of cracks in gas turbine engine components driven by thermal fatigue during engine operation [27], while Figure 2.3(c) shows an example of a crack arising from the penetration of corrosion product [28]. Reduced operating efficiency from cracked components [25], and the risk of catastrophic engine damage resulting from unexpected failure of a component [29, 30], necessitate regular inspection and repair of damaged components at scheduled maintenance intervals. The length of a maintenance interval is often driven by an appropriate fatigue-life design strategy for the component in question [31, 32].

If cracks are detected during inspection, damaged components can often be returned to service via either weld repairs or braze repairs. Weld repairs entail fusion of the base material in a highly invasive pre-grinding and crack-filling process, while braze repairs entail fusion of only a low-melting-point filler material to accomplish crack-filling via surface wetting and capillary action. Braze repairs thus offer greater flexibility to conform to as-cracked component geometries without extensive pre-grinding required. More importantly, braze repairs avoid a range of hot-cracking and poor weldability issues that frequently plague welding processes for Ni-base superalloys, particularly γ'-strengthened alloys with high Ti and Al concentrations [5, 33-38]. Figure 2.4 shows examples of liquation cracks in the heat-affected zone of Alloy 738 welds; liquation cracking represents one of the most common cracking issues [37, 38]. Thus, γ'-

strengthened alloys are often selected for study of braze repairs to avoid welding the material altogether. Because its high γ' and carbide contents offer microstructural stability at brazing temperatures, and because it is a cast alloy to which grain size strengthening is of relatively little importance, Alloy 738LC in particular is frequently selected [25], so that grain-growth considerations at brazing temperatures may be ignored.

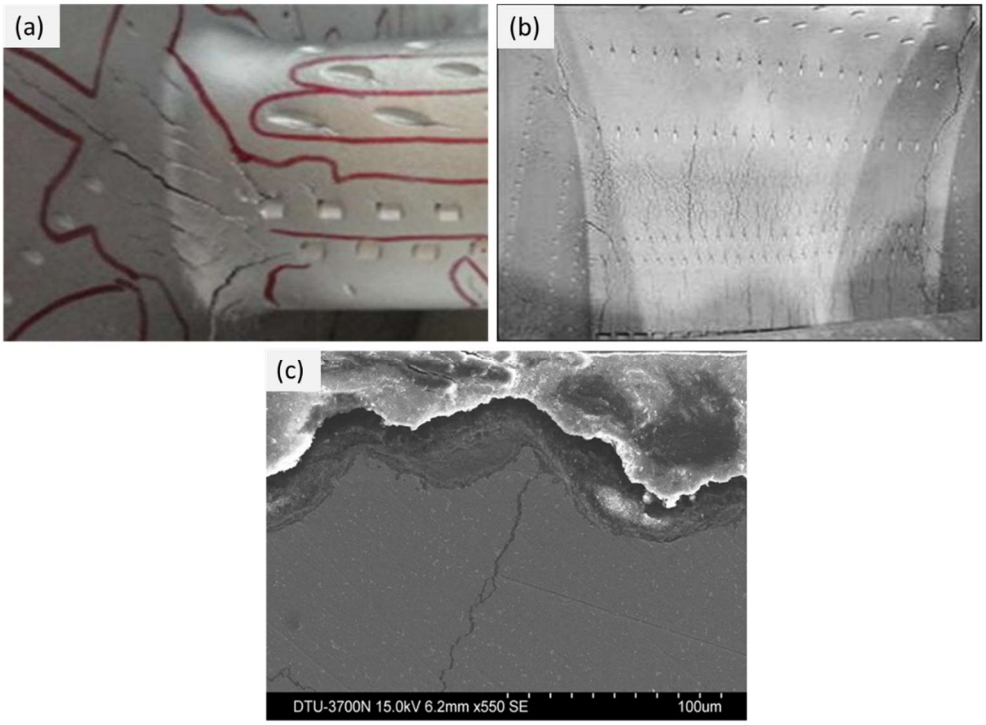

Figure 2.3: Photographs showing examples of cracking in Ni-base superalloy components of gas turbine engines. (a-b) Cracks driven by thermal fatigue during engine operation; photographs provided by Warren Miglietti [27]. (c) Micrograph of a crack resulting from the penetration of corrosion product [28].

In any braze repair, the resultant microstructure follows directly from the solidification mechanism for the filler material in the brazing strategy employed. Subsequent microstructural evolution may proceed if the component is returned to service at a sufficiently high operating temperature to allow kinetically controlled evolution toward equilibrium to occur over observable durations. However, manipulation of the as-solidified microstructure through the selection of filler alloy compositions and brazing process parameters represents the greatest available means for performance control of braze-repaired structures. Understanding the solidification behavior of filler alloy compositions selected to execute repairs is therefore critical.

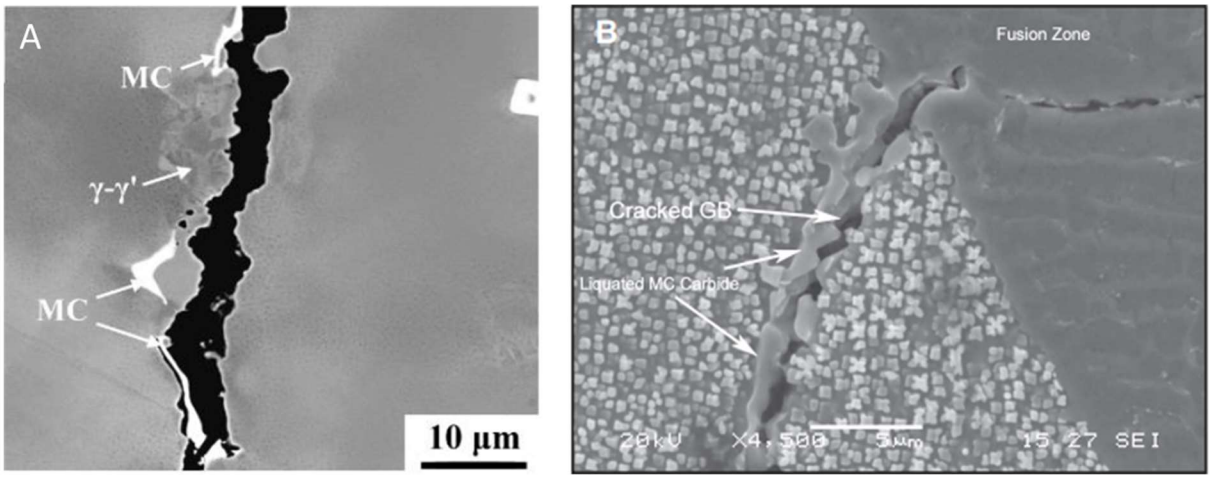

Figure 2.4: Examples of heat-affected zone cracking in welds of γ'-strengthened Alloy 738 [37, 38].

2.3 Review of Existing Filler Alloy Categories and Solidification Mechanisms

The most important attribute driving selection of a filler alloy is its melting point, which must be sufficiently low so that the filler is fully molten at the brazing temperature, which in turn must be carefully selected to be below the solidus temperature of the Ni-base superalloy undergoing repair. The design of filler compositions with sufficiently low melting points is most often accomplished through the deliberate inclusion of melting point depressant (MPD) elements to a composition otherwise similar to that of the parent material. This similarity of composition promotes homogeneity in the final brazed microstructure [25, 39], and the MPD elements serve only the specific purpose of melting-point manipulation. An alternative category of fillers have compositions very disparate from that of the parent material, but with inherently low melting points (ILMPs). These ILMP filler alloys do not possess elements that play the specific role of melting-point depression. Each of these categories of filler materials is reviewed here.

2.3.1 Fillers with Melting-Point Depressant Elements (MPD Fillers)

Traditional MPD elements included in conventional fillers that are otherwise similar in composition to parent nickel superalloy materials are boron and silicon. Figure 2.5 shows the calculated binary equilibrium phase diagrams for Ni with each of these MPD elements, with the concentration ranges found in the commercially available *BNi* series of fillers indicated by shading [40-44]. Each of these phase diagrams possesses a deep eutectic trough that makes B and Si highly effective MPD elements. However, for the full range of typical boron concentrations indicated in

Figure 2.5(a), as well as certain fillers with a high Si content in Figure 2.5(b), direct solidification of the molten filler will result in a substantial phase fraction of Ni_3B or Ni_3Si in eutectic microconstituents. While the orthorhombic and monoclinic Ni_3Si phases are predicted to be replaced by a second solid-solution phase at lower temperatures, this transformation may not be driven to completion during the cooling stage of the brazing thermal cycle, leaving the intermetallic Ni_3Si in the as-brazed microstructure. Furthermore, these phase diagrams do not account for additional boride and silicide phases that may form with other major constituent elements of the superalloy base material, such as Cr. Cr is a strong boride former, and chromium borides are generally at least as prevalent in microstructures reported in the literature as nickel borides (*e.g.*, [45]).

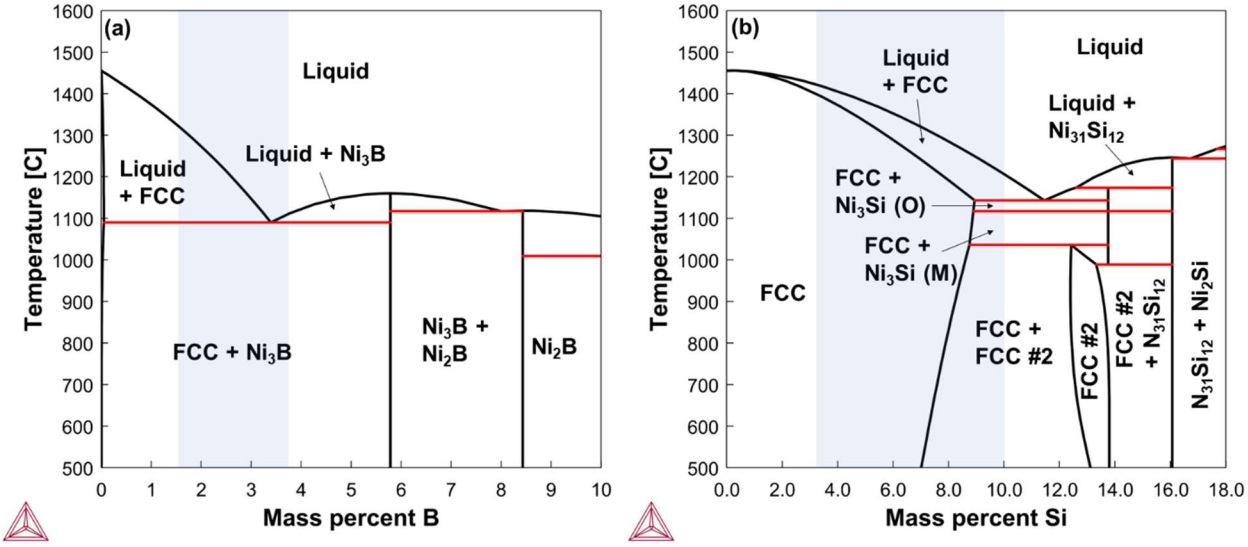

Figure 2.5: Equilibrium phase diagrams for (a) Ni-B and (b) Ni-Si binary pairs, calculated using the ThermoCalc software, with the typical concentration ranges for MPD elements indicated by the shaded rectangles [40-44]. (M) stands for the monoclinic crystal structure, and (O) stands for the orthorhombic crystal structure.

2.3.1.1 Unmitigated (Direct) Eutectic Solidification

Boride and silicide phases are very brittle, and therefore sufficiently detrimental to the mechanical performance of brazed structures that some mitigation strategy is usually employed to reduce or eliminate these second phases. There are few studies reporting on the properties of B- and Si-suppressed brazes allowed to solidify eutectically with no mitigation. One exception is a study by Tung et al., in which the authors studied microstructure manipulation of Alloy 270 joints

brazed with BNi-4 filler by controlling only the cooling rate and holding temperature [46]. While the authors achieved substantial morphological control by adjusting these parameters, resultant microstructures universally contained brittle nickel-boride and nickel-silicide constituents [46].

A set of studies by Miglietti and DuToit attempted to mitigate brittleness induced by borides and silicides by replacing B and Si with the unconventional MPD elements of Hf and Zr in fillers for brazing Alloy 738 [47, 48]. As these elements are much slower diffusers than B and Si, little isothermal solidification could be achieved, so this qualifies as a direct eutectic solidification mechanism rather than a transient liquid phase process (see Section 2.3.1.2). The resultant eutectic microconstituents contained Ni_7Hf_2, Ni_5Hf, or Ni_5Zr intermetallic phases [47, 48]. It is noteworthy that these phases were found to be 2 – 3 times softer than typical borides and silicides, and therefore less detrimental to ductility [47, 48]. However, total elongation of joints in tension never exceeded 5%.

2.3.1.2 Transient Liquid Phase Mechanisms (Isothermal Solidification)

Transient liquid phase (TLP) processes date back to the 1970s [25, 49] and have since become one of the most common industrial practices to reduce or eliminate eutectic microconstituents in B- and Si-suppressed braze repairs. Numerous studies describe either TLP bonding or TLP infiltration for repair of Ni-base superalloys. TLP bonding was comprehensively reviewed by Gale and Butts in 2004 [39], with the mathematics governing the process previously discussed by Liu et al. in 1991 [50]. TLP infiltration was comprehensively reviewed by Huang and Miglietti in 2012 [25].

Figure 2.6 illustrates the stages of a typical TLP process in practice [25, 39, 50]. Figure 2.6(a) provides a simplified schematic eutectic phase diagram with key compositions marked for reference, and the schematics in Figure 2.6(b) highlight the microstructural evolution. In the process, a molten filler rich in MPD elements (composition C_0) is delivered to the joint gap and brought to a bonding temperature T_B, fully melting as shown in Figure 2.6(b-i). This step is followed by rapid dissolution of the adjoining substrate until the MPD element concentration in the liquid is diluted to the liquidus C_L in Figure 2.6(b-ii). Subsequently, the assembly is held at T_B while rapid diffusion of the MPD element into the base material, a diffusion sink, causes a local composition change that drives isothermal solidification. This stage is depicted in progress in Figure 2.6(b-iii). B and Si are ideally suited to the role of MPD elements in this situation because

they are rapid diffusers in Ni. In theory, the liquid composition remains at C_L, while full equilibrium is established at the solid-liquid interface, causing the immediately adjacent solid composition to lie at the solidus C_S, and the MPD element concentration to diminish with distance from the liquid. In practice, departures from this ideal equilibrium lead to precipitation of undesired phases, described below.

Note that Figure 2.6 highlights TLP bonding, but TLP infiltration differs only in the geometry of the diffusion sink(s). Rather than delivering only filler material to a gap, TLP infiltration incorporates base material powder particles to serve as additional diffusion sinks for MPD elements, enabling isothermal solidification to occur in joint clearances that span wider distances [25]. For this reason, TLP infiltration is often referred to as wide-gap brazing. This means of filler delivery is known as blended powder delivery and requires optimizing the ratio of filler to base material particles as an additional parameter [51].

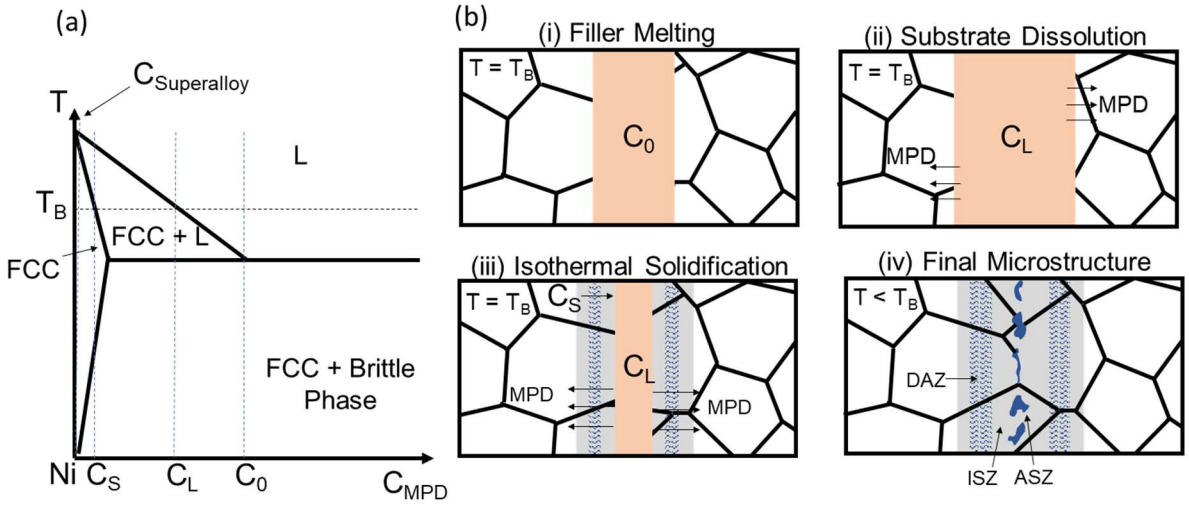

Figure 2.6: (a) Schematic Ni-MPD element phase diagram and (b) stages of a TLP bonding process with common deviations from ideality indicated in the final microstructure (modelled after [39, 50]).

In ideal TLP processes, isothermal solidification is driven to completion [25, 39]. No residual liquid remains in the brazing seam, and eutectic microconstituents are successfully avoided. This situation is not depicted in Figure 2.6(b-iv) because it is difficult to achieve in practice. If the hold duration at T_B is insufficient, the isothermally solidified zone (ISZ) may not encompass the entire brazed structure. Residual liquid may remain in the brazing seam as cooling

begins, which will create an athermally solidified zone (ASZ) with eutectic microconstituents at the immediate centerline (*e.g.,* [52, 53]).

Even if an ASZ is avoided, an additional phenomenon that has been observed in the majority of studies on TLP processes (*e.g.,* [45, 52-59]) is the formation of a diffusion affected zone (DAZ) where boride (and sometimes silicide) phase precipitation occurs during or after the isothermal hold, caused by local supersaturation of the MPD elements. Ojo et al., among others, note that these DAZ precipitates (usually borides) result from boron diffusion into the base material outpacing the establishment of equilibrium between the solid and liquid phases [59]. Gale and Wallach offer the most detailed discussion of this phenomenon, including a mathematical example demonstrating that, in the absence of constraints posed by solid-liquid equilibrium at the interface (*i.e.,* defined boundary conditions at the interface), boron will diffuse through the entire structure as a continuum instead [54]. The distinction between a situation in which solid/liquid equilibrium is fully established prior to appreciable boron diffusion (ideal TLP) and a situation in which boron diffusion outpaces equilibrium (practical TLP) is further illustrated by the schematic composition profiles in Figure 2.7.

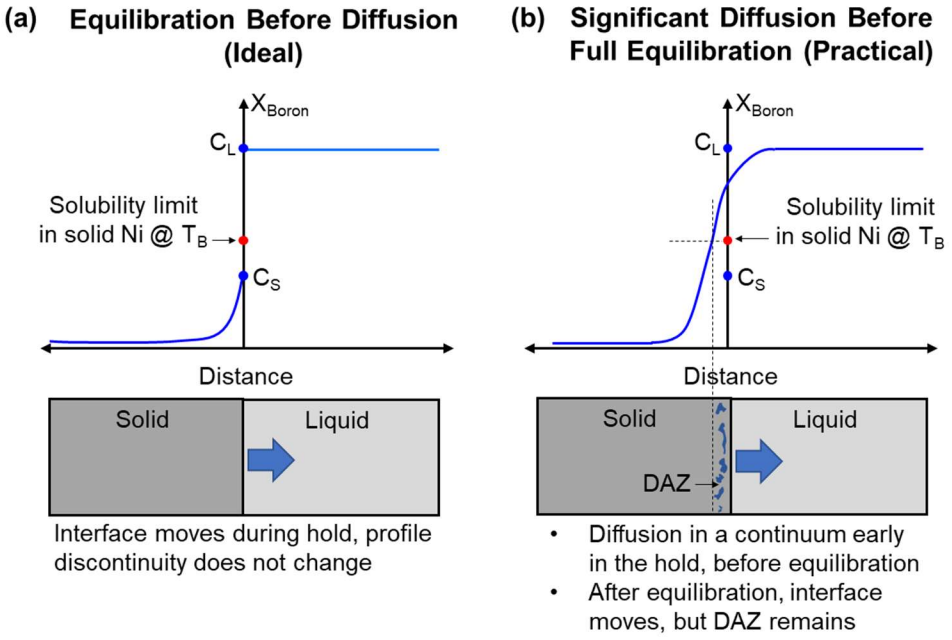

Figure 2.7: Schematic boron concentration profiles near the solid-liquid interface in (a) an ideal TLP process where equilibration completes before diffusion begins, and (b) a practical TLP process where equilibration and diffusion occur simultaneously, leading to boron supersaturation. Based on discussion in [54].

In the ideal case in Figure 2.7(a), the constraints imposed by solid-liquid equilibrium keep the boron concentration below the solubility limit throughout the solid material. In the practical case in Figure 2.7(b), the boron concentration profile can be estimated by Equation 2.1 for diffusion out of a finite interlayer into a semi-infinite solid substrate [54]:

$$C(x,t) = \frac{1}{2} C_L \left(\text{erf} \frac{h-x}{2\sqrt{Dt}} + \text{erf} \frac{h+x}{2\sqrt{Dt}} \right) \quad (2.1)$$

Where C represents the variable concentration, C_L is the liquidus concentration, x is the distance from the center of the finite interlayer, h is the interlayer half-width, D is the solute (boron) diffusivity, and t is the diffusion time. As indicated in Figure 2.7(b), the width of the DAZ will be determined by the distance into the solid substrate at which the variable concentration exceeds the boron solubility in the solid. Gale and Wallach use reported diffusivity values, an assumed interlayer width of 50 μm, and an estimated time of 1 minute for solid-liquid equilibration to occur to calculate that the boron concentration 10 μm into the solid substrate will be nearly 10 times in excess of the solubility limit under these conditions. This simplified calculation illustrates that the DAZ is likely to routinely exceed 10 μm in width in practical TLP processes. Furthermore, Pouranvari et al. discuss that once precipitated, it is exceedingly difficult for these detrimental phases to re-dissolve completely, though post-braze heat treatments may offer some degree of improvement [45].

Overall, literature in which TLP processes for Ni-base superalloy repair consistently avoid both an ASZ and a DAZ is scarce. The prevalence of a DAZ in particular is highlighted in Figure 2.8, which is an agglomeration of SEM micrographs from five independent studies of TLP bonding on either Ni-Alloy 738 or 718 [45, 55-58]. The extent of isothermal solidification achieved among the studies varies, but all the micrographs present a distinct DAZ, characterized by a high density of boride precipitates with a needle-like morphology. The ubiquity of brittle phases is also reflected in the ductility data assembled by Huang and Miglietti for TLP infiltration repairs, which usually does not exceed 3% [25]. Importantly, the introduction of boride and/or silicide phase during repair leaves superalloy microstructures susceptible to re-cracking during subsequent service, especially via creep or low cycle fatigue [47, 48, 60].

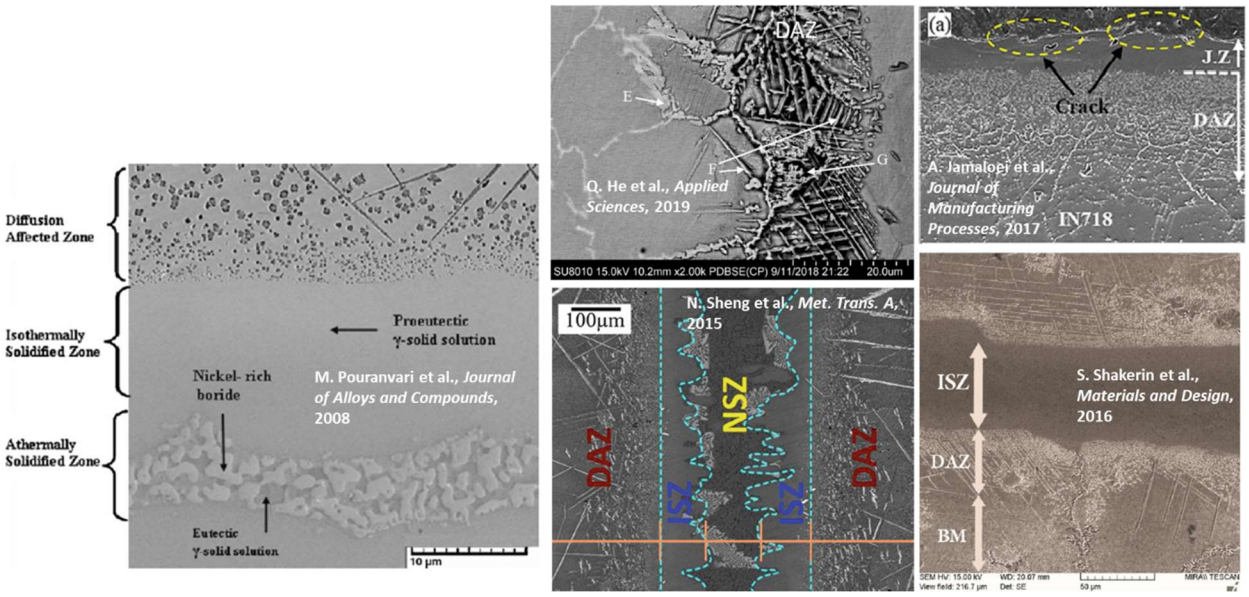

Figure 2.8: Agglomeration of SEM micrographs from five independent studies which brazed either Alloy 738 or Alloy 718 using a TLP process, highlighting the ubiquity of a diffusion affected zone (DAZ) [45, 55-58].

Occasionally, a variation on conventional TLP processes is employed in which the assembly is only held at the initial brazing temperature for a short duration, and then a long diffusion treatment at a temperature 50 – 100°C below the brazing temperature immediately follows [22, 61, 62]. This variation is sometimes referred to as activated diffusion brazing [22, 62]. Su et al. employed this process using DF-4B, an industry-leading filler with relatively low boron content, but these authors did not avoid the precipitation of chromium borides in their microstructures [22, 62]. The alternative use of Nicrobraz 150, a filler with higher boron content, saw the additional formation of nickel borides.

2.3.1.3 Multi Principal Element Alloy Fillers with MPD Elements

Since their advent in the early 2000s [63, 64], high entropy alloys (HEAs) and the broader class of multi-principal elements alloys (MPEAs) have garnered attention in the metallurgical community for use in structural or refractory applications. Within approximately the last five years, several research groups worldwide have turned attention toward employing these as filler materials, with a handful of key studies emerging pertaining to Ni-base superalloy joining or repair [2, 65-68]. A subset of these studies have employed a strategy of adding MPD elements to a well-known equiatomic HEA [66, 67]. These studies invoked the 'entropy effect', one of four original postulates of HEAs (see Section 2.4 for more details) [64, 69], to hypothesize that high

configurational entropy in these near-equiatomic filler candidates may promote accommodation of MPD elements in a ductile, disordered solid solution phase.

This approach has thus far proven not entirely successful at eliminating non-solid-solution phases from brazed microstructures. Hardwick et al. brazed Alloy 718 with a filler using Ge additions to suppress the melting point of a NiCrFe MPEA [66]. Further additions of 2.5 at. % boron were nonetheless required to make the filler suitable for brazing at 1100°C. Although this boron content is reduced relative to conventional TLP fillers, the inclusion of any quantity of boron rendered a TLP mechanism necessary to avoid eutectic borides. While isothermal solidification was reportedly achieved after a hold time of 60 min, a significant network of borides were present in the microstructure of brazed joints, along with an additional Ni-Ge-Nb rich phase, as shown in Figure 2.9 [66].

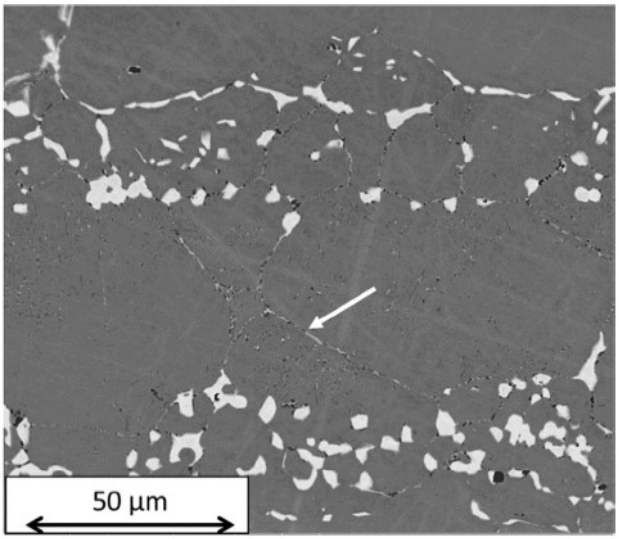

Figure 2.9: Microstructure of Alloy 718 joint brazed with the NiCrFeGeB MPEA with boron additions explored by Hardwick et al. Grain boundary borides are indicated by the white arrow, and a secondary Ni-Ge-Nb rich phase appears white in the micrograph [66].

A separate study by Tillmann et al. explored additions of Ga, Ge, and Sn to equiatomic CoCrCuFeNi as potential filler materials [67]. CoCrCuFeNiGa was selected as the most promising candidate to braze Alloy Mar-M-247, albeit at a high brazing temperature of 1270°C. While this study successfully eliminated boron as an MPD element, the resultant microstructure remained complex, with three solid-solution phases and three intermetallic phases identified as shown in Figure 2.10 [67]. The specific solidification mechanism resulting in this microstructure is not examined, but two of the three intermetallic phases contain Ga, suggesting that its inclusion in the

filler may contribute to the formation of undesired phases in the solidification sequence. Furthermore, the reputation of Ga as an element causing liquid metal embrittlement in aluminum and other alloys [70] makes its inclusion in any potential repair filler alloy wholly undesirable.

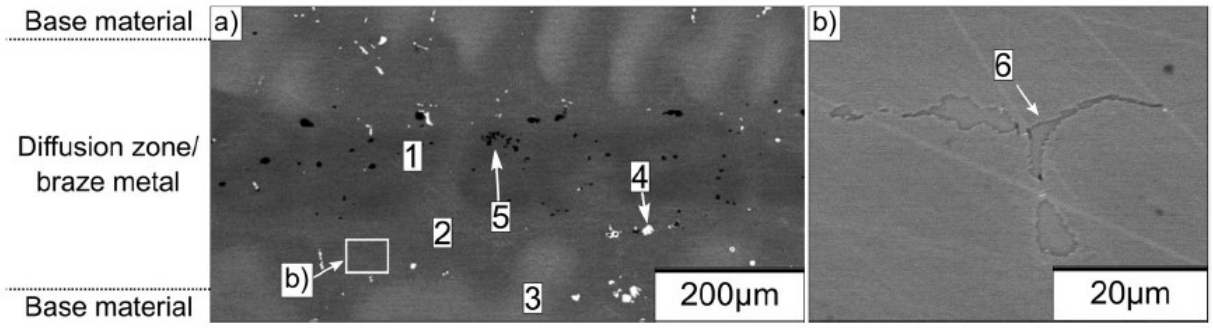

Figure 2.10: (a) Low magnification and (b) higher magnification electron micrographs of Mar-M-247 superalloy brazed with CoCrCuFeNiGa MPEA, with Ga serving as an MPD element. Phases 1-3 are identified as solid solutions, and Phases 4-6 are identified as intermetallics. Phase 6 is a Ni-Ti-Ga-Al rich intermetallic [67].

2.3.2 Fillers with Inherently Low Melting Points (ILMP Fillers)

Inherently low melting point (ILMP) fillers are generally very disparate in composition from parent superalloy materials, but they are designed to avoid requiring the inclusion of specific elements whose only role is to depress the melting point. The composition of these fillers is typically selected such that solidification to a single, ductile FCC phase is possible. The ILMP fillers need not have a melting point that is low in an absolute sense, but rather only relative to the brazing temperature in the desired application. The ILMP fillers can be further subcategorized into noble-metal fillers and MPEA fillers without MPD elements.

2.3.2.1 Noble Metal Fillers

Gold and silver have traditionally been considered excellent basis elements for ILMP fillers due to their low melting points (1064°C for Au and 962°C for Ag) and unreactive nature. Both display positive deviations from ideality in their enthalpy of mixing with Ni [71], indicating that phase separation will be preferred over the formation of intermetallic compounds. The binary phase diagram for Ni-Au in Figure 2.11(a) [72] indicates that solidification to a single FCC phase is possible over the entire composition range, with a miscibility gap forming in the solid state at lower temperatures. The Ni-Ag phase diagram in Figure 2.11(b) [73] displays a miscibility gap in the liquid state. This creates difficulty with wetting a Ni-base superalloy substrate; for this reason,

Ag-based fillers are typically heavily alloyed and include minor additions of Ti to promote wetting [74]. This class of Ag-based fillers are known as active braze alloys (ABAs). ABAs may be used for superalloy repair, but they are more commonly employed to accomplish dissimilar joining and metal-to-ceramic brazing [74].

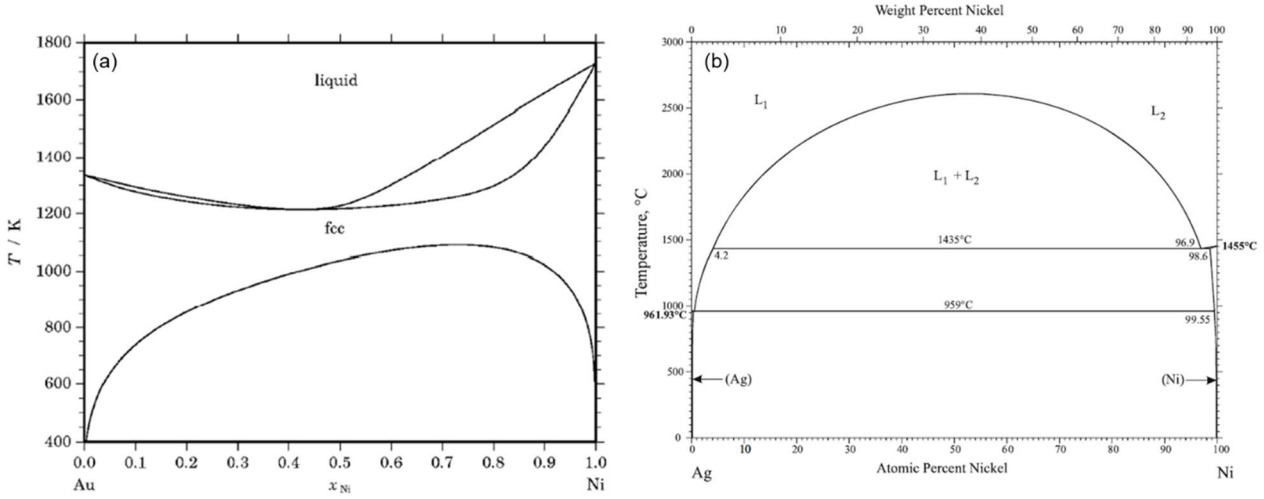

Figure 2.11: Binary phase diagrams for (a) Ni-Au [72] and (b) Ni-Ag [73].

Au-based brazes were among the leading technologies for brazing Ni-base superalloys until the 1970s, prior to the widespread adoption of TLP processes with much less expensive filler materials (Section 2.3.1.2). In 1975, Schwartz compiled mechanical property data for Alloy 718 joints brazed with a variety of Au-based fillers, with an average tensile strength of 815 MPa and average ductility of 12% reported for 82Au-18Ni filler [75]. This finding indicates that Au-based fillers can create high-strength joints without brittle phases, but the extreme cost of Au and the high volume of industrial Ni-base superalloy repairs has driven research into other fillers in the past fifty years.

Most of this research has been dedicated to the TLP processes described previously, but a few studies in noble metal fillers have examined the less-expensive Ag-based option for Ni-superalloy repair. Generally, these studies have demonstrated less success in achieving ductile, single-phase microstructures than for Au-based fillers. Zaharinie et al. used Ag-based Cusil ABA to braze Alloy 600, but reported multiple phases in the microstructure, including a Ni-Ti reaction layer [76]. Khorram et al. used an alternative titanium-free filler of composition 57Ag-22Cu-16.5Zn-4.5Sn to laser-braze Alloy 718, but found significant fractions of eutectic microconstituent

in joints [77]. In both studies, reported strengths were less than half of what was reported for the Au-based fillers.

2.3.2.2 Multi-Principal Element Alloy Fillers without MPD Elements

A relatively inexpensive alternative to noble metal ILMP fillers lies in MPEAs, whose constituent elements are usually commonplace. As discussed in Section 2.3.1.3, a subset of studies on MPEA fillers focuses on near-equiatomic compositions with MPD element additions, relying on entropy effects to target single-phase microstructures. However, the postulate of a universal 'entropy effect' that stabilizes solid-solution phase formation across a broad range of constituent elements has been largely debunked [1, 78], which will be discussed further in Section 2.4. Nevertheless, certain MPEA systems based in 3-d transition metals may favor single-phase FCC microstructures across a broad composition space within the system [1].

This combination of ideas led to certain studies exploring MPEAs at non-equiatomic compositions to create ILMP fillers which do not require extrinsic MPD element additions to be suitable for brazing, and therefore are capable of solidifying to a single, ductile FCC phase. Such exploration requires a careful, rigorous down-selection process to identify ILMP-MPEA fillers whose melting points are in the appropriate range [3]. The candidate filler of this description that has been researched most extensively is $Mn_{35}Fe_5Co_{20}Fe_{20}Cu_{20}$ (composition approximate) [2, 3, 68, 79, 80], discussed further in the following sections.

2.4 Contextual Review of High Entropy Alloy Postulates

Like much research in the field of HEAs or MPEAs, the conceptualization of $Mn_{35}Fe_5Co_{20}Ni_{20}Cu_{20}$ as a filler material originally began as an attempt to harness the benefits of the four 'core effects' posited by the field's independent pioneers, Jien-Wei Yeh and Brian Cantor [63, 64]. These include the 'entropy effect', sluggish diffusion, severe lattice distortion, and the 'cocktail effect' [64, 69, 81-83]. A brief description of each of these effects follows:

- Entropy effect: The configurational entropy term in the Gibbs free energy equation will become increasingly dominant when increasing the number of constituent elements, allowing disordered solid solutions to outcompete intermetallic compounds in energetic favorability [64, 69, 82].

- Sluggish diffusion: Fluctuation in lattice potential energy among individual atomic sites will be high in a disordered solid solution with many constituent elements. Certain atoms will become kinetically 'trapped' at low-potential sites, slowing the overall diffusion kinetics in the system [84].
- Severe lattice distortion: Loss of crystalline perfection will stem from incorporating many elements of disparate atomic radii on the same crystal lattice, contributing to exceptional solid solution strengthening behavior [81].
- Cocktail effect: Mixing many elements in a concentrated alloy system may result in (potentially beneficial) properties that deviate from those predicted by a simple rule of mixtures [69].

Yeh in particular theorized that these core effects, each proposed to stem directly from the configurational entropy of a composition, would be universally applicable to any alloy with constituent elements in near-equiatomic concentrations, regardless of element identity [69, 82]. This proposed universality is because configurational entropy ΔS_{config}, given by Equation 2.2, depends only on element concentration and not element identity [83]. In the equation, *R* represents the gas constant, *C* is concentration of constituent element *i*, and *n* is the total number of elements.

$$\Delta S_{config} = -R \sum_{i=1}^{n} C_i \ln C_i \tag{2.2}$$

However, as research on HEAs/MPEAs has continued to grow, skepticism toward or outright rejection of Yeh's universal postulates has also grown. Miracle and Senkov, and Pickering and Jones, each coauthor independent comprehensive reviews that argue that these postulates are not cross-cutting [1, 85]. Key individual studies on the 'entropy effect' include work by Otto et al. which explicitly demonstrated a lack of single-phase stability as constituent elements were interchanged in quinary alloys [78]. This work demonstrated that enthalpy terms, which are functions of element identity, must be critically evaluated alongside configurational entropy when assessing predicted phases. Pertaining to sluggish diffusion, Jin et al. measured the diffusion kinetics of Ni in several alloy systems ranging from binary to quinary, and concluded that any sluggish diffusion effect that exists is strongly dependent on the specific constituents, as a NiCoFeCrPd alloy was found to have more rapid diffusion kinetics than several quaternary and even ternary subsystems that excluded Pd [86]. Owen et al. analyzed the extent of the lattice distortion in CrMnFeCoNi by constructing pair distribution functions from neutron diffraction

data, and concluded that the lattice distortion is not anomalously larger than that in simpler alloy subsystems [87]. The 'cocktail effect' has not been contradicted, but Miracle and Senkov argue that it is more of a generic statement of the unpredictable nature of materials research than a true scientific hypothesis [1].

As each set of reviewers implicitly argue, the demise of the suggested universality of these principles carries positive implications for materials design [1, 85]. The underlying tone of their conclusions is one of gratitude to the pioneers of HEAs/MPEAs for sparking thought about a vast and previously untapped alloy design space, and optimism that materials of significant value that are not beholden to strict definitions of configurational entropy await discovery there.

As discussed in [3], the first three of the 'core effects' were originally hypothesized to hold benefits to an alloy serving as a Ni-base superalloy repair filler. The entropy effect would serve to stabilize ductile disordered solid solutions over brittle intermetallic compounds, sluggish diffusion would serve to slow potentially detrimental interactions with base materials, and severe lattice distortion would offer excellent solid solution strengthening contributions. However, considering the growing skepticism surrounding these effects, the research questions governing this thesis shift focus away from the role of entropy. Moreover, the concluding chapters of this thesis will discuss that the benefits of using MPEAs as braze fillers for Ni-base superalloys are less interwoven with the 'core effects' than originally conceptualized.

Miracle and Senkov argue that despite the absence of a cross-cutting entropy effect, certain regions of composition space are nonetheless favorable to the formation of a single solid-solution phase [1]. They point to the plethora of studies on different 3d-transition metal MPEA compositions, which usually report the dominance of solid-solution crystal structures, arguing that these studies all indicate manifestations of the same phase that is interconnected in hyper-dimensional phase space [1]. In keeping with the idea that it is critical to consider enthalpy alongside entropy, they point out that this family of materials is exceptional in that it contains many binary element pairs with near-zero mixing enthalpies [1]. Thus, this composition subspace, while significantly reduced from the overarching class of MPEAs, still represents a broad area in which materials with robust single-phase crystal structures may be discovered.

Along this line of thinking, the governing hypothesis of this thesis deals with *select* MPEA composition spaces, such as that proximal to $Mn_{35}Fe_5Co_{20}Ni_{20}Cu_{20}$. Significant computational work [3] has identified this window as one of the MPEA composition subspaces most tolerant to

perturbations while keeping detrimental intermetallic phases suppressed. Perturbations may take the form of compositional variation within the MnFeCoNiCu system, introduction of additional elements from Ni-base superalloy materials, and/or exposure to a range of operating temperatures during component service. Experimental assessments of phase equilibria within the MnFeCoNiCu system generally agree that an FCC solid solution is the dominant phase, although nanoscale Cu-clustering and a (Fe, Co)-rich B2 precipitate phase have been reported [88-90]. Overall, the discussion of TLP processes in Section 2.3.1.2 illustrates that when using the most popular current alternative technology for brazing Ni-base superalloys, the introduction of some amount of non-native boride or silicide phases is very common. The governing hypothesis proposes that the tolerance of the selected MPEA subspace to perturbation is sufficient for this MPEA filler to be more effective than TLP processes at preventing the introduction of non-native phases.

2.5 Prior Study of $Mn_{35}Fe_5Co_{20}Ni_{20}Cu_{20}$ as Filler Material

The $Mn_{35}Fe_5Co_{20}Ni_{20}Cu_{20}$ MPEA was previously shown by synchrotron X-ray diffraction (XRD) to solidify to a single FCC solid solution with segregation *as a stand-alone material* [3, 80]. However, the original paper reporting use of this MPEA in brazing Alloy 600 did not rigorously characterize the phases present in the resultant braze microstructure [2]. Energy dispersive spectroscopy (EDS) identified local elemental segregation in the braze, but no high-magnification imaging or site-specific diffraction analyses were performed. Instead, the presence of a ductile solid solution phase in the braze was inferred, based on the known FCC crystal structure of the initial as-cast filler and the extent of plastic deformation observed during shear testing of brazed lap-joints [2]. Additionally, while the role of Cr introduction to the MPEA is considered, this original work does not fully acknowledge the extent of the composition change in the filler zone induced by the brazing process, or its implications for single-phase stability.

Alongside the primary research questions posed in Chapter 1, these knowledge gaps are filled in the subsequent chapters of this thesis. Chapter 4 includes a thorough, site-specific synchrotron XRD characterization of the Alloy 600 braze in its as-brazed condition, confirming the presence of an FCC solid solution as the primary microconstituent, and identifying minor inclusions previously disregarded. Though Chapter 5 focuses on interactions between the $Mn_{35}Fe_5Co_{20}Ni_{20}Cu_{20}$ MPEA and Alloy 738LC, the phase identification methodology detailed therein was also crucial in rigorously identifying all the microconstituents of the Alloy 600 brazes.

Finally, Chapter 6 focuses specifically on the extent of MPEA-filler composition change when brazing both Alloy 600 and Alloy 738LC, offering a new, direct illustration of the importance of considering resultant compositions in MPEA filler design.

CHAPTER 3:
DUCTILE BRAZE REPAIRS FOR NI-BASE SUPERALLOYS USING NOVEL MPEA FILLER

Based on a paper published in *Welding Journal*,*
a publication of the American Welding Society

Benjamin Schneiderman[1], Olivia DeNonno[1], Jonah Klemm-Toole[1], Zhenzhen Yu[1]

3.1 Abstract

The performance of a newly developed multi-principal-element alloy (MPEA) filler for brazing of Ni-base superalloys was directly compared to a conventional boron- and silicon-suppressed filler (BSSF). The comparison was demonstrated on an Alloy 600 substrate with a brazing temperature of 1200°C. Single-phase solidification behavior and the absence of boron and silicon in the MPEA led to a joint microstructure devoid of eutectic constituents or brittle phases in brazes employing this filler. In the brazes using the conventional BSSF, incomplete isothermal solidification and subsequent athermal solidification of the residual liquid resulted in large particles of a Cr-rich boride phase distributed throughout the microstructure. Tensile testing of brazed butt joints at both room temperature and 600°C testing conditions demonstrated that the MPEA joints exhibited total ductility values at least one order of magnitude greater than that of BSSF joints fabricated under the same brazing conditions, but comparable yield strengths at both testing conditions. Fractographic assessment confirmed that boride phases nucleated cracks and resulted in brittle failure in the BSSF joints, while the MPEA joints exhibited extensive ductile micro-void coalescence. Fine-scale porosity and oxide inclusions may be the dominant factors limiting the overall ductility observed in the MPEA brazes.

---

[1] Colorado School of Mines, Golden, CO, 80401

3.2 Introduction

Nickel-base superalloys are widely employed in elevated-temperature applications in the power-generation and aerospace industries due to their desirable mechanical properties at high temperatures. Despite their exceptional properties, damage mechanisms such as fatigue, creep, and surface degradation cause cracking in Ni-base components during service [25]. Braze repair processes have been developed over the past several decades in attempts to prolong component service life. Conventional brazing, in which a molten filler material is briefly flowed into the damage-induced gap or crack, typically employs Ni-base filler materials with boron and/or silicon added as melting-point depressants (MPDs). Solidification upon cooling leaves behind significant volume fractions of boride or silicide phases within eutectic constituents, which are brittle and degrade joint ductility [25, 46].

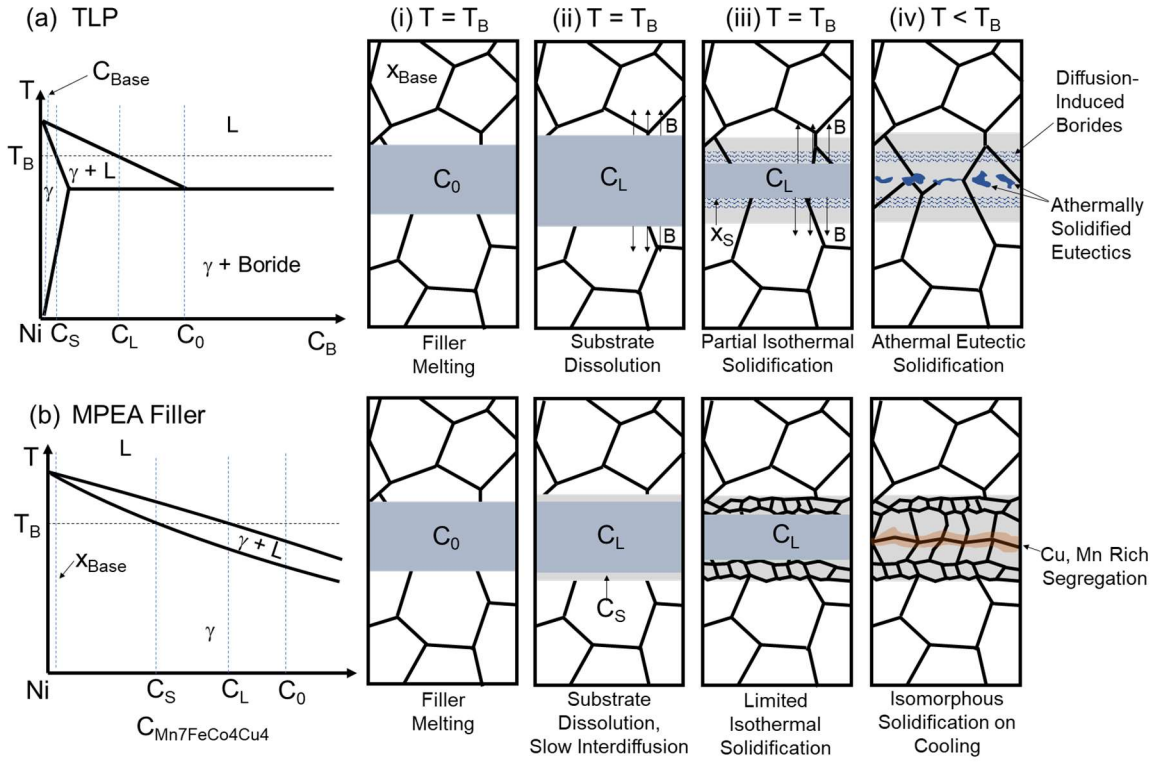

Figure 3.1: Schematic illustrations of the phase diagram and microstructure evolution during brazing using: (a) conventional TLP braze filler with formation of secondary phases in eutectic constituents, modeled after [39]; and (b) the new MPEA filler.

Transient liquid phase (TLP) brazing, either using a molten braze filler only [39, 45, 54-56, 91], or a mixture of filler and substrate powder (also called wide-gap brazing or transient liquid

phase infiltration (TLI)) [25, 92-95], can theoretically eliminate borides and silicides from the microstructure. These processes rely on the rapid diffusion of MPD elements into the substrate material, as shown from stages (i) to (ii) in Figure 3.1(a), causing a local composition change that drives isothermal solidification at a holding temperature. In the case of TLI, substrate powder particles serve as additional diffusion sinks to enable isothermal solidification to occur with wider joint clearances, by shortening necessary diffusion distances [25, 92-95]. Ideally, TLP and TLI are expected to result in a homogeneous microstructure with no second phases and high-strength brazes with appreciable ductility [25, 92]. However, homogeneous microstructures are rarely achieved in industrial braze repairs. Full isothermal solidification requires long hold times for MPD diffusion to reduce the solute content to the solidus composition ($\leq C_s$ in the phase diagram of Figure 3.1(a)), often on the order of hours for a narrow joint gap of approximately 25 μm [25, 45]. Incomplete isothermal solidification may occur if the hold time is insufficient, leaving behind residual liquid that subsequently solidifies athermally as a eutectic mixture during cooling [25, 55, 56, 91], as illustrated by stages (iii) and (iv) of Figure 3.1(a). Furthermore, if the brazing temperature is below the binary eutectic temperature of a pair of elements in the system, diffusion-induced saturation of B or Si beyond the solubility limit [39, 54-56, 91] may occur, causing precipitation of borides or silicides in the solid state, as illustrated in stages (iii) and (iv) of Figure 3.1(a). These second phases usually do not redissolve without an additional elevated temperature heat treatment [39, 45]. The role of diffusion-induced boride and silicide phases in the brazed microstructure is important to consider. Literature reports do not isolate the impact of the diffusion-induced boride or silicide precipitates upon mechanical properties, usually instead discussing athermally solidified borides and silicides as the primary ductility inhibitors. However, it is noteworthy that poor ductility is often demonstrated even at long process durations. For example, a comprehensive review of mechanical properties in wide-gap Ni-base superalloy brazes performed by TLI indicated that the highest room-temperature elongation achieved was 2.3%, in a process employing a hold duration of up to 20 hours [25].

Boron-free and silicon-free braze fillers can be employed using conventional brazing cycles of shorter duration, but these are usually based in expensive noble metals such as Au or Ag [75, 77]. Miglietti and Du Toit reported studies on Ni-base fillers for conventional brazing in which the MPD elements were replaced by either Hf or Zr [47, 48]. Most of the resulting microstructures contained eutectic constituents with phases rich in these new MPDs [47, 48]. Although these

eutectics were not as detrimental to ductility as borides or silicides, and the joints exhibited strength approximately 65% of that of the base material over a range of testing temperatures, the total tensile elongation did not exceed 5% [47, 48]. Hence, there is a need for superalloy braze repair fillers that offer a combination of high ductility and strength, short processing durations, and inexpensive constituent elements.

3.3 Filler Design Strategy

The authors' research group recently developed a new multi-principal-element alloy (MPEA) filler of approximate composition $Mn_{35}Fe_5Co_{20}Ni_{20}Cu_{20}$ [2, 80] to address this challenge. Early theory pertaining to MPEAs predicted several properties that render them attractive candidates for a novel class of filler alloys, including vast design space, single-phase stability [63, 64, 69], severe lattice distortion [81] within a random solid solution structure, and the potential for sluggish diffusion [84, 86]. Lattice distortion may lend itself to extensive solid solution strengthening and corresponding toughness. Sluggish diffusion may delay undesirable interactions with superalloy substrates during service at elevated temperatures, inhibiting detrimental secondary phases by limiting interdiffusion across the joint interface. Nonetheless, a flexible design space to tune the solidification range and a stable single phase with appreciable ductility are the most important characteristics of MPEAs, giving them the potential to avoid formation of brittle second phases that plague superalloy repair with conventional fillers. This scenario is illustrated in Figure 3.1(b), where very limited isothermal solidification occurs during the braze holding step, and no second phases precipitate during subsequent solidification of the remaining liquid during cooling.

While more recent studies have questioned the universality of entropy-stabilized single-phase behavior among MPEAs [78], there is a general acknowledgment that ductile face-centered cubic (FCC) crystal structures are prevalent among 3d-transition metal MPEAs [1]. Exploiting this, the specific filler composition was down-selected from a set of nine 3d transition metal elements via a multi-step computational approach to filter a large candidate pool. The design criteria governing candidate down-selection were to generate a single-phase FCC microstructure and a sufficiently low liquidus temperature to braze at least 100°C below the solidus temperature of the Alloy 600 substrate [2]. The down-selection process was subdivided into three phases as described below.

Phase I targeted the selection of an appropriate alloy system, or a group of five elements with a high likelihood of exhibiting a single-phase FCC crystal structure over a wide composition space. In MPEA literature, the traditional Hume-Rothery rules [96-98] were extended [1, 99, 100] to define appropriate ranges for atomic size mismatch, average valence electron concentration, ΔS_{mix} (entropy of mixing), and ΔH_{mix} (enthalpy of mixing) that would favor the stability of disordered solid solution FCC phases. Of the five-element systems considered, the MnFeCoNiCu system displayed the largest fraction of compositions that lie within the specified ranges for all criteria.

Phase II of the selection process aims to probe the composition space within an alloy system to seek compositions with an appropriate melting range. This was accomplished by high-throughput Scheil solidification simulations in the ThermoCalc software performed through the TC-Python interface. Figure 3.2(a) shows a subset of the solidification curves output from the simulation set on the MnFeCoNiCu system, indicating the variability of the solidification temperature range for compositions within the system. Based on this analysis, $Mn_{35}Fe_5Co_{20}Ni_{20}Cu_{20}$, with the Scheil curve identified in Figure 3.2(a), was identified as a specific candidate composition. Subsequent equilibrium thermodynamic calculations were employed to estimate the solidification temperature range for this composition under slow, furnace-cooled conditions. These calculations predicted a liquidus temperature of 1150°C and a solidus temperature of 1090°C, which were confirmed to match experimental differential thermal analysis results to within 10°C [2]. This solidification range renders the composition appropriate for brazing at 1200°C, which is approximately 150°C below the solidus temperature of Alloy 600 [13]. Note that predictions of phases that form upon solidification are also employed in Phase II to corroborate the Phase I filtration outputs.

Finally, Phase III examined whether selected compositions are robust in their single-phase stability after interactions with the superalloy substrate during brazing. As indicated by the isopleth phase diagrams in Figure 3.2(b-c), $Mn_{35}Fe_5Co_{20}Ni_{20}Cu_{20}$ possesses a high tolerance to dilution in Ni, and appreciable tolerance to dilution in Cr without forming second phases. Although as-solidified MPEA microstructures do not represent an equilibrium thermodynamic condition [80], the calculated phase diagrams can nonetheless offer insight regarding the robustness of single-phase stability.

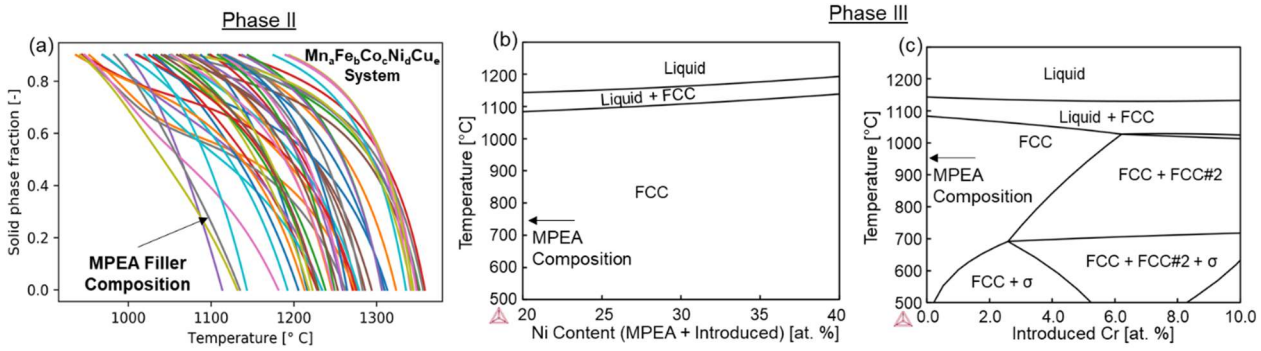

Figure 3.2: (a) A subset of the solidification curves output from high-throughput Scheil solidification simulations for the MnFeCoNiCu system in Phase II of the down-selection process; and isopleth phase diagrams in Phase III demonstrating the tolerance of the single-phase behavior of $Mn_{35}Fe_5Co_{20}Ni_{20}Cu_{20}$ to (b) Ni and (c) Cr diffused from substrate.

The initial feasibility study confirmed that this overall strategy was successful in selecting a viable filler composition [2]. For the $Mn_{35}Fe_5Co_{20}Ni_{20}Cu_{20}$ MPEA, the phase diagram is isomorphous with a narrow solidification range, and all the constituent MPEA elements diffuse into the substrate at similar rates [2], which prevents local supersaturation of a particular element. Neither postmortem microstructural characterizations nor in-situ examination of the MPEA solidification behavior [80] observed intermetallic phases in the braze, until a critical level of Cr diffuses from the base metal into the filler at extended braze holding time, e.g., for 120 min [2]. For joints brazed using optimized parameters, room temperature shear strengths of up to 530 MPa were reported for brazed lap joints in the original study [2]. However, cracked Ni-base superalloy components which are repaired and returned to service are more likely to exert tensile stresses on the filler, and operate at elevated temperatures. The objective of this study is to identify both room- and high-temperature tensile properties of the MPEA braze and compare directly to those of a conventional braze.

3.4 Experimental Methods

As illustrated in Figure 3.3(a), cylindrical rods of Ni-base Alloy 600, 9.53 mm (3/8-inch) in diameter and 50.8 mm (2 inches) long, were stacked vertically end-to-end and brazed to form a butt joint. Stainless steel fixturing was engineered to ensure good alignment, and Continental Braze Pro-Stop 700V was employed to prevent bonding to the fixture. Specimens were brazed using one of the two types of fillers: a 300 μm thick MPEA filler foil manufactured as detailed in [2], or a commercially available boron- and silicon-suppressed filler (BSSF) paste. The BSSF paste formed

by mixing powder with the nominal composition as listed in Table 3.1 [40] with Vitta Braz-Binder Gel-Grade ST in a ratio of 10 wt. % gel and 90 wt. % powder. For comparison, Table 3.1 also lists the nominal composition of the Alloy 600 base material [13]. No means of joint-clearance control was employed, as the rods were permitted to move freely in their axial direction, by virtue of a 0.005-inch radius difference with respect to the holes in the fixture plates. Brazing was performed in a high vacuum furnace employing a mechanically-backed diffusion pump, operating at a pressure no greater than 10^{-5} torr.

Table 3.1: Nominal composition (wt. %) of the BSSF filler [40], the MPEA filler, and the Alloy 600 base material [13]. Note that the MPEA nominal composition has been converted to wt. % for the sake of comparison with the other alloys.

	Ni	**Cr**	**Fe**	**B**	**Si**	**C**	**Mn**	**S**	**Cu**	**Co**
BSSF Filler	Bal.	7.0	3.0	3.1	4.5	-	-	-	-	-
MPEA Filler	20.2	-	4.8	-	-	-	33.0	-	21.8	20.2
Alloy 600	72.0 min.	14.0-17.0	6.0-10.0	-	0.50 max.	0.15 max.	1.00 max.	0.50 max.	0.50 max.	-

As the MPEA has a reported melting range of 1080-1150°C [2], and the melting range of the BSSF filler is 971-999°C [40], both are viable for brazing Alloy 600 (melting range 1354-1413°C) [13]. The optimum brazing temperature of 1200°C reported for the MPEA [2] was selected for both fillers in order to make a direct comparison. The MPEA joints were heated to 1200°C at a rate of 15C°/min and held for 90 minutes followed by a furnace cool, following the reported optimal thermal profile [2] (Figure 3.3(c)). To highlight the differences in filler performance under similar processing requirements, the BSSF brazing procedure outlined in Hawk's work [61] was selected because it closely mirrors the overall process time necessary for the MPEA brazing process. The thermal cycle for the BSSF joints (Figure 3.3(d)) involved intermediate holding stages during heating at 200°C to remove excess moisture in the paste, at 583°C for binder decomposition, and at 900°C for temperature equilibration. The heating rate was 15°C/min between each hold. The final brazing temperature was 1200°C, with a 10-minute hold time followed by a furnace cool. While these conditions do not represent a full-duration hold for isothermal solidification, they are representative of BSSF brazing processes in many industrial settings [61].

Specimens were either prepared for metallographic examination by diametrically cross sectioning the joint and polishing to a final step of 0.05 µm, or were machined into ASTM E8M round tensile specimens with a 6 mm gauge diameter and a surface finish of 32 µin (Figure 3.3(b)). Analysis of the microstructure and elemental distribution in the cross-section of the joints was performed with a JEOL 7000F field-emission scanning electron microscope (SEM) with an energy dispersive spectrometer (EDS), operating at 20 kV and 10 mm working distance.

Room temperature and 600°C elevated temperature tensile tests were performed at an engineering strain rate of $1x10^{-3}$ s^{-1} on an MTS Landmark 22.5 kip load frame equipped with a pyrometer-controlled induction furnace, water-cooled grips, and an elevated-temperature extensometer. Three tensile tests were performed for each condition. For the room temperature tests, digital image correlation (DIC) was used to generate strain partitioning maps. Prior to testing at 600°C, the pyrometer emissivity was calibrated against a K-type thermocouple contacting base material at the same surface finish as the tensile specimens. Specimens were held at 600°C for three minutes prior to initiating the tensile test. After testing, fracture surfaces were examined using an FEI Helios Nanolab 600i SEM.

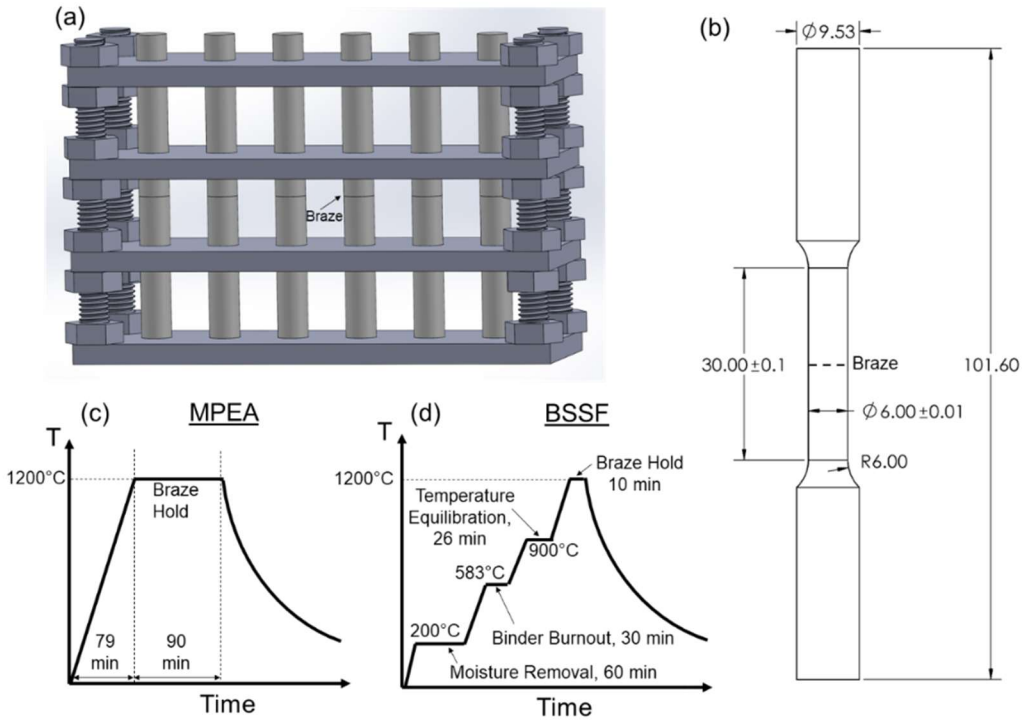

Figure 3.3: (a) Schematic illustration of the fixturing assembly employed during brazing. (b) Drawing of the ASTM E8M specimen machined from each butt joint, where the dimensions are in mm. (c-d) Thermal profiles employed for brazing with (c) the MPEA filler [2] and (d) the BSSF filler [61].

3.5 Results and Discussion

3.5.1 Braze Microstructure and Composition

Figure 3.4(a) and (b) illustrate macroscopic views of the MPEA and BSSF braze joints captured from optical microscopy. Secondary electron images and corresponding EDS element maps of representative areas of joint cross-sections are provided in Figure 3.4(c-f). Large circular pores in the BSSF joint can be observed in Figure 3.4(b). The pores in the MPEA joint are considerably smaller and only observable in the SEM micrograph as shown in Figure 3.4(c).

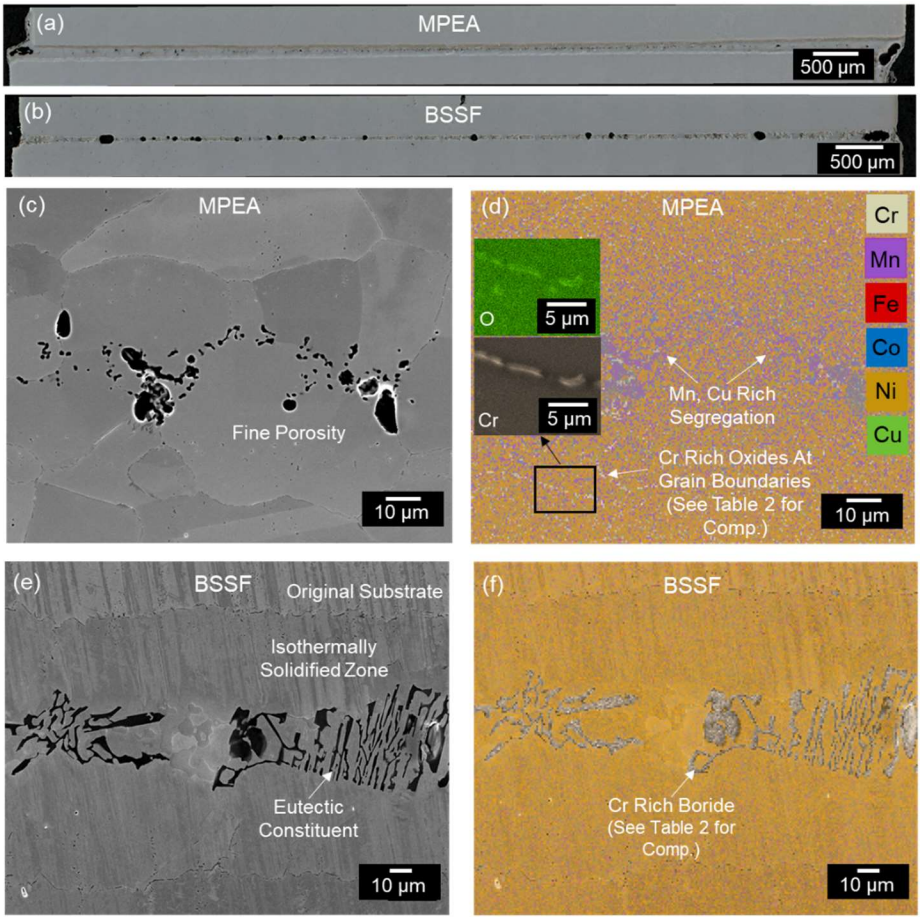

Figure 3.4: Optical micrographs of the braze cross-section of (a) MPEA joint and (b) BSSF joint. SEM micrographs and EDS element maps of representative braze cross-section of (c-d) MPEA joint and (e-f) BSSF joint.

As shown in Figure 3.4(e-f), taken from a region in between the larger pores visible in the macrograph, a Cr-rich boride phase is observed in eutectic constituents that populate the centerline of the BSSF joint. Boron is excluded from the EDS element map in Figure 3.4(f) due to the low

signal-to-noise ratio when detecting elements below carbon in atomic number using EDS. However, the estimated composition of the boride, determined using point-based EDS measurement with a higher signal-to-noise ratio, is provided in Table 3.2. The extent of the boride phase, limited to within approximately 20 μm of the joint centerline, indicates that some isothermal solidification likely occurred during the 10-minute holding cycle. However, isothermal solidification was incomplete, and the residual liquid solidified as a eutectic mixture at the joint centerline, as discussed in Figure 3.1(a). The isothermally solidified zone comprises a Ni-rich FCC solid-solution matrix as its primary microconstituent, although some diffusion-affected zone borides too small to be detectable in these EDS maps may additionally be present.

As indicated in Figure 3.4(c-d), the MPEA braze exhibits no harmful second phase formation in the solidification microstructure, although Mn and Cu segregation is observed at the centerline of the joint as detailed in [2, 80]. However, it is noted that Cr-rich oxide is observed to discontinuously populate grain boundaries, as shown in Figure 3.4(d). Of the constituent metallic elements, Cr and Mn have the greatest affinity for oxygen [101], which could explain why Cr preferentially oxidizes. The estimated composition of this oxide from point-based EDS is provided in Table 3.2. While the point-based data indicates more Ni than Cr in the assessed region, the particles are small enough that the EDS interaction volume likely encompasses both the particle and some of the surrounding matrix. Local Cr and oxygen enrichment in the particle is conclusively demonstrated in the EDS map insets provided in Figure 3.4(d).

Table 3.2: Compositions (at. %) of non-solid-solution particles appearing in either the MPEA or BSSF braze. Compositions represent an average of point-based EDS analysis, taken over five distinct particles.

Element (At. %)	**B**	**C**	**O**	**Mg**	**Al**	**Si**	**Ca**	**Ti**	**Cr**	**Mn**	**Fe**	**Co**	**Ni**	**Cu**
Cr-rich Oxide Particles at Grain Boundaries in MPEA Braze	-	9.1	56.6	-	-	-	-	-	5.1	4.8	3.0	2.6	17.5	1.2
Cr-rich Boride Particles in BSSF Cross-Section	69.3	-	-	-	-	-	-	-	28.9	0.6	-	-	1.2	-
Contaminant Particles on MPEA Fracture Surface	-	33.5	35.0	2.5	1.3	3.2	3.4	6.6	-	0.1	0.03	-	0.2	-

3.5.2 Mechanical Performance

Figure 3.5 summarizes the mechanical testing results for joints brazed with the MPEA and BSSF fillers. Figure 3.5(a-b) provide the individual engineering stress-strain curves for each specimen tested. The contour maps in the insets, along with Figure 3.5(c), directly compare strain partitioning behavior measured through room-temperature DIC. Figure 3.5(d) summarizes the statistical distribution of the mechanical properties for the two joints under both testing conditions. As indicated, the average total elongation for the MPEA-braze was 15.2% and 9.9% for room-temperature and 600°C testing, respectively, while elongation was limited to less than 1% for the BSSF-braze under both testing conditions. Variations in the apparent elastic modulus in Figure 3.5(b) are attributed to slip of the elevated-temperature extensometer, which was employed for both room-temperature and elevated-temperature tests. The DIC strain data demonstrate that the MPEA-brazed specimens underwent extensive yielding throughout the gauge length of the specimen, achieving a nearly uniform elongation of approximately 8%, as shown by the legend in the inset of Fig. 3.5(a). The more egregious strain localization at the braze interface, indicated in the DIC map, only developed late in the tensile test, as indicated by the supplementary DIC map data located in Appendix B. In contrast to the yielding observed throughout the MPEA-brazed specimens, the BSSF-braze only yielded in highly localized deformation within the joint (Figure 3.5(b)). Both specimens ultimately experienced interfacial failure.

Figures 3.6 and 3.7 provide a fractographic assessment of the mechanical behavior of the MPEA and BSSF braze fillers, respectively. As illustrated in Figure 3.6(a-b), dispersed contaminant inclusions with an irregular morphology up to 50 μm in size were observed on the MPEA braze fracture surface. The average composition of five of these particles is provided in Table 3.2. The composition indicates that the particles are mixed carbides and oxides of several contaminant elements, including Mg, Si, Al, Ca, and Ti, with low concentrations of any of the MPEA or Alloy 600 primary constituents. The presence of these contaminant elements indicates room for improvement in avoiding contamination of the manufacturing process described in [2]. Despite the contamination particles, the fracture surfaces of the MPEA braze are dominated by extensive regions of ductile microvoid coalescence, shown in Figure 3.6(c-d) and labeled as MVC in the figures. In contrast, no microvoid coalescence was identified in the BSSF fractographs displayed in Figure 3.7(a-b). Two features on these fracture surfaces can be correlated with the cross-sectional micrographs displayed in Figure 3.4. Circular features ranging from 20 μm to 50

μm in diameter (Figure 3.7(a)) are identified as the remnants of pre-existing pores at the braze interface visible in Figure 3.4(b). Clusters of second phase that possess a flower-like morphology, shown in Figure 3.7(a-b), are identified as the Cr-rich boride in Figure 3.4(e-f). The identity of these second-phases was confirmed through EDS analysis on the fracture surfaces.

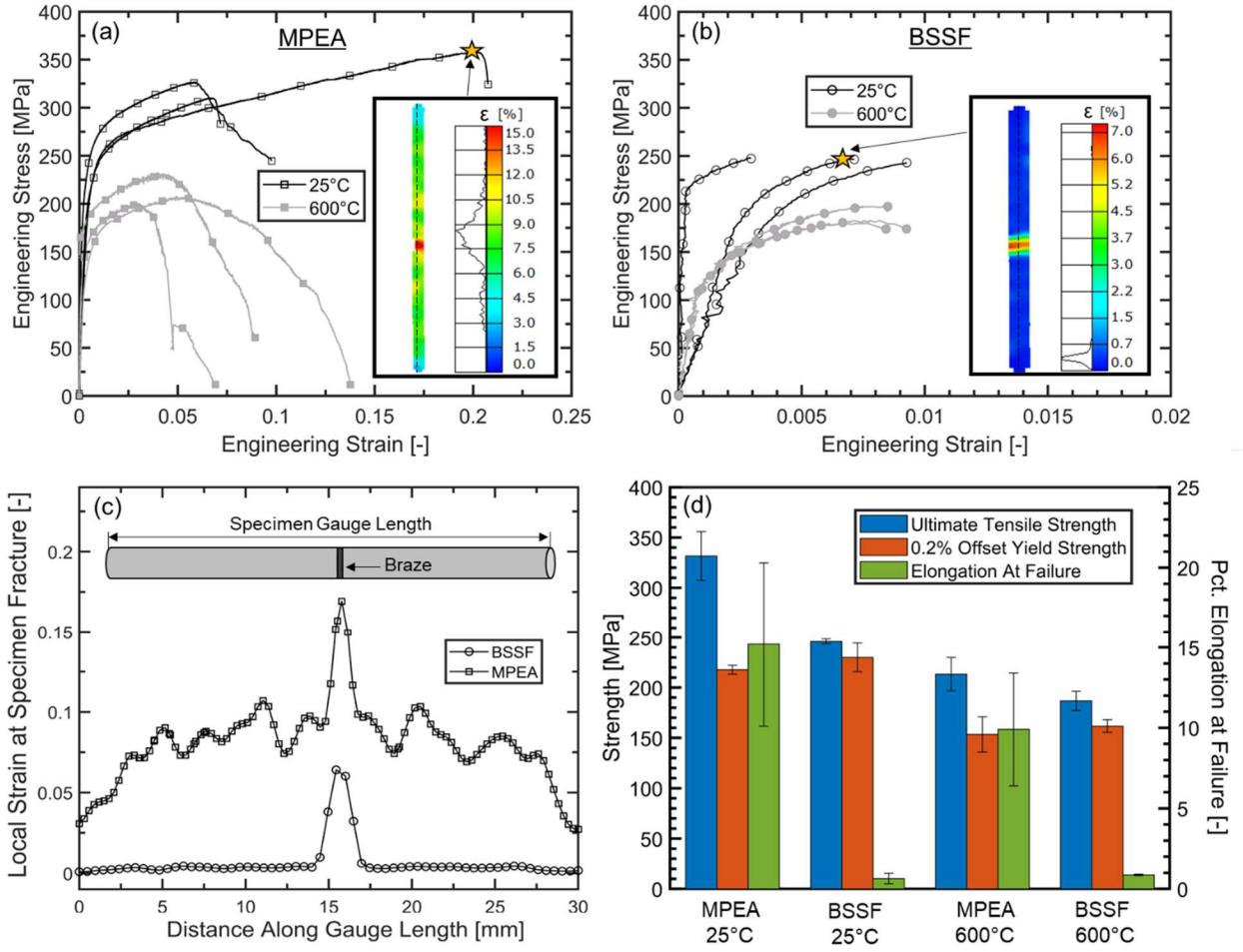

Figure 3.5: (a-b) Engineering stress-strain data for room-temperature tests and 600°C tests for joints brazed using (a) the MPEA filler and (b) the BSSF filler. Note the difference in the x-axis scaling. The insets show strain partitioning maps generated from digital image correlation, taken at the loading conditions indicated on the stress-strain curves. The adjoining plots in the insets qualitatively show the fractional distribution of the assessed area that experiences particular strain values. (c) Comparison of cross-sectional strain profiles at the locations indicated by the dashed lines in the insets in (a) and (b). (d) Summary of mechanical properties, with error bars representing one standard deviation.

Figure 3.7(c-d) show the BSSF fracture surfaces at higher magnification. Cracks were clearly observed adjacent to flat, planar features that possessed branching "river" markings around the borides. This set of features is consistent with crack nucleation and brittle cleavage fracture at

the interface between a boride particle and matrix. Cracks were not observed to nucleate from the pore remnants shown in Figure 3.7(a-b). Therefore, the microstructural feature dominating the failure mechanism of the BSSF braze was the Cr-rich boride phase, despite the porosity observed in Figure 3.4(b). Cleavage fracture in the matrix indicates that the toughness of this phase is also diminished from what would be expected of an FCC solid solution, which could indicate embrittlement from fine-scale diffusion-affected borides only identifiable in higher magnification characterizations. Brittle cracking through the eutectic borides indicates that the BSSF brazing process employed in this work can be considered sufficiently representative for the brazes to fail by the same mechanism commonly reported in literature [55, 56], although the amount of athermally solidified eutectics in this work may be more than the optimal or desirable level. It is ackowledged that substantially longer braze hold times would likely reduce the extent of the eutectic microconstituent containing the boride phase, by promoting additional isothermal solidification. However, as detailed previously, it is difficult to completely eliminate boride phases, as evidenced by the retention of diffusion-induced borides in the microstructure of a transient liquid phase bond, even after complete isothermal solidification was achieved [45]. It is also notable that the elongation of the MPEA braze reported in Figure 3.5 is greater than almost all reported values for brazes of Ni-base alloys employing conventional fillers [25].

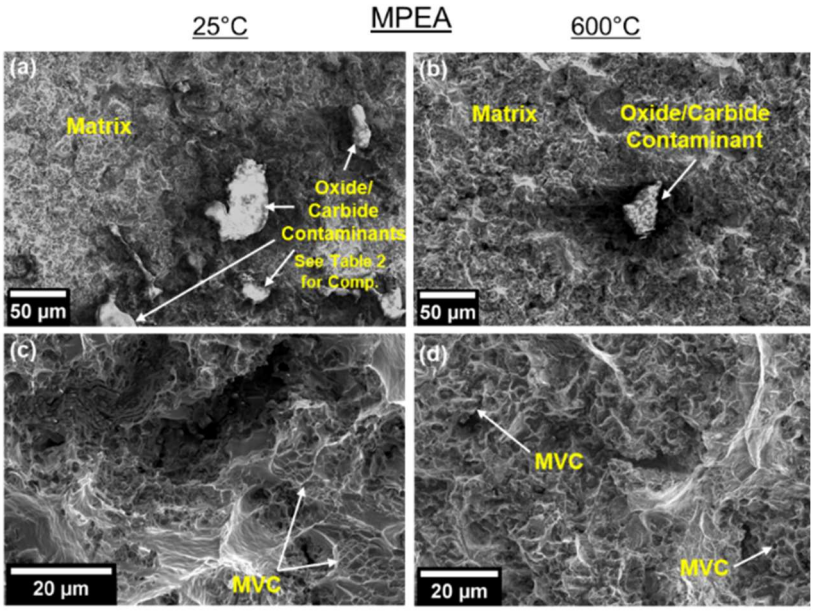

Figure 3.6: SEM micrographs of fracture surfaces following mechanical testing of the MPEA braze:(a-b) low-magnification images highlighting the presence of dispersed contaminant particles on the fracture surfaces. (c-d) Higher magnification images displaying ductile microvoid coalesence, labeled MVC in the figures. (a), (c) room temperature tests; (b), (d) 600°C tests.

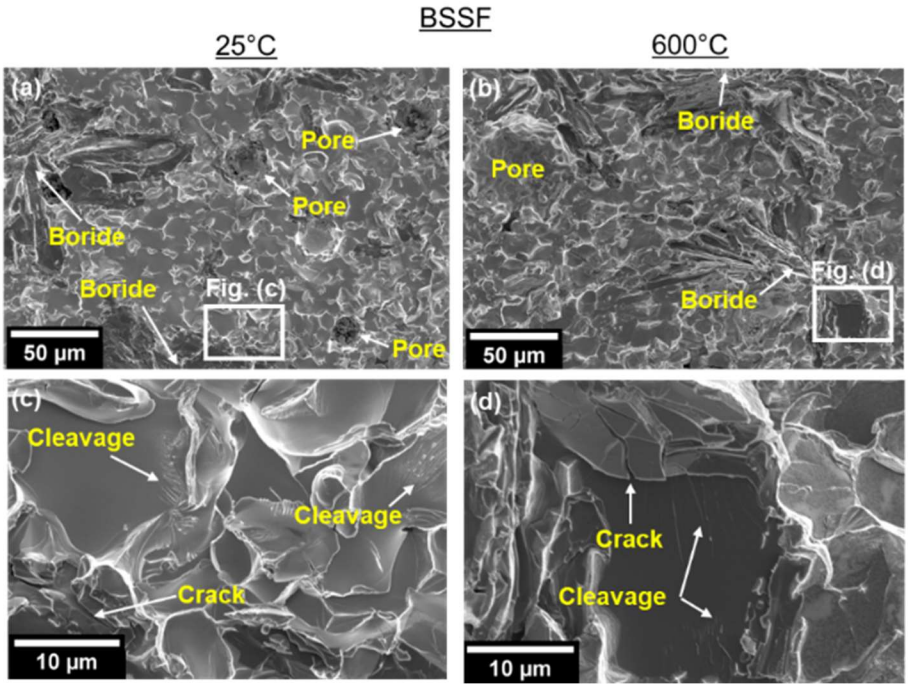

Figure 3.7: SEM micrographs of fracture surfaces following mechanical testing of the BSSF braze: (a-b) low-magnification images displaying boride phase clusters and pore remnants. (c-d) Higher magnification images indicating cracking through boride particles and brittle cleavage fracture. (a), (c) room temperature tests; (b), (d) 600°C tests.

No crack inititation sites could be easily identified via fractography on the MPEA braze fracture surface due to the extensive ductile microvoid coalesence. The elongation data in Figure 3.5(d) (green bars) and the individual stress-strain curves in Figure 3.5(a-b) indicate that the ductility of the MPEA braze, while always superior to that of the BSSF, exhibits considerable variation for both room-temperature and elevated-temperature tests. The inconsistent elongation demonstrated by the MPEA braze suggests inconsistency in the nature of stress concentrators and fracture nucleation sites contained within the braze. The irregular morphology of the porosity visible in the cross-section (Figure 3.4(c)), along with the broad distribution in size, suggest that this porosity may cause variable stress concentration and contribute to the scatter in the ductility. Alternatively, the presence of Cr-rich oxides along grain boundaries (Figure 3.4(d)) and the larger, dispersed oxide and carbide inclusions on the fracture surfaces of the MPEA braze (Figure 3.6(a-b)) could play a role in nucleating fracture and ulimate failure. If the large inclusions govern failure, it is likely that further improvement in performance could be achieved by developing a cleaner means of filler production. The current production method by arc-casting and cold rolling [2] is not yet optimized to mitigate contaminants and oxidation, as emphasized by the presence of

several contaminant elements (Table 3.2) in the fracture-surface particles. Regardless of which feature is primarily involved, the ductility data demonstrate that the MPEA filler possesses substantial tolerance to defects in the braze microstructure before failure is initiated.

The average yield strengths (red bars in Figure 3.5(d)) exhibited by the two braze specimens were comparable to within one standard deviation at both room temperature and 600°C, as indicated by the error bars. The ultimate tensile strength (blue bars in Figure 3.5(d)) was greater for the MPEA than the BSSF, due to the significant work hardening experienced during plastic deformation (Figure 3.5(a)). Thus, it is concluded that the MPEA braze offers superior ductility and comparable strength to the BSSF braze at both room temperature and 600°C, which together represent a marked improvement in the energy absorbed prior to failure in tension.

The room temperature yield strengths measured were 218 MPa for the MPEA braze and 230 MPa for the BSSF braze. These values are 33.4% and 35.2% of the measured value of 653 MPa for the Alloy 600 base material tested in the as-received condition. However, metallographic assessment performed on as-received Alloy 600 and material that was subjected to the MPEA brazing thermal cycle indicated that the majority of this reduction in yield strength could be attributed to grain growth in the base material. The grain size in the as-received condition was found to be 9 μm ± 1 μm, and the grain size in the material that underwent the thermal cycle was found to be 301 μm ± 83 μm. These data were analyzed in conjunction with a reported Hall-Petch type relationship for Alloy 600 [102], and it was found that this grain growth alone could account for 84% of the observed yield strength debit in the brazes. Considering the empirical nature of the Hall-Petch relationship, and the DIC data which indicated uniform initial yielding throughout the specimen gauge length (see Appendix B), it is reasonable to propose that observed yield strength reduction is fully accounted for by grain growth in the base material. Furthermore, a microhardness traverse performed on a braze joint employing the MPEA filler indicated a nearly uniform hardness profile acrosss the structure [2].

This combination of indicators suggests that there is no inherent weakness in the MPEA filler, and that higher joint yield strengths could be achieved when using alternative brazing methods that limit the heat input into base materials, or brazing other Ni-base superalloy materials that are more resistant to grain growth. It is further noted that the thickness of the MPEA braze is generally greater than that of the BSSF braze (Figure 3.4). Since thinner brazes typically experience greater strengthening contributions from triaxial constraint, it is noteworthy that the

thicker MPEA braze displays comparable strength to the thinner BSSF. Hence, applying this MPEA filler or further fine-tuned compositions to braze precipitation-strengthened superalloys is an area of promising future research. Additionally, the high-temperature testing matrix should be expanded in future studies to include higher operating temperatures (e.g. 800°C) that mimic the harsh operating conditions of the superalloy substrate. Creep and fatigue testing should also be performed in future studies to evaluate the endurance of the MPEA filler's beneficial mechanical properties in a working environment.

3.6 Conclusions

In summary, this study confirms that the metallurgical benefits of the new MPEA filler, as originally reported in [2], extend to tensile deformation at both room temperature and elevated temperature. The single-phase solidification behavior of the filler and the absence of brittle phases introduced by conventional MPD elements, offer comparable strength but vastly improved ductility over boron- and silicon-suppressed fillers. Extent of isothermal solidification is unimportant for the MPEA filler, offering ductile performance after relatively short process durations. Fractography on the specimens indicated that boride phases, not pores, were the primary factor limiting the ductility of the BSSF brazes. The superior tensile ductility exhibited by the MPEA braze is due to a single-phase FCC microstructure and fracture dominated by microvoid coalescence. The ductility could be further improved by cleaner filler production process with less oxides introduced and better controlled porosity in the MPEA braize. While joints brazed with both fillers exhibited yield strengths that were only fractions of that of the as-received base material, this discrepancy could be nearly wholly accounted for by grain growth in the base material during the brazing thermal cycle.

3.7 Chapter Acknowledgements

This research is supported by the National Science Foundation with Award no. 1847630. The authors would like to acknowledge Dr. Garrison Hommer for his assistance with the high-temperature tensile testing setup.

CHAPTER 4
INFLUENCE OF OXYGEN ON PERFORMANCE OF MULTI-PRINCIPAL ELEMENT ALLOY AS BRAZE FILLER FOR NI-BASE ALLOYS

Based on a paper submitted and in review at *Journal of Manufacturing Processes**

Benjamin Schneiderman[1], Alexander Hansen[1], Andrew Chihpin Chuang[2], Zhenzhen Yu[1]

4.1 Abstract

In manufacturing of multi-principal element alloys (MPEAs), the casting process is often a primary point of oxygen introduction to the material system, which was demonstrated by the laboratory scale button arc-melting process. Oxygen introduction raises concerns for the mechanical performance of these alloys if employed as structural materials alone or in engineering applications, such as serving as filler materials to enable joining of similar or dissimilar alloy pairs that are conventionally considered difficult to join. In this work, oxide inclusions in an as-cast off-equiatomic MnFeCoNiCu MPEA and Ni-base alloy braze joints made with this MPEA were evaluated by synchrotron X-ray diffraction mapping and electron microscopy. MnO was found to be prevalent throughout the cast MPEA and was chemically reduced during brazing by trace Al from the base material, Ni-base Alloy 600. Incomplete reaction of the MnO with Al, and some alternative reaction with Cr, left a mixture of MnO, Al_2O_3, and Cr_2O_3 in the as-brazed joint, with the oxides concentrated near the braze centerline due to directional solidification. In the braze joints, the non-oxide constituent phases detected were an FCC matrix and particles of $Cr_{23}C_6$, Cr_7C_3, and TiN which are all native to Alloy 600. The evolution of oxides within the brazed joints at elevated service temperatures of 600-800°C was also evaluated. While MnO and Al_2O_3 were stable during high-temperature service, Cr_2O_3 particles grew to several hundred microns, with dissolved oxygen in the MPEA providing a significant source for oxide growth. Comparing tensile performance of the as-brazed condition with post-service conditions showed that the evolution of oxide particles contributed to an increase in strength and decrease in ductility of the brazed joints.

---

* See copyright permissions appendix for permissions

[1] Colorado School of Mines, Golden, CO, 80401
[2] Advanced Photon Source, Argonne National Laboratory, Lemont, IL

Evaluating particle morphologies among fracture surfaces of individual specimens demonstrated that large Cr_2O_3 particles and continuous cluster networks of Al_2O_3 were the features most detrimental to total elongation. Hence, unmitigated evolution of oxygen-containing species during brazing and service conditions is detrimental to the ductility of the brazed joints, which highlights the importance of oxygen control in initial manufacturing of MPEAs for engineering applications.

4.2. Introduction

Multi-principal element alloys (MPEAs), which encompass high-entropy alloys (HEAs), have been gaining traction in the metallurgical community since 2004, when their potential beneficial effects were first published [63, 64]. Today, MPEA research continues to accelerate and diversify, and manufacturing methods to produce new compositions for study are expanding accordingly [103]. Powder metallurgy (PM) mechanical alloying techniques have emerged as a solid-state alternative for producing certain MPEAs [103-106], but the predominant manufacturing strategy remains casting from the liquid state. The most common MPEA casting method reported in literature is laboratory-scale button arc-melting, particularly in studies which examine a multitude of distinct novel compositions, requiring an inexpensive and rapid means of synthesis [78, 107-110]. In 2015, Jablonski et al. commented on several shortcomings of button arc-melting, including its tendency to result in solidification defects and macro-segregation, which cause variability in properties and are industrially unacceptable [111]. Vacuum induction melting (VIM) is a more relevant, industrial casting method preferred for solidification-sensitive alloys and critical applications that require strict compositional control. VIM offers more uniform solidification conditions [111] and better oxygen and trace element control, reducing the presence of microstructural defects and tramp elements when compared to “in air” casting processes [103]. Some recent MPEA studies have employed VIM for casting [112, 113], while others have incorporated induction melting in an inert gas environment [90].

Given the wide variability in manufacturing techniques and in the quality of fabrication equipment among various laboratory-scale research facilities, there is relatively little acknowledgment in the literature of the effects of contamination by atmospheric elements in MPEAs. There are two reasons for this lack of discussion: (1) MPEAs contain many elements of interest, such that contaminant interstitials are often ignored in compositional analyses [111], and (2) the majority of phase-stability research on MPEAs has been heavily focused on favoring solid

solution phases over intermetallic compounds [1], such that any minor carbide, nitride, or oxide phases are frequently disregarded. The role of these contaminant phases is gaining attention, however. Some of the recent studies on MPEA production by PM techniques trace the origins of oxygen contamination throughout their MPEA manufacturing process and comment on the role of oxide phases in performance [104-106]. A handful of studies on cast MPEAs acknowledge the presence of contaminant oxides in their microstructure, but usually do not correlate their presence directly with the manufacturing conditions [78, 111]. Choi et al. conducted a direct investigation of the effect of contaminant inclusions upon mechanical performance of the CrMnFeCoNi MPEA, achieving variable contamination levels and inclusion morphologies by altering the casting environment [114]. These authors demonstrated that fine oxide inclusions were more adverse to ductility, while coarse inclusions were more detrimental to ultimate tensile strength [114]. Thus, gaining better understanding of the effects of atmospheric element contamination and nature of the resultant inclusions is important for cast MPEAs for practical engineering applications.

Furthermore, recent studies on MPEA development as filler materials for joining applications indicated oxygen introduction into MPEAs during manufacturing is likely to adversely impact the mechanical performance of joined components as well. MPEA fillers developed for Ni-base alloy braze repair have included near-equiatomic MPEAs with added melting-point depressants [65-67] and off-equiatomic MPEAs designed to melt intrinsically at an appropriate temperature range for this application [2, 3, 68, 79, 115]. An off-equiatomic MPEA filler developed by the authors' research team for Ni-base alloy brazing, $Mn_{35}Fe_5Co_{20}Ni_{20}Cu_{20}$, has demonstrated success in avoiding brittle eutectic microconstituents and intermetallic phases, while providing comparable strength and far improved ductility over conventional fillers [115]. In brazing applications, cast MPEAs are designed to re-melt during filler delivery, experiencing non-negligible interactions with the base material in the process, and then be exposed to the high-temperature operating environment of the Ni-base alloy following brazing. Therefore, there are several opportunities for contaminant elements introduced during MPEA filler production to evolve within the system at elevated temperatures, possibly precipitating undesired phases that may adversely affect properties. The work in Chapter 3 has suggested that variabilities in the quantity and morphology of contaminant oxides are responsible for variations in the ductility of MPEA-brazed Ni-Alloy 600 structures in tension [115], similar to findings discussed for bulk MPEAs [114]. This work aims to perform a comprehensive assessment of the contaminant

particles present in the as-cast MPEA filler, and their evolution within the braze joints during brazing and subsequent service conditions. Synchrotron X-ray diffraction (XRD) and energy-dispersive spectroscopy (EDS) methods were used to examine the evolution of particles including carbides, nitrides, and oxides. The effects of contaminant phases on the mechanical performance of the MPEA-brazed structures were investigated.

4.3 Experimental Procedures

4.3.1 MPEA Filler Production and Oxygen Evaluation

Ingots of MPEA filler of approximate composition $Mn_{35}Fe_5Co_{20}Ni_{20}Cu_{20}$ were arc melted directly from pieces of its pure constituent elements on a water-cooled copper hearth, using a gas-tungsten arc welding electrode encased in a stainless-steel environmental chamber assembled in-house [2, 79]. Ingots were flipped and re-melted three times to ensure bulk compositional homogeneity. The chamber was evacuated with a mechanical pump and backfilled with ultra-high purity argon gas three times prior to each melt. However, the highest vacuum level achievable with this production setup was 0.9 torr, measured by a type-531 thermocouple pressure gauge, causing appreciable oxygen to remain in the chamber atmosphere. Prior to each melt, a piece of titanium metal was melted inside the chamber and held molten for 20 seconds to attempt to bind remaining atmospheric oxygen. After casting, ingots were milled to uniform thickness, removing all visible surface oxide. Subsequently, the oxygen and nitrogen content of the as-fabricated MPEA filler were estimated using a Leco TCH600 inert gas fusion elemental analyzer, calibrated using steel calibration samples with a known oxygen content of 200 ppm and nitrogen content of 535 ppm.

4.3.2 Brazing

Samples of Alloy 600 were furnace-brazed using MPEA foil cold rolled to a thickness of 300 μm. Brazing was conducted at a vacuum level of 10^{-5} torr or better as measured by an ion gauge, using a holding temperature of 1200°C and a hold duration of 90 min followed by furnace cooling, as described in [2, 115]. Two sample geometries were produced: a lap-joint of rectangular members with ¼-in thickness [2], and a butt-joint of cylindrical rods with 3/8-in diameter [115]. The butt-joint configuration employed stainless-steel fixturing and Continental Braze Supply Pro-Stop 700V stop-off to keep the members axially aligned [115]. In both cases, the joint clearance

was not fixed, and the plane of the joint gap was horizontal, with the uppermost Alloy 600 member allowed to weigh freely upon the molten MPEA filler during brazing [3].

4.3.3 Machining and Heat Treatment

Coupons 1 mm in thickness encompassing the entire braze cross-section were cut from the brazed lap-joints for characterization by synchrotron X-ray diffraction (XRD) and energy-dispersive spectroscopy (EDS). The cylindrical butt-joints were machined using a lathe into ASTM E8M round tensile samples with a gauge-section diameter of 6 mm and a 1 μm surface finish. After machining, some coupons and tensile samples were left in the as-brazed condition, while others were heat-treated in a Carbolite CWF-1200 open-air furnace at either 600°C or 800°C for 100 hours, followed by water quenching. The open-air environment was selected to simulate industrially relevant service conditions. Selected coupons were also heat treated in an evacuated quartz tube for comparison. The heat treatment temperatures were selected to simulate a range of possible operating conditions for Alloy 600 and other Ni-base superalloys to which the MPEA filler could be potentially applied [13, 18].

4.3.4 Characterizations

Both as-brazed and heat-treated tensile bars were mechanically tested to failure at room temperature on an MTS Landmark hydraulic load frame at an engineering strain rate of 10^{-3} s^{-1}. Following testing, sample fractography was performed using an FEI Helios Nanolab 600i scanning electron microscope (SEM), with low-magnification EDS mapping performed to identify the composition of particles on the fracture surfaces. After standard metallographic preparation with a final polishing step of 0.05 μm colloidal silica, both as-brazed and heat-treated 1 mm thick coupons cut from the lap joints were analyzed by optical microscopy and EDS, performed using a Tescan S8252G SEM.

Synchrotron XRD patterns were collected from the as-brazed and heat-treated coupons at beamline 1-ID-E of the Advanced Photon Source. A monochromatic beam with energy of 61.332 keV was directed in transmission through the 1-mm thick samples, with incident beam dimensions of 100 μm horizontally by 50 μm vertically. A Pilatus3X CdTe 2M hybrid photon counting detector with a sample-to-detector distance of 740 mm was used to collect patterns. The coupons were positioned with the plane of the braze horizontal and translated horizontally and vertically in

increments equal to the dimensions of the incident beam. This translation created a continuous spatial map of XRD patterns that extended 500 μm in either direction from the braze centerline, and laterally over the full width of the braze coupon. A description of sample alignment techniques including how the braze centerline was located is available in Appendix A.

Individual synchrotron XRD patterns were also collected from samples of the MPEA foil itself. To increase the diffracting grain population and achieve a near-powder pattern for easier observation of minor constituent phases, MPEA for synchrotron characterization was rolled at 400°C to 50% reduction in thickness, and subsequently recrystallized at 850°C for 2 hours in an evacuated quartz tube. This processing decreased the grain size from greater than 100 μm in the as-cast state to the range of 10 – 40 μm in the recrystallized state. Light surface oxidation occurred during the recrystallization treatment and was removed with SiC grinding paper prior to synchrotron characterization.

4.4. Results

4.4.1 Microstructure Evolution During Service

Figure 4.1(a) illustrates a synchrotron XRD pattern taken from the MPEA recrystallized as described above, plotted against the wavelength-independent reciprocal lattice vector $q = 2\pi/d$, where d is the interplanar atomic spacing. It should be noted that in previous diffraction studies within the as-cast MPEA [80], a strong solidification texture was observed along with obvious shoulder peaks corresponding to interdendritic segregation. The texture was eliminated by the recrystallization treatment, allowing for easier observation of minor phase peaks than the previous diffraction study on as-cast MPEA. The diffraction pattern is consistent with a major FCC phase containing MnO particles. Figure 4.1(b) provides a SEM image and corresponding EDS element maps of one such MnO particle. Figure 4.1(b) was generated from MPEA filler in the as-cast condition, proving that MnO particles are introduced in the casting process, before the recrystallization treatment employed for easier observation by XRD. Furthermore, the estimated total oxygen content of the as-cast MPEA by inert gas fusion elemental analysis was 1648 ± 160 ppm. While this quantity is only an estimate because it is far beyond the calibration curve provided by the steel calibrant, the oxygen content is certainly several times greater than 40-50 ppm, the level reported in MPEAs fabricated by VIM [111, 112]. The estimated nitrogen content of the

MPEA in this work was 2040 ± 241 ppm, which is also far greater than what could be achieved under optimal VIM conditions. Previous mechanical testing on the as-cast MPEA demonstrated a highly ductile deformation response despite the level of oxygen introduced during manufacturing [2], but the presence of MnO particles indicates that further improvements to performance are achievable with better environmental control.

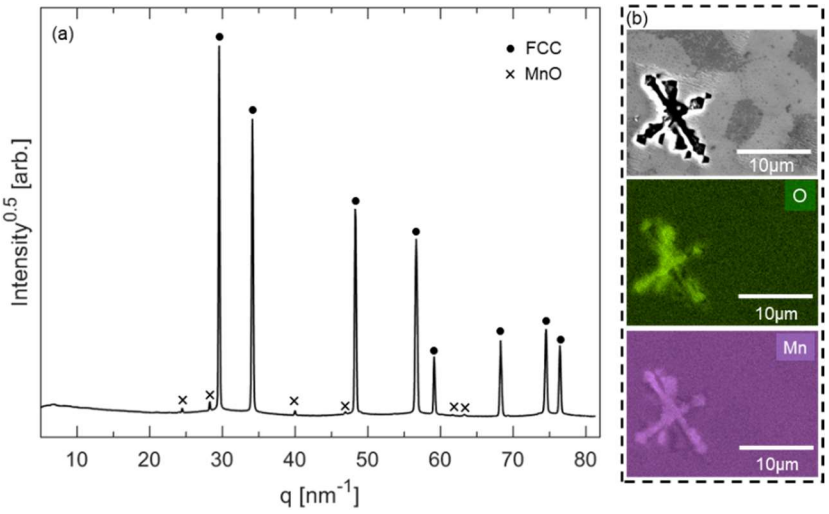

Figure 4.1: (a) Synchrotron XRD pattern taken from the MPEA following rolling at 400°C to 50% reduction in thickness and recrystallization at 850°C for 2h. (b) SEM image and EDS Mn and O maps of an MnO particle found in the as-cast MPEA.

Figures 4.2, 4.3, and 4.4 compile EDS and synchrotron XRD data from MPEA-brazed Alloy 600 coupons in the as-brazed condition, the 600°C-100h heat-treated condition, and the 800°C-100h heat-treated condition, respectively. Figures 4.2(a), 4.3(a), and 4.4(a) provide optical macrographs of the entire braze cross-section, with the grid of red rectangles indicating the size and position of individual incident beams used to construct the spatial maps of XRD patterns. Note that only a single row and column of beam positions is shown so that the macrograph is clearly visible, but spatial mapping was conducted in a grid over the entire rectangular area indicated by the dashed outline. For each sample, patterns were averaged laterally across the *y* dimension indicated in the figures. This analysis approach was undertaken to investigate how the constituent phases indicated by the XRD patterns varied over the spatial coordinate *x*, as indicated in the figures, where *x* is defined as the absolute value of the distance from the braze centerline.

In all cases, deviations from powder texture, along with compositional complexity, presented challenges in identifying constituent phases via automated software packages based upon the powder diffraction file. Instead, XRD peak positions were identified by fitting a Pearson

VII peak function [116] to the data. Peak positions were then compared to simulated patterns of likely constituent phases identified using composition information from EDS, and using published Alloy 600 technical data [13]. Simulated patterns were produced using GSAS-II [117]. Consistency of peaks among similar locations on the spatial map, the potential for peak shifting due to atomic substitution in a concentrated alloy environment, and the simulated powder intensities among candidate phases were all considered when identifying the phase that produced each peak. These details are described more completely in Chapter 5.

Figure 4.2(b-1) and (b-2) indicate that in the as-brazed condition, dispersed particles rich in Ti and N exist throughout the base material and the filler region, while dispersed particles rich in Al and O populate a region near the centerline. The segregation morphology most commonly presented among the major constituent elements is displayed, showing continuous (Mn, Cu) grain-boundary segregation along the immediate centerline in the filler region in Figure 4.2(b-8, b-10), thought to represent the last material to solidify [2, 3]. Figure 4.2(c-d) show selected EDS data demonstrating other phenomena found in as-brazed samples. Figure 4.2(c) shows a region with a much denser distribution of (Al, O) rich particles, while Figure 4.2(d) shows a region with no (Mn, Cu) segregation. Unsegregated brazes such as in Figure 4.2(d) are found intermittently among samples and usually occur in regions where the final thickness of the filler region is limited to under 200 μm, suggesting that there is a dependency of segregation on the local joint clearance. Joint clearance is uncontrolled in the brazing setup and may vary due to imperfect mating between faying surfaces.

In all conditions, XRD patterns display an FCC solid solution phase as the primary microstructural constituent for all locations across the joint (x axis in Figure 4.2(a)). As annotated in Figure 4.2(b-9), the measured lattice parameters are 3.631 Å for the (Mn, Cu) segregation region within the filler, 3.602 Å for the (Co, Fe) rich filler regions, and 3.561 Å for the Alloy 600 base material. Patterns such as that in Figure 4.2(e), taken from x = 250 μm, confirm the presence of TiN. Though Alloy 600 nominally contains no Ti, TiN is reported as a minor phase in its microstructure [13]. The peak positions for TiN are consistent at all values of x, indicating this phase is inert and displays little if any substitutional uptake of other elements from its environment. Figure 4.2(f) demonstrates the additional presence of three oxide phases – Cr_2O_3, Al_2O_3, and MnO – at the immediate centerline, with the Al_2O_3 phase being the most visible in the EDS data. $Cr_{23}C_6$, a reportedly stable carbide in Alloy 600 below 760°C, is also present [13]. The centerline XRD

pattern displays peak splitting resulting from simultaneous diffraction of the (Mn, Cu) and (Fe, Co) rich filler regions, segregation, which have a 0.8% disparity in lattice parameter, similar to the phenomenon reported in [80].

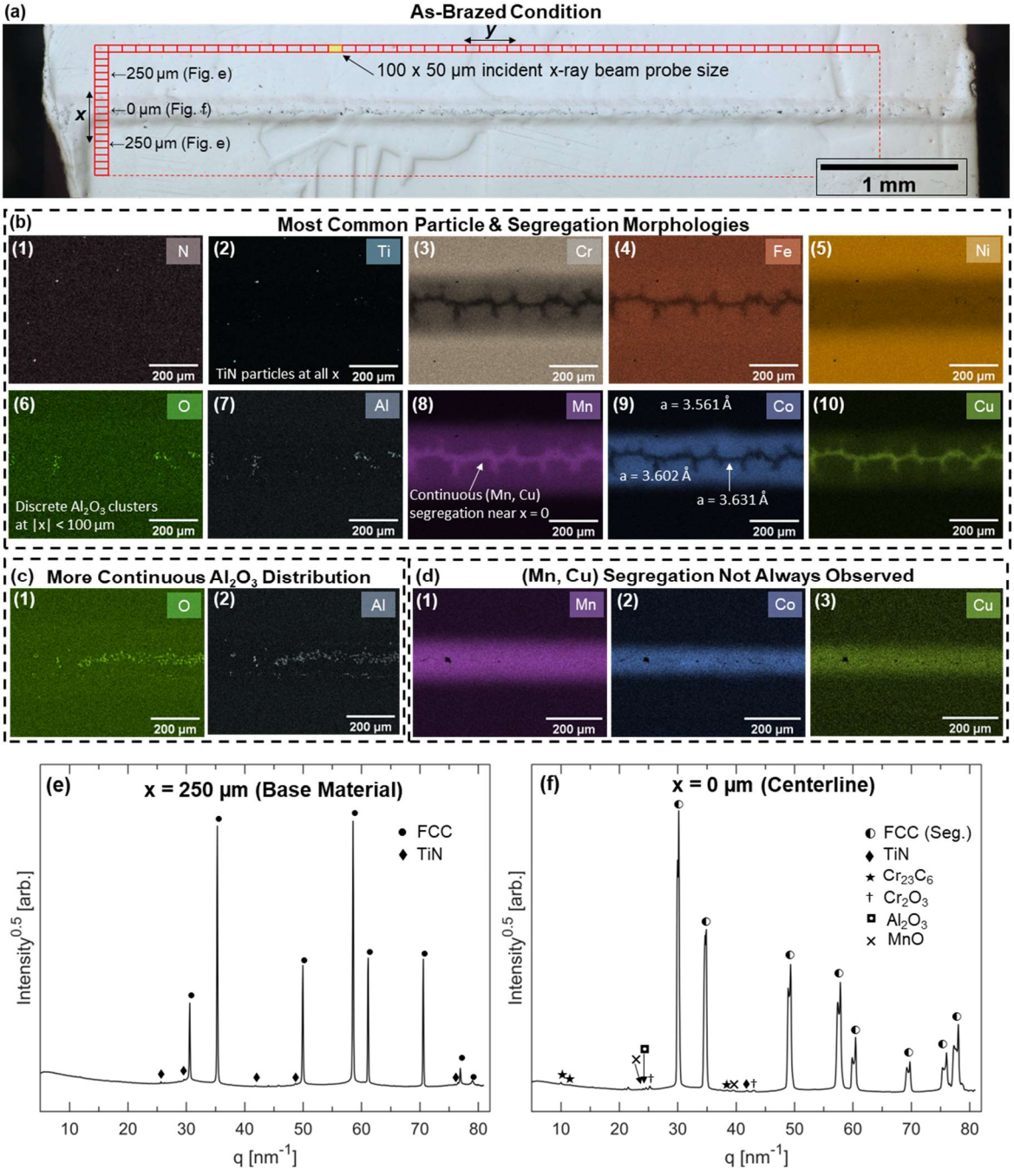

Figure 4.2: The as-brazed condition: (a) Optical macrograph with incident beam positions indicated by the red rectangles. (b-d) Selected EDS element maps displaying (b) the most common particles and segregation morphologies; (c) a region with a denser Al_2O_3 dispersion, and (d) a region with no (Mn, Cu) segregation. (e-f) Synchrotron XRD patterns collected at (e) x = 250 µm and (f) x = 0 µm.

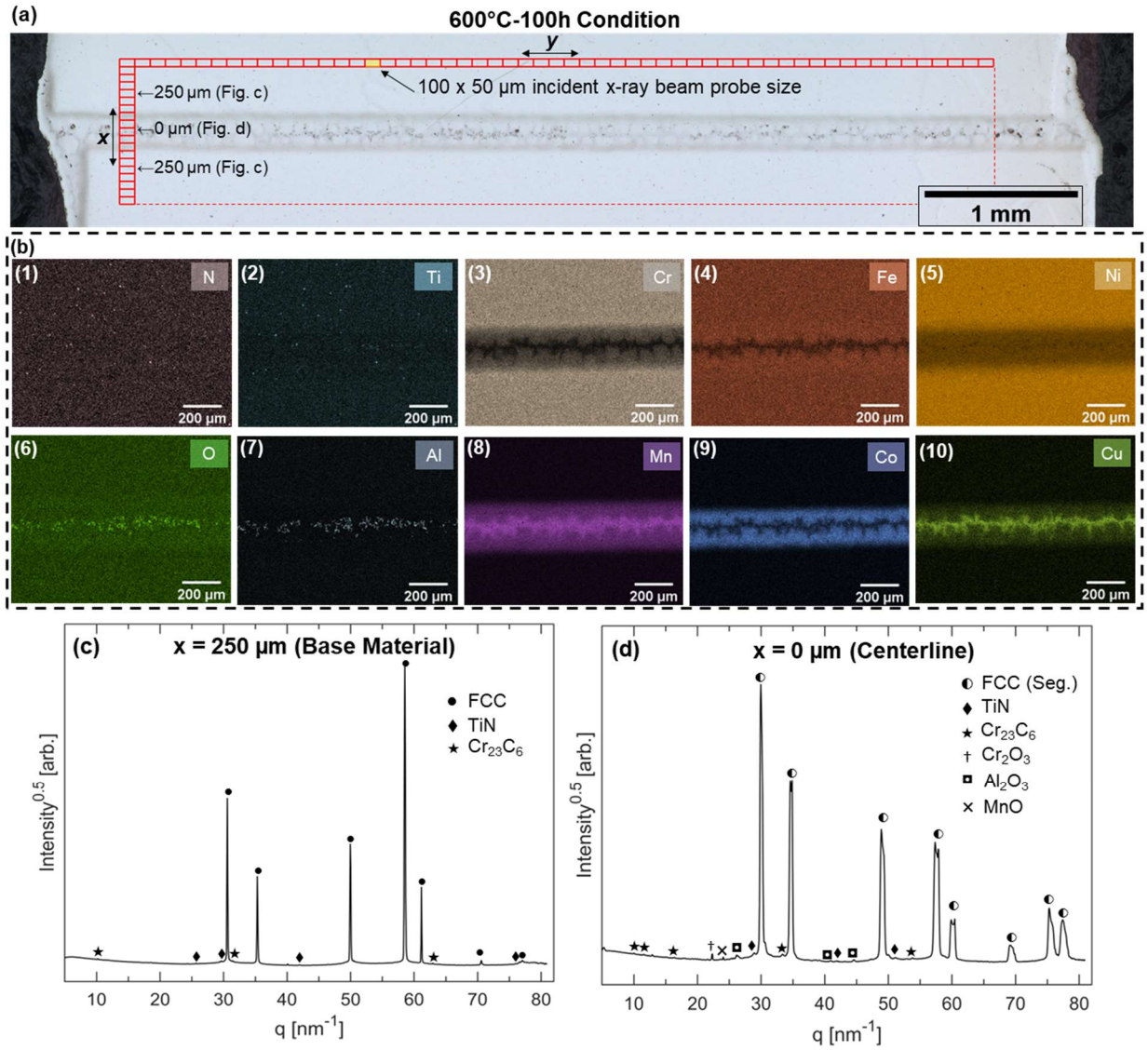

Figure 4.3: The 600°C-100h condition: (a) Optical macrograph with incident beam positions indicated by the red rectangles. (b) EDS maps showing element distribution in this condition. (c-d) Synchrotron XRD patterns collected at (c) x = 250 µm and (d) x = 0 µm.

As seen in Figure 4.3(a-b), little change relative to the as-brazed condition is observed after 100 hours at 600°C in either the optical macrograph or the EDS data. Figure 4.3(c) demonstrates that very small $Cr_{23}C_6$ peaks were observed in the base material following this heat treatment, and Figure 4.3(d) illustrates the centerline presence of the same three oxide phases as in the as-brazed condition.

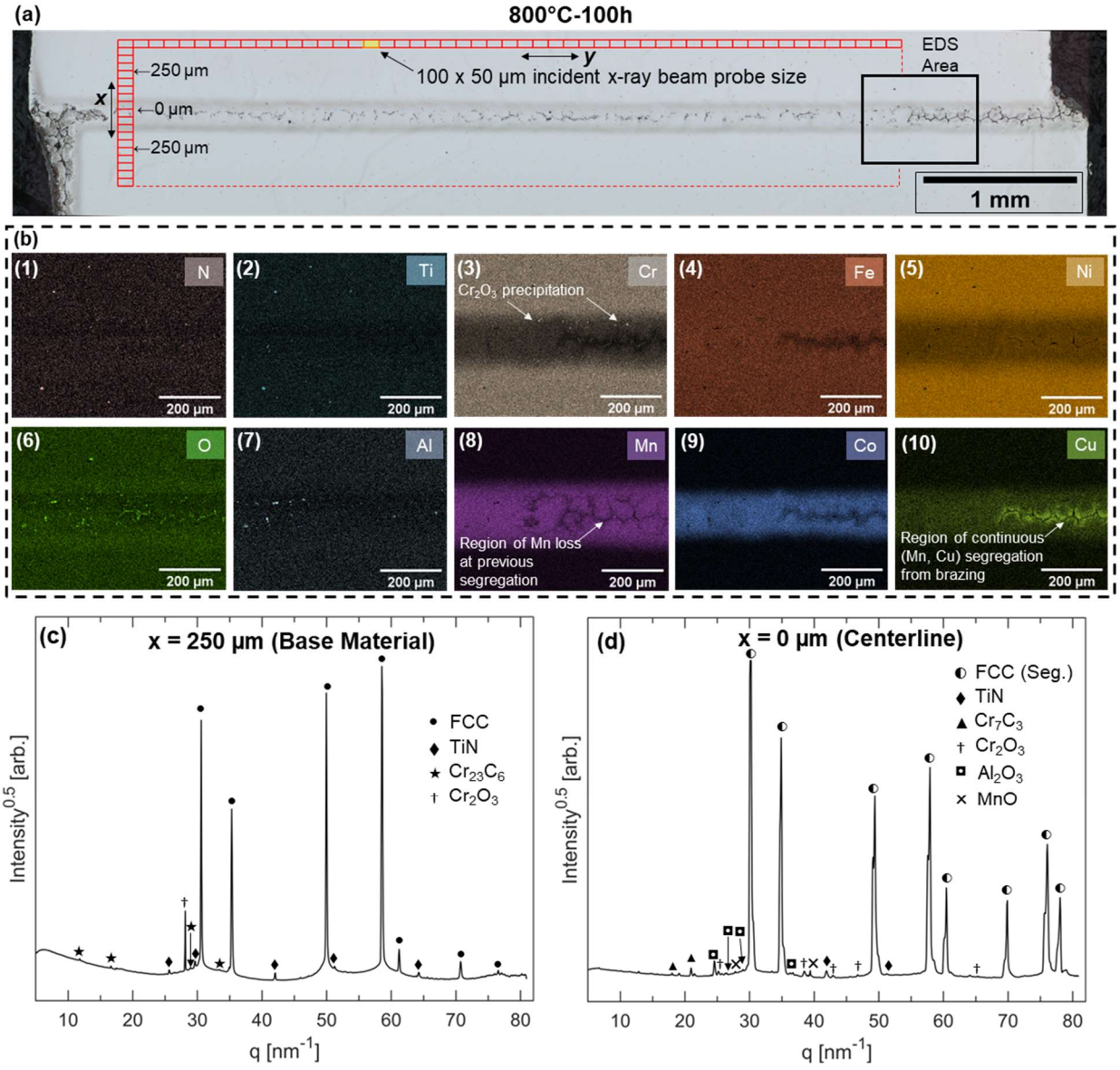

Figure 4.4: The 800°C-100h condition: (a) Optical macrograph with incident beam positions indicated by the red rectangles and EDS map area shown by the black rectangle. (b) EDS element maps displaying the most common particle and segregation morphologies. (c-d) Synchrotron XRD patterns collected at (c) x = 250 µm and (d) x = 0 µm.

Figure 4.4 indicates that more significant changes occur during the 100-hour heat treatment at 800°C. Cr_2O_3 and Al_2O_3 precipitation during heat treatment is evident in both EDS and XRD data. Particles rich in both chromium and oxygen are observed in Figure 4.4(b-3, b-6), while Figure 4.4(c) shows that some large Cr_2O_3 peaks are observed in XRD patterns extending into the base material. Figure 4.4(d) shows that Cr_2O_3, Al_2O_3, and MnO are all still present at the centerline. The

EDS data in Figure 4.4(b-8) also shows a depletion of Mn along grain boundaries that were previously enriched in Mn and Cu, and remain enriched in Cu after heat treatment, as shown in Figure 4.4(b-10). Mn is the most volatile constituent element of the filler, with a vapor pressure of 1.6×10^{-4} torr at 800°C, 1000 times greater than that of Cu, the next most volatile constituent [118]. This volatility makes Mn prone to vaporization in certain regions where Mn is segregated along grain boundaries that are connected to the specimen surface (see Figure 4.4a). This vaporization is limited in extent to regions that possess a continuous (Mn, Cu) segregation in the as-brazed state, as is evident by the absence of Mn depletion on the left-hand side of Figure 4.4(b-8), where the Cu segregation in Figure 4.4(b-10) is also absent. Cu-segregation is left unchanged by heat treatment.

Figure 4.5 compares the spatially dependent intensities of the maximum XRD peak for each non-major phase in the as-brazed condition and the two heat-treated conditions. The approximate extent of the MPEA filler in *x* is denoted. As indicated, the minor phases that formed during brazing and service were limited to nitrides, carbides, and oxides, with no intermetallic phases detected. While a Rietveld refinement to quantitatively calculate phase fractions was not feasible because of the same challenges that prevented automated phase identification, Figure 4.5 offers a semi-quantitative comparison of the phases observed in all three conditions. The size, volume fraction, and proximity to an orientation meeting the Bragg condition for discrete particles all play a role in determining intensity.

Figure 4.5(a-c) illustrate the incorporation of TiN, $Cr_{23}C_6$, and Cr_7C_3 – three phases native to Alloy 600 [13] – into the MPEA filler region. TiN and $Cr_{23}C_6$ are present at all *x* across all three conditions, while Cr_7C_3 appears more intermittently. Heat treatment at 600°C almost completely suppresses the Cr_7C_3 phase, while it is more prevalent in the as-brazed condition and after heat treatment at 800°C. This behavior is consistent with the reported favorability of Cr_7C_3 above 760°C [13]. For TiN and $Cr_{23}C_6$, the highest intensity generally occurs in or near the filler region, which may indicate concentration and/or growth of these particles within the filler due to high nitrogen and potentially carbon content in the cast MPEA.

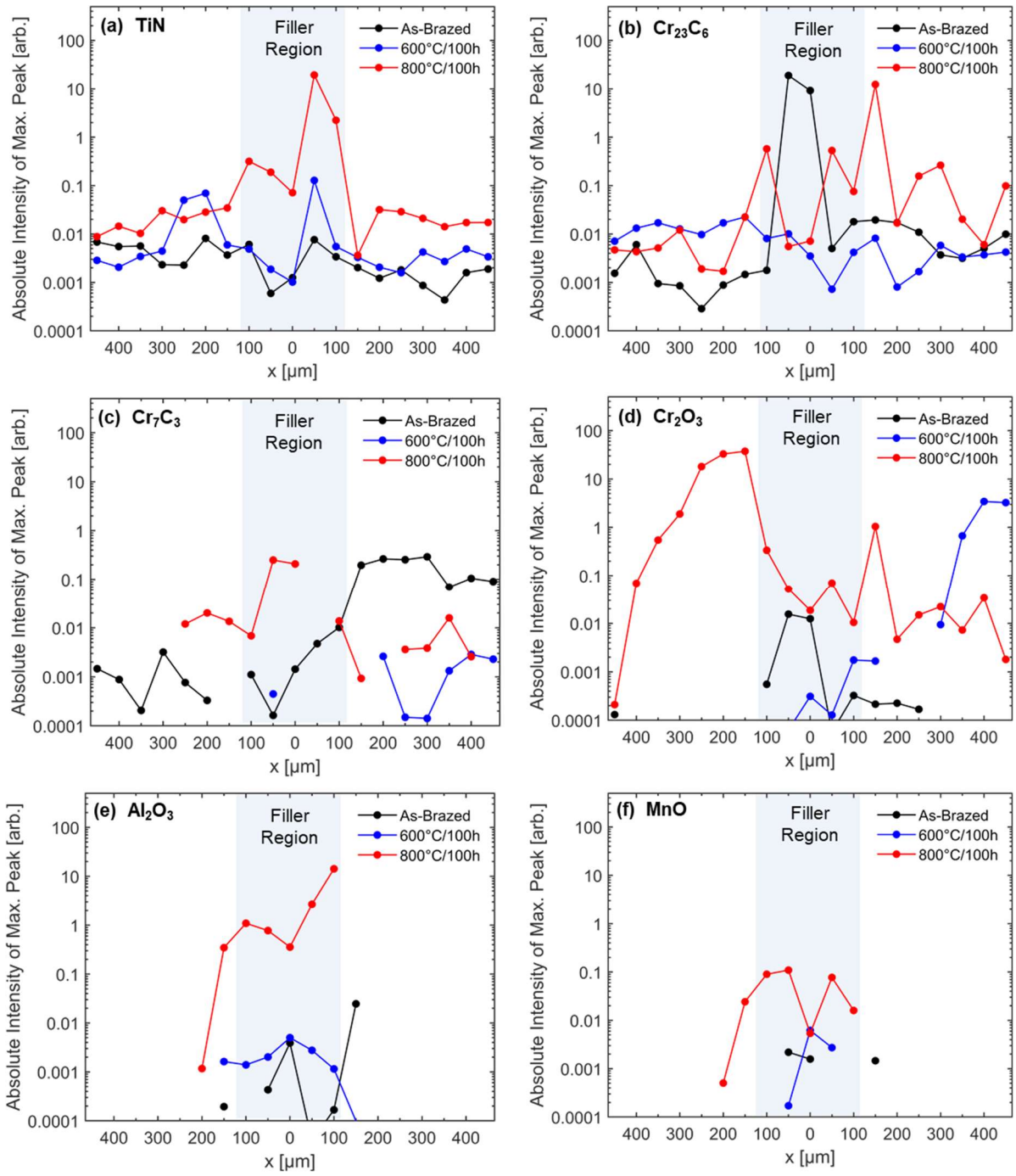

Figure 4.5: Intensities of the maximum peak for each minor phase identified as a function of distance from the braze centerline for the as-brazed condition and two heat-treated conditions. (a) TiN. (b) $Cr_{23}C_6$. (c) Cr_7C_3. (d) Cr_2O_3. (e) Al_2O_3. (f) MnO.

The behavior of the oxide phases in Figure 4.5(d-f) is the most important takeaway from Figure 4.5. Al_2O_3 and MnO are only found at $x \leq 200$ μm, approximately coincident with the filler region. The intensity of these two oxide phases is comparable between the as-brazed condition and

the 600°C-100h condition, but a notable increase in the intensity of both phases is observed after heat treatment at 800°C, which may indicate some growth of Al_2O_3 and MnO particles at this temperature. Cr_2O_3 is present further from the centerline than either Al_2O_3 or MnO in all conditions, owing to the abundance of Cr in the base Alloy 600. In the as-brazed condition, the intensity of Cr_2O_3 is small and usually limited to near the centerline. After heat treatment at 600°C, more intense Cr_2O_3 peaks are observed in a few patterns extending up to x = 450 µm, while after heat treatment at 800°C, these large Cr_2O_3 peaks are more consistent and widespread. The data are consistent with the precipitation of some Cr_2O_3 particles during 600°C heat treatment and more numerous or larger Cr_2O_3 particles during 800°C heat treatment.

4.4.2 Effect of Oxides on Mechanical Performance

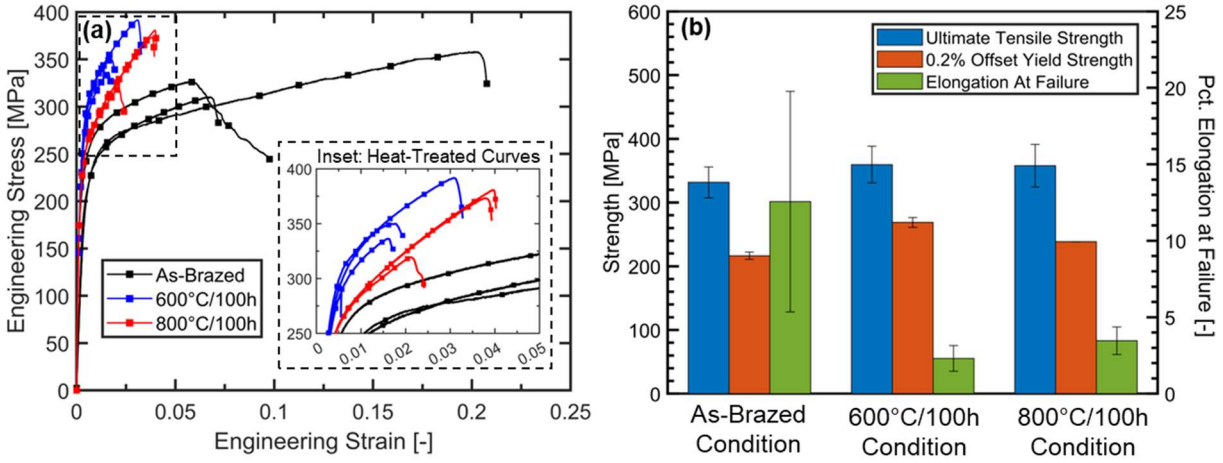

Figure 4.6: Comparison of tensile data for the as-brazed, 600°C-100h, and 800°C-100h conditions. (a) Individual engineering stress-strain curves from mechanical testing; (b) summary of ultimate tensile strength, yield strength, and total elongation for the three conditions.

Figure 4.6 summarizes the results of mechanical testing on the MPEA-brazed Alloy 600 tensile bars machined from butt joints for the as-brazed, 600°C-100h, and 800°C-100h conditions. All samples failed at the braze interface. A slight increase in both yield strength and ultimate tensile strength (UTS) of the brazes was observed following either heat treatment, alongside an accompanying decrease in ductility. Overall, the specimens heat treated at 600°C demonstrated slightly higher strength and lower ductility than those heat treated at 800°C. The mean yield strength increased from 217 MPa in the as-brazed condition to 269 MPa after heat treatment at

600°C and 238 MPa after heat treatment at 800°C. The UTS followed a similar trend, increasing from 332 MPa in the as-brazed condition to 360 MPa after 600°C-100h and 358 MPa after 800°C-100h. The mean total elongation decreased from the as-brazed value of 12.5% to 2.3% in the 600°C-100h condition and 3.5% in the 800°C-100h condition. As indicated by the inset of Figure 4.6(a), significant variability in the total elongation was observed among specimens in each heat-treated condition, as well as in the as-brazed condition shown in the main part of the figure.

To understand the variability in performance among the heat-treated specimens, fractography was performed on the best-performing and worst-performing specimen in each condition. Figure 4.7 shows low-magnification SEM micrographs and corresponding EDS element maps for Cr, Al, and O for each of these specimens. Though it is not a quantitative technique when performed on a tortuous fracture surface, EDS can nonetheless assist in identifying particles on the fracture surfaces. These EDS maps supplement the assessments of the oxide phases from cross-sectional EDS and synchrotron XRD discussed in Section 4.4.1 and offer insights into the mechanical performance of the specimens.

Figure 4.7(a) shows that few Cr_2O_3 particles and discrete clusters of Al_2O_3 exist on the fracture surface of the best-performing specimen in the 600°C-100h condition. For the worst-performing specimen in this condition (Figure 4.7(b)), numerous Cr_2O_3 particles up to 200 μm in length are observed, alongside a continuous network of Al_2O_3. The inconsistent precipitation of Cr_2O_3 at 600°C agrees with the XRD peak intensity data in Figure 4.5(d). Figure 4.7(c-d) show that large Cr_2O_3 particles are found on fracture surfaces of both the best-performing and worst-performing specimens heat treated at 800°C, with the largest particles exceeding 500 μm in length, in agreement with the widespread high Cr_2O_3 intensity in Figure 4.5(d). The Al_2O_3 distribution was found to be similar between the two fracture surfaces in Figure 4.7(c) and (d), consisting of discrete clusters of particles. However, the worst-performing specimen heat-treated at 800°C also displayed a region of incomplete fill, a brazing defect identifiable by the preserved dendrite tips observable to the right of the yellow dashed line in the SEM micrograph in Figure 4.7(d). This brazing defect, caused by imperfect surface mating and serving as a pre-existing crack during tensile testing, was determined by macroscopic fractography to encompass 6.7% of the fracture surface by area. This finding explains the lower ductility demonstrated by this specimen (see inset of Figure 4.6a).

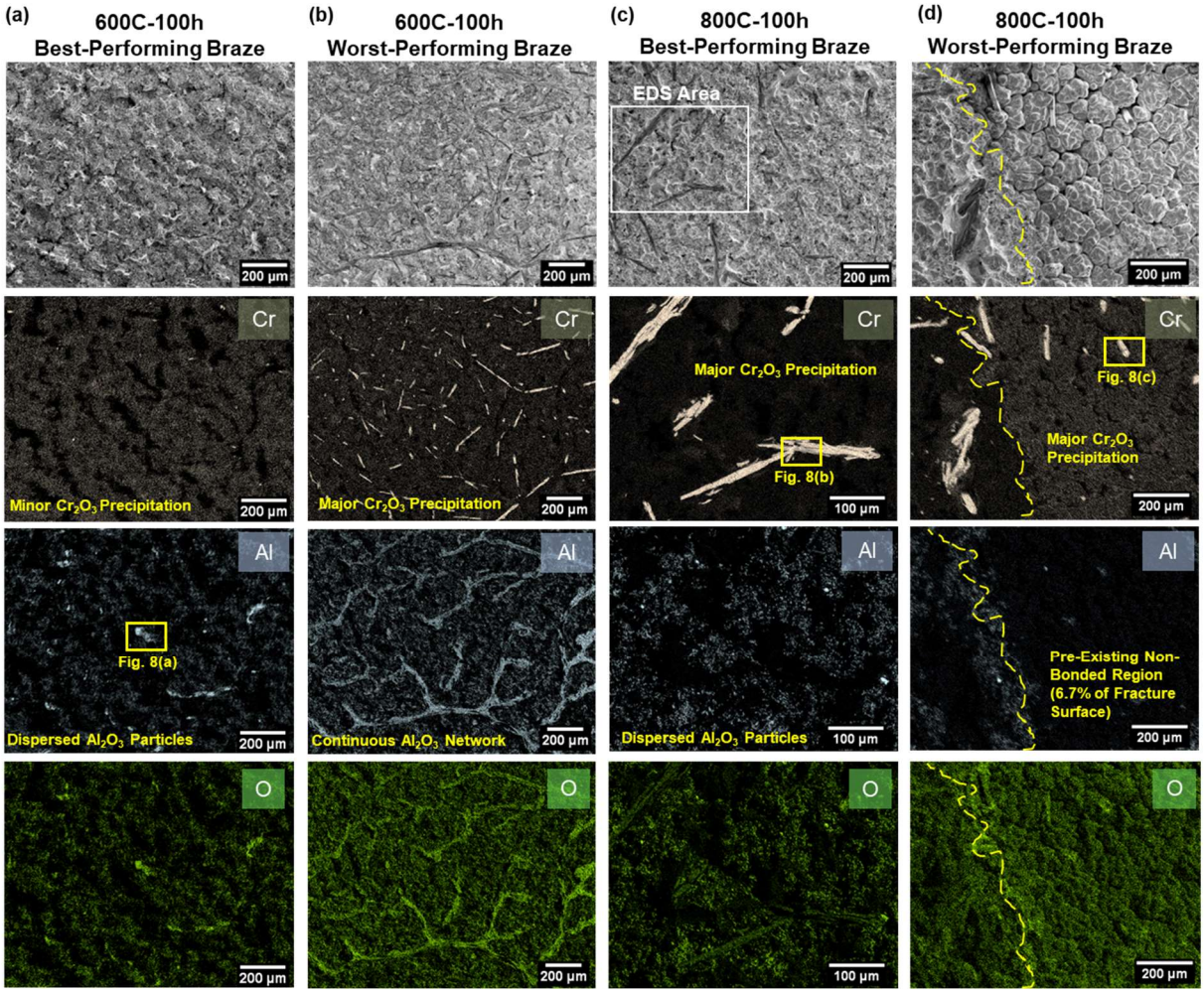

Figure 4.7: Low magnification SEM fractography images and corresponding EDS maps for Cr, Al, and O for tensile specimens heat treated at (a-b) 600°C-100h and (c-d) 800°C-100h. (a, c) Best-performing tensile specimens; (b, d) worst-performing tensile specimens.

Figure 4.8 shows higher magnification SEM images of the regions indicated in Figure 4.7. Figure 4.8(a-b) demonstrate brittle cracking through a fractured Al_2O_3 particle and Cr_2O_3 particle, respectively. In contrast, the surrounding matrix phase displays ductile microvoid coalescence (labeled MVC), indicating the oxides play a role in limiting the ductility of the heat-treated brazes. The region of incomplete fill in Figure 4.7(d) allows for the examination of particles in their unfractured state. An unfractured Cr_2O_3 particle is shown in Figure 4.8(c). This figure indicates the particles are rod-like in morphology with hexagonal crystallographic facets. The hexagonal facets further assist to positively identify the large Cr-rich particles visible in EDS as Cr_2O_3, which has a trigonal crystal structure within the hexagonal crystal family and can produce hexagonal

facets [119]. In contrast, $Cr_{23}C_6$ and Cr_7C_3 are cubic and orthorhombic, respectively [119], and thus neither carbide phase is capable of producing the observed hexagonal morphology. Smaller Cr-rich particles, identified by EDS and believed to be chromium carbides, also decorate the surface of the incomplete fill region and are visible in Figure 4.8(c).

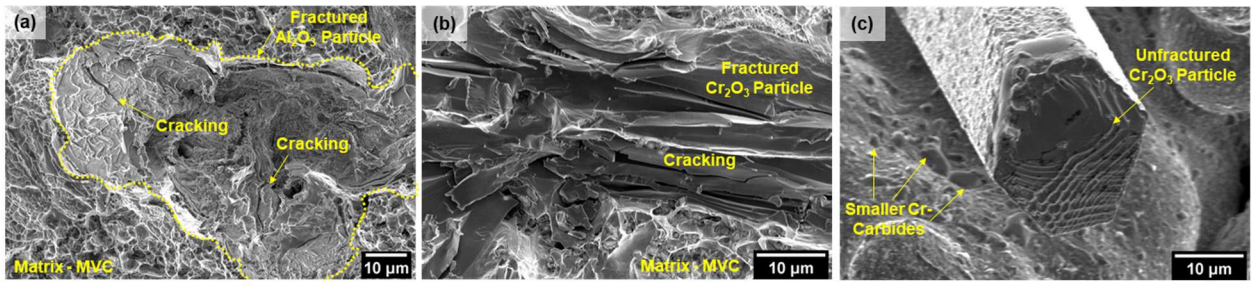

Figure 4.8: Higher magnification SEM micrographs of fracture surface particles. (a) Fractured Al_2O_3 particle from the region indicated in Fig. 4.7(a). (b) Fractured Cr_2O_3 particle from the region indicated in Fig. 4.7(c). (b) Unfractured Cr_2O_3 particle from the region indicated in Fig. 4.7(d).

4.5 Discussion

The maximum vacuum capability of 0.9 torr in the MPEA production chamber, the presence of MnO in the as-fabricated MPEA, and the estimated oxygen content of 1648 ± 160 ppm all indicate insufficient control of atmospheric oxygen during MPEA production. Little additional oxygen introduction is likely during brazing, as the brazing chamber is held at much higher vacuum (10^{-5} torr). During exposure to service conditions in the open air, environmental oxygen atoms may diffuse from the surface to the interior of the braze along grain boundaries or defect networks, and oxygen atoms dissolved in the FCC matrix may precipitate oxides to alleviate supersaturation as the system evolves toward equilibrium. Cr_2O_3 was observed to precipitate in specimens heat treated in an evacuated quartz tube in addition to those heat treated in the open air. This finding indicates that oxide precipitation during simulated service results primarily from the diffusion of excess dissolved oxygen rather than from environmental introduction. Furthermore, the size of the observed oxide particles on fracture surfaces was not generally a function of distance from the specimen surface. If oxygen diffusing from the furnace environment were the primary source for precipitation, larger oxide particles would generally populate more superficial regions.

Figure 4.9 provides a schematic illustration of the behavior of oxygen in the MPEA-Alloy 600 system after it has been introduced through MPEA filler production. Before brazing (Figure 4.9a), MnO is the preferred oxide in the as-fabricated MPEA because Mn has the greatest affinity

for oxygen out of the MPEA constituents according to the Ellingham diagram [120]. Given the high estimated oxygen content and non-equilibrium solidification of the MPEA during production by casting, the matrix is also supersaturated in dissolved oxygen, indicated by the dark blue color in Figure 4.9(a).

During brazing (Figure 4.9b), a degree of substrate dissolution will occur [39, 115], diluting the total oxygen concentration in the molten filler and introducing Al from the Alloy 600 base material. Although Alloy 600 does not nominally contain Al, no maximum Al content is indicated in its compositional specification [13]. Furthermore, the material is produced in the same facilities as other Ni-base superalloys containing Ti and Al as γ'-formers, allowing some degree of cross-contamination to occur. Even trace Al contamination can result in Al_2O_3 formation, owing to the strong affinity of Al for oxygen, as indicated by the Ellingham diagram [120]. This phenomenon is well-documented in literature. Choi et al. found Al_2O_3 inclusions to occur in as-fabricated CoCrFeMnNi MPEAs as the result of trace Al impurities with an average concentration of 800 ppm among the nominally pure constituent elements [114]. A mixed Mn-Cr-Al oxide was observed in the same MPEA at Al concentrations as low as 130 ppm [113]. Thus, during the braze hold, trace Al from Alloy 600 chemically reduces MnO via the reaction

$$2Al + 3MnO \rightarrow 3Mn + Al_2O_3 \quad (4.1)$$

causing pre-existing MnO particles to shrink at the expense of Al_2O_3 precipitation, as illustrated in Figure 4.9(b).

When the braze hold is terminated, directional solidification often occurs (Figure 4.9c) [2], causing the segregation observed in Figure 4.2(b). Oxides which float in the liquid are carried to the braze centerline and coagulate there, explaining the Al_2O_3 distribution in the as-brazed condition observed in Figure 4.2(b-c). Figure 4.5(a) indicates the presence of MnO and Cr_2O_3 near the centerline as well; they occur because there is only a trace amount Al in the system, which is insufficient to bind all the contaminant oxygen. With the Ti in the system bound in inert TiN particles, the Ellingham diagram indicates the elemental species with the next-greatest affinity for oxygen are Mn and Cr, whose affinities are similar [120]. MnO particles are likely those present in the original MPEA filler that did not undergo complete reaction with Al, while Cr_2O_3 results from new precipitation, which is possible because substrate dissolution has introduced significant Cr to the molten filler.

Following non-equilibrium solidification after brazing, the filler region remains significantly supersaturated in dissolved oxygen atoms, allowing the growth of existing oxides and the precipitation of new ones during high temperature service (Figure 4.9d). Figures 4.4, 4.5, and 4.7 all indicate that the preferred oxide to precipitate and grow is Cr_2O_3, as both chromium and dissolved oxygen are readily available in the filler region. Figure 4.5(c) indicates that growth of existing Al_2O_3 is also possible during service, particularly at 800°C. MnO present in the as-brazed condition is not observed to change appreciably during service conditions.

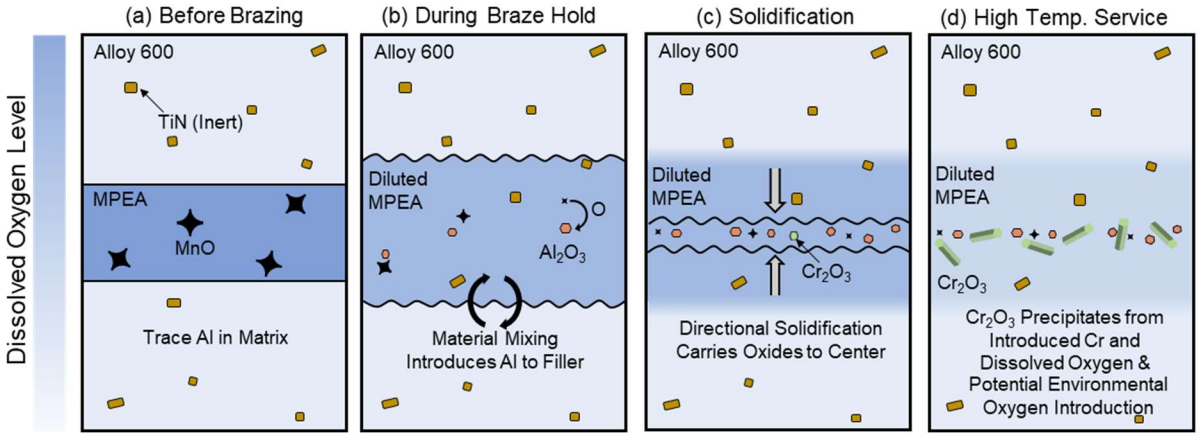

Figure 4.9: Schematic illustration of the behavior of oxygen in the MPEA-Alloy 600 system during brazing and subsequent service.

The effect of oxide particles on the mechanical performance of the MPEA brazes following service conditions has not been isolated in this study. Other microstructural changes, such as chromium carbide precipitation and Mn vaporization along superficial grain boundaries, occur simultaneously during heat treatment. However, Figures 4.6, 4.7, and 4.8 demonstrate that the oxides are an important factor in limiting ductility. In Figure 4.6(a), the best-performing specimen heat-treated at 600°C exhibited nearly twice the total elongation of the worst-performing specimen. A comparison of Figure 4.7(a) and (b) shows a stark difference in the number and size of both Cr_2O_3 and Al_2O_3 on their fracture surfaces, likely resulting from an uneven distribution of oxygen in the original MPEA cast ingots. Figure 4.8(a) and (b) demonstrate the brittle nature of each oxide particle, and the large size of precipitated Cr_2O_3 particles after both 600°C and 800°C heat treatments indicates significant influence on ductility of braze joints.

Overall, despite the oxide precipitation at both 600°C and 800°C conditions, the potential for incomplete fill brazing defects (Fig. 4.7d), and Mn vaporization damage at 800°C (Fig. 4.4a), Figure 4.6(a) shows that all specimens underwent yielding and appreciable plastic deformation prior to failure. This is not the case for Alloy 600 brazes produced using a conventional non-MPEA filler, which contain chromium borides [115]. These findings illustrate that the MPEA's FCC matrix ensures ductile deformation and avoids fully brittle failure in the face of oxide inclusions, brazing defects, and defects acquired during service. Moreover, the constituent phase assessment did not detect any intermetallic phase precipitation during either 600°C or 800°C heat treatment, indicating the short-term thermodynamic stability of the FCC solid solution matrix and the potential for enduring ductility in the braze filler if contamination from manufacturing is better controlled.

4.6 Conclusions

1. For the MPEA-brazed Alloy 600 system, the presence of MnO in as-fabricated MPEA, the poor vacuum capabilities of the MPEA arc-melting setup, and the high MPEA oxygen content estimated through inert gas fusion elemental analysis all point to the MPEA casting process as the primary point of oxygen introduction.
2. A comprehensive analysis by synchrotron XRD and EDS indicates that the MPEA-brazed Alloy 600 structure contains only the variably segregated FCC solid solution matrix phase and carbide, nitride, and oxide phases both before and after simulated service at 600°C or 800°C. No intermetallic phases are detected to form during brazing or simulated service. The carbide and nitride phases are native to Alloy 600, but the oxide phases result from atmospheric contamination of the filler.
3. During brazing, MnO reacts with trace Al from Alloy 600 to form Al_2O_3, which exists in the as-brazed microstructure alongside some Cr_2O_3 and unreacted MnO. During service at both 600°C and 800°C, large Cr_2O_3 particles precipitate from Cr and oxygen dissolved in the matrix.
4. Large Cr_2O_3 particles and Al_2O_3 cluster networks are identified as features detrimental to the ductility of brazes following service. Improvements to performance can be expected with fewer contaminant particles, highlighting the importance of careful atmospheric oxygen control during MPEA production by casting.

4.7 Chapter Acknowledgements

This research is supported by the National Science Foundation with Award No. 1847630. This research used resources of the Advanced Photon Source, a U.S Department of Energy (DOE) Office of Science User Facility operated for the DOE Office of Science by Argonne National Laboratory under Contract No. DE-AC02-06CH11357. Data was collected at Beamline 1-ID-E. Support from beamline staff was greatly appreciated. Use of the Tescan S8252G SEM was supported by the National Science Foundation Division of Materials Research Award No. 1828454.

CHAPTER 5
METHODOLOGY FOR PHASE IDENTIFICATION IN COMPLEX CONCENTRATED ALLOY SYSTEMS

5.1 Abstract

Conventional strategies for phase identification from X-ray diffraction (XRD) do not holistically account for the compositional complexity and stoichiometric deviations from pure phases presented in complex concentrated alloy (CCA) systems. In this work, a robust methodology is presented for the identification of constituent phases in any newly fabricated CCA. This methodology synthesizes predicted phase fraction and phase composition from thermodynamic simulations, existing literature data for crystal structures, and high-energy synchrotron XRD experiments along with supplementary data collected via scanning electron microscopy (SEM) with energy dispersive spectroscopy (EDS). A critical component of the methodology is the introduction of a statistical hard-sphere model, employed on composition data output from simulations, to predict XRD peak positions for compositionally complex disordered solid solution phases common to CCAs. The methodology is demonstrated on a material system consisting of a single-phase MnFeCoNiCu-type CCA, multiphase Ni-base Alloy 738LC, and a range of intermediate compositions generated by laser-welding between the two materials. In this demonstration, a system-specific library of simulated XRD patterns for twelve prospective phases is amassed and compared with experimental synchrotron and supplementary data. The prospective phases include two solid solutions, two carbides, three oxides, and five intermetallic phases. Only six of the twelve prospective phases are determined to be experimentally present in some composition within the system. While this discrepancy may indicate the over-prediction of certain phases by thermodynamic simulations, this demonstration exemplifies rigorous accounting for all statistically significant experimental XRD peaks across a broad range of compositions, even those of low intensity. The methodology is therefore validated for the identification of all constituent phases detectable by synchrotron XRD in a CCA material system with many unknowns. Furthermore, the experimental lattice parameters for the disordered FCC solid solution matrix in the material system demonstrate strong agreement with those predicted by the statistical hard-sphere model, indicating the effectiveness of this calculation in predicting XRD peak positions for disordered solid solutions in CCAs.

5.2 Introduction

Since they were originally conceptualized in 2004 [63, 64], high-entropy alloys (HEAs) have been an area of interest in the metallurgical community as a vast design space from which to select novel structural or functional materials. With the universality of the original entropy-driven postulates of HEAs being called into question in recent studies [78, 86], many researchers in materials design are shifting away from strict, entropy-based definitions and broadening the design space to include multi-principal element alloys (MPEAs) or complex, concentrated alloys (CCAs) [1]. In this broadened design space, concentration limits and restrictions on the number of constituent elements are more relaxed, such that many traditional material systems including Ni-superalloys and even some stainless steels meet criteria for classification as MPEAs or CCAs [1].

When investigating novel materials in the CCA design space, a robust and thorough assessment of their constituent metallurgical phases is essential to predict performance. High energy synchrotron X-ray diffraction (XRD) is the most powerful and efficient technique available for this characterization. In contrast to electron-diffraction techniques, synchrotron XRD can assess relatively large material volumes, and it has been reported to detect minor phases with volume fractions as low as 0.0045 in multiphase systems [121]. Traditionally, phase identification from an XRD pattern is accomplished by comparison with the powder diffraction file (PDF) [122, 123], a comprehensive database of materials' powder diffraction patterns amassed over the past 80 years [124, 125]. In recent decades, several software packages for automated phase identification using methods based on comparison to the PDF database have been developed [125].

Simple comparison to the PDF, especially using automated techniques, is often insufficient for a complete and correct identification of constituent phases in novel, multiphase CCAs. Powder diffraction patterns are defined by peak positions and relative intensities, the latter assuming an effectively infinite number of randomly oriented diffracting grains. However, many novel CCAs, as well as established Ni-superalloy CCAs, are assessed in their as-cast state [1], where large grain size and strong solidification texture cause significant deviations from powder-pattern intensities. Additionally, disordered solid-solution phases common to CCAs often have lattice parameters, and corresponding XRD peak positions, that do not precisely match those of known substances in the PDF. Furthermore, any non-solid-solution phases that exist in CCA systems may differ from their known stoichiometry in isolation, due to the availability of elements in the CCA for substitution. The Rietveld refinement technique [126] can accommodate deviations from powder

intensities and known lattice constants by iteratively refining relevant parameters until the differences between an experimental pattern and that calculated from an input crystal structure are minimized. However, when assessing novel materials, this technique is severely limited in that it requires known prototype structures to be input, creating the potential for incorrect phase identification if false assumptions regarding the constituent phases are made.

Few studies on novel CCAs directly acknowledge the full complexity of phase identification from XRD in these alloy systems. In one of the most comprehensive existing studies, Gasan et al. discuss the necessity of using equilibrium and non-equilibrium thermodynamic simulations to guide the selection of structures input to a Rietveld refinement for the four-phase $Al_xCoCrFeMoNi$ CCA system [127]. This strategy can reduce the possibility of erroneous structure selection. However, in this study, the selected input structures were taken directly from the PDF materials database without considering the effects of composition on crystal lattice parameters. Other studies compare experimental XRD data for a CCA to the predicted constituent phases from thermodynamic simulations [128, 129], but these do not perform Rietveld refinements and do not discuss in detail the strategy for assigning experimental XRD peaks to a particular phase.

To overcome these deficiencies, this paper outlines a thorough and robust methodology to synthesize all the information available from thermodynamic simulations, literature, and experimental data to identify all phases present in a newly fabricated CCA with confidence. The flow chart for this methodology is depicted in Figure 5.1 and discussed in subsequent sections. To demonstrate the applicability of the methodology to a wide range of CCAs, a material system was selected consisting of the single-phase $Mn_{35}Fe_5Co_{20}Ni_{20}Cu_{20}$ MPEA (composition approximate) [2, 68, 80, 115], the multiphase Ni-base Alloy 738LC, and intermediate compositions generated by laser-welding between the two materials. This MnFeCoNiCu-type MPEA has been demonstrated as a successful braze filler for Ni-base Alloy 600 due to the predominance of a single, ductile FCC solid solution phase in both materials [2, 115]. However, the MPEA/Alloy 738LC system is more compositionally and microstructurally complex, as Alloy 738LC contains both refractory elements and precipitate-forming elements which are nominally absent in Alloy 600 [13, 18]. These materials, and particularly the previously un-reported intermediate compositions generated by welding, are therefore ideally suited to demonstrate the phase identification methodology for a multiphase system with many unknowns.

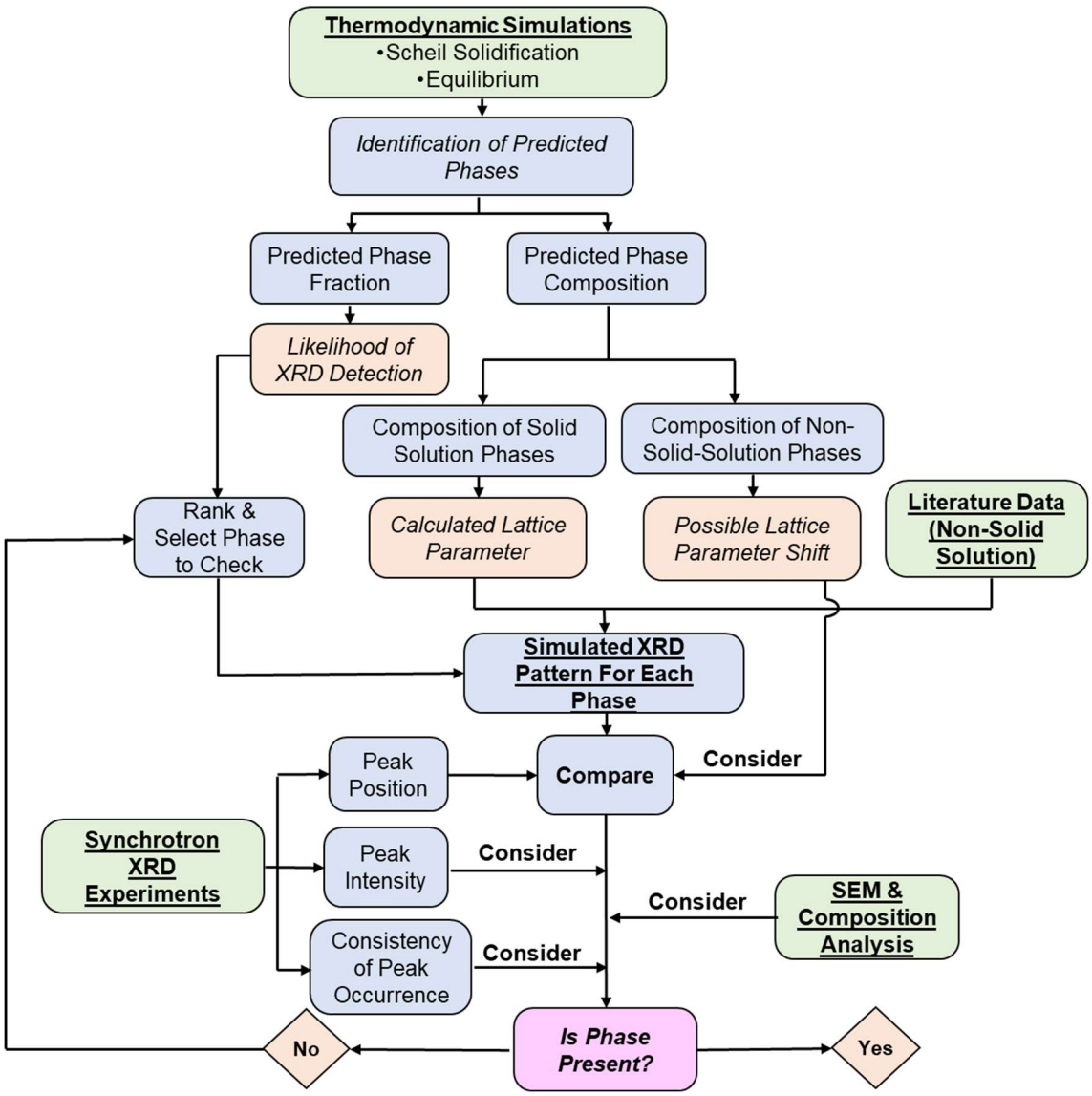

Figure 5.1: Flow-chart describing the methodology combining simulated and experimental data to identify phases present in a complex concentrated alloy of novel composition. Green boxes represent information input to the methodology, blue boxes represent intermediate analytical steps, and orange boxes represent important information output from the preceding steps.

5.3 Simulations

To study the range of intermediate compositions between the MnFeCoNiCu-type MPEA and Alloy 738LC, the dilution parameter is introduced to quantify the extent of mixing between the two materials. Dilution is often reported in welding metallurgy as a means of quantifying the amount of base metal incorporated into the melt pool in a non-autogenous weld [5, 130]. By convention, the base material is treated as the diluent, such that 0% dilution corresponds to pure weld filler material, and 100% dilution corresponds to pure base material. If the two materials are

of disparate concentration *(C)* in a particular element *(i)*, the dilution $(Dil)_i$ in a weld may be calculated by

$$(Dil)_i = \frac{C_{i,Weld} - C_{i,Filler}}{C_{i,Base} - C_{i,Filler}} \quad (5.1)$$

In this work, the MnFeCoNiCu-type MPEA is treated as the filler material, Alloy 738LC is treated as the base, and any intermediate composition is treated as the weld. For simulations, intermediate compositions were calculated in increments of 10% dilution, assuming that $(Dil)_i$ remains constant for every element in the system.

5.3.1 Thermodynamic Simulations

As indicated in Figure 5.1, each calculated composition was first assessed via the Scheil solidification and equilibrium modules in ThermoCalc software. For comparison, both the TCNI-11.0.1 database for Ni-alloys and the TCHEA-5.1 database for high entropy alloys were employed in the simulations. ThermoCalc's database documentation [131] was used to interpret the predicted phases in the results. Figure 5.2 summarizes the simulated phase fractions for all prospective minor phases for both databases and both simulation modules. The major phase, constituting the remainder of the material up to a phase fraction of 1.0, always consisted of a disordered FCC solid solution matrix. Phase fractions are presented at the termination of the solidification sequence for the Scheil simulations, and at a temperature of 843°C for the equilibrium simulations. 843°C was selected because it is the industrially recommended aging temperature for Alloy 738LC [18]. As shown in Figure 5.2, a total of eleven prospective minor phases are predicted to form in at least one of the simulation modules for at least one dilution condition. Nine of these phases can be sub-categorized as disordered solid solutions, carbides, geometrically close-packed (GCP) ordered intermetallics, or topologically close-packed (TCP) ordered intermetallics.

Two BCC solid solutions are predicted. One, labeled BCC in Figure 5.2, is prevalent across many dilution levels in the Scheil module at phase fractions up to 0.01, and at dilution levels less than 50-60% in the equilibrium data at phase fractions up to 0.06. The other, labeled BCC#2, is only predicted in very small phase fractions at high dilution levels in the Scheil module. An MC carbide phase is predicted at every dilution level of 10% or more in the Scheil data, and between dilution levels of 20-90% in the equilibrium data. At the Alloy 738LC composition (100% dilution), the equilibrium carbide at 843°C is instead predicted to be $M_{23}C_6$. The MC carbide phase

fraction increases with dilution level and approaches 0.01 near the Alloy 738LC composition in both simulation modules, while the $M_{23}C_6$ phase fraction exceeds 0.02 in the condition for which it is predicted. In terms of performance, the prediction of carbide phases is benign, as carbides are found in most Ni-base superalloys and offer direct and indirect strengthening contributions [10].

The GCP phases include γ' and η, which are also generally neutral to beneficial microstructural constituents [10]. γ' is the main strengthening phase for Alloy 738LC and a range of precipitate-strengthened Ni-superalloys, and is critical in providing high-temperature strength [132]. η-phase, though typically not employed as a strengthening phase at service conditions, may assist in microstructural control during processing of certain superalloys [10]. Figure 5.2 shows that γ' is only predicted in equilibrium conditions, first appearing at a dilution level of 50% and steadily increasing in abundance as dilution increases, reaching a phase fraction exceeding 0.45 in the Alloy 738LC composition. The η-phase only appears at dilution levels of 90-100% in the non-equilibrium Scheil simulations. However, it is predicted to be the most abundant minor phase in these conditions, with a phase fraction exceeding 0.05 for 100% dilution in the HEA database prediction.

The brittle TCP phases, which include σ, μ, and Laves phase, are always detrimental to performance [10, 133, 134]. Figure 5.2 indicates that these phases are only predicted in the as-solidified microstructure (Scheil simulation) and not in equilibrium conditions. σ and μ are predicted by both databases when dilution exceeds 70%, and Laves phase is predicted primarily by the Ni database when dilution is between 10% and 50%. The two additional phases predicted are δ and the Heusler phase. δ is commonly observed in certain superalloys and is often considered detrimental, as it causes depletion of strengthening precipitates, although some beneficial aspects are also noted [135]. The Heusler phase is occasionally discussed in both MPEA and Ni-alloy literature and reported to be brittle [136, 137]. Figure 5.2 illustrates that δ and the Heusler phase, as well as the BCC#2 solid solution, only appear intermittently and at very small predicted phase fractions in the simulation data. These three phases were disregarded in subsequent analysis.

Broadly, the simulated results from each of the two databases were similar, although comparing Figure 5.2(a) and (b) shows that the HEA database consistently predicts higher phase fractions of minor phases across the compositions assessed by the Scheil module. The results from the HEA database were therefore considered a more conservative prediction of minor phases that would need consideration in experimental data, and this database was used in subsequent analysis.

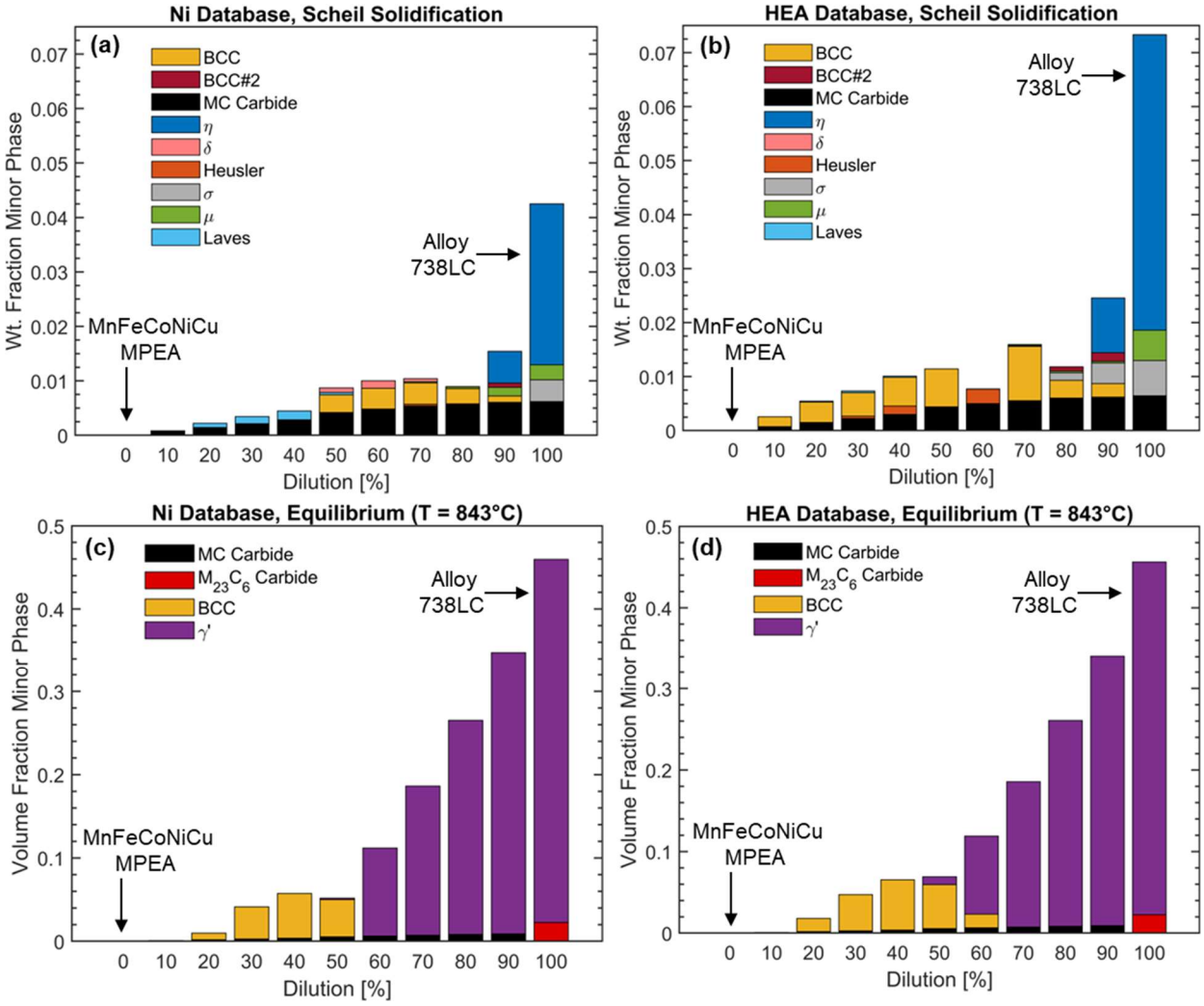

Figure 5.2: Summary of phase fractions predicted by thermodynamic simulations for all phases except the disordered FCC solid solution matrix, which comprises the balance. (a, b) Scheil solidification module, weight fraction. (c, d) Equilibrium module at a temperature of 843°C, volume fraction. (a, c) Using TCNI-11.0.1 database. (b, d) Using TCHEA-5.1 database.

As indicated in Figure 5.1, the simulated phase composition is another important output of the thermodynamic simulations. The composition data output from the HEA database for select prospective minor phases is provided in Figure 5.3, with any elements whose concentration is below 1 at. % omitted. The phases shown are those predicted to exist at appreciable phase fractions across a broad range of dilution levels. Composition data from equilibrium simulations is reported at 843°C. Composition data from Scheil simulations is averaged step-wise over the precipitation of the phase in the simulated solidification sequence, according to the equation:

$$C_{i,\phi} = \frac{1}{f_{\phi,N}} \sum_{j=1}^{N-1} \left(f_{\phi,(j+1)} - f_{\phi,j} \right) * \ C_{i,j} \tag{5.2}$$

Where C is the concentration of any element i in phase ϕ, N represents the total number of simulation steps taken in the Scheil solidification sequence, j represents any given simulation step number, and f represents the fraction of phase ϕ at a given simulation step.

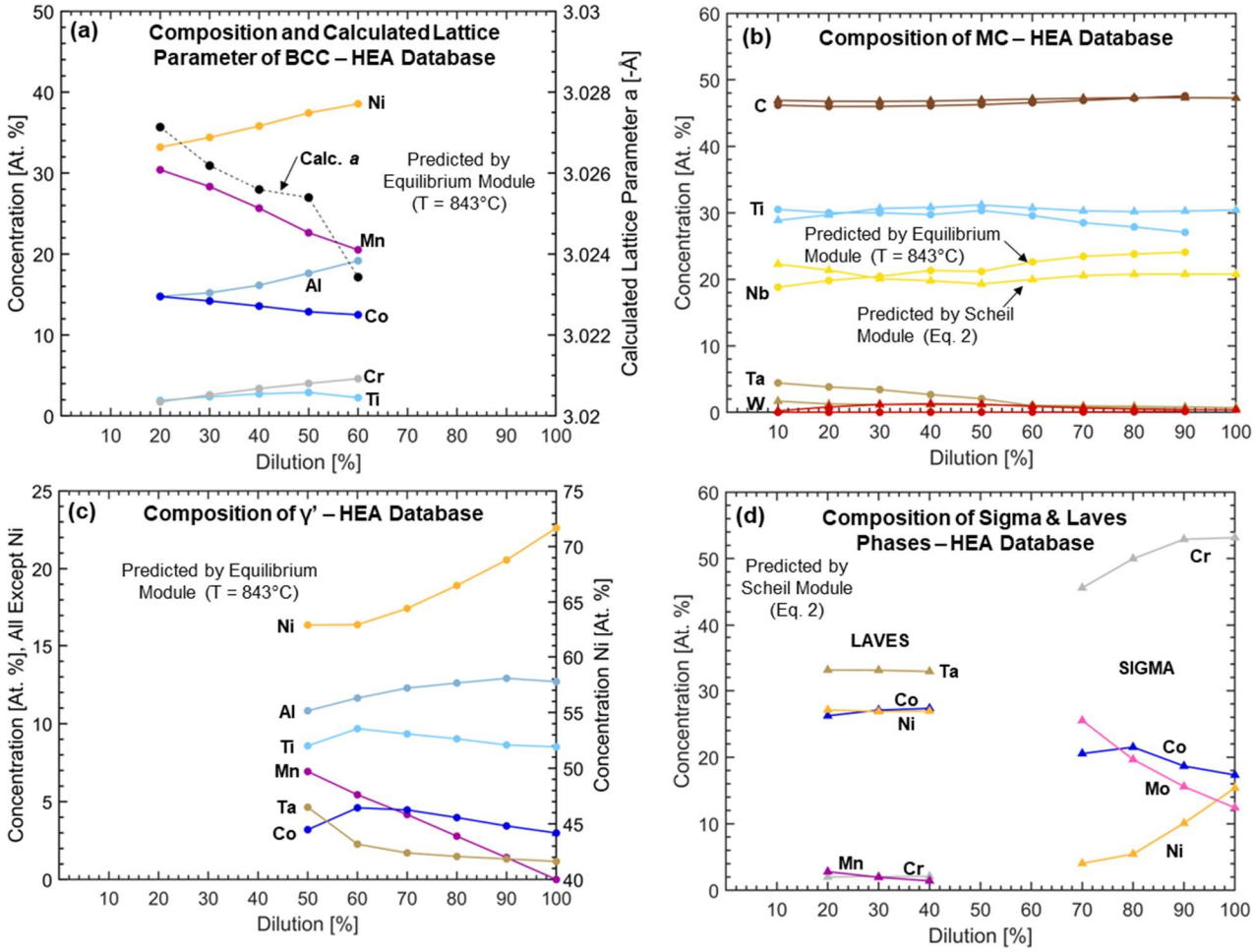

Figure 5.3: Simulated composition data for select prospective phases in the MPEA/Alloy 738LC system. Circles represent data from the equilibrium module, and triangles represent data from the Scheil solidification module. (a) BCC solid solution with the lattice parameter *a* calculated via Equation 5.4 included. (b) MC carbide. (c) γ'. (d) Sigma and Laves TCP phases.

Figure 5.3(a) shows that the prospective BCC phase contains Ni, Mn, Al, Co, Cr, and Ti. For simplicity, only the equilibrium composition data are shown, but the Scheil module predicts similar trends in composition. Figure 5.3(b) indicates that Ti and Nb are the main metal atoms in

the MC carbide phase, with minor concentrations of Ta and W. In Figure 5.3(c), the composition of γ' is consistent with its known stoichiometry of $Ni_3(Ti, Al)$, although γ' is predicted to dissolve increasing amounts of Mn, Co, and Ta as the dilution level decreases, i.e., as MnFeCoNiCu MPEA is mixed with Alloy 738LC. Finally, Figure 5.3(d) shows that σ is predicted to be rich in Cr, Co, Mo and Ni, while the constituents of the Laves phase are Ta, Co, Ni, Mn, and Cr.

As introduced in [80], a statistical hard-sphere approximation can be used in conjunction with reported atomic radii data [1] to calculate the lattice parameter of a disordered solid solution for any composition. The following equations are used for an FCC and a BCC structure, respectively:

$$a_{FCC} = \left(\frac{1}{\sqrt{2}}\right) \sum_{k=1}^{n^3} (C_{Ak} * C_{Bk} * C_{Ck}) * (r_{Ak} + 2r_{Bk} + r_{Ck}) \tag{5.3}$$

$$a_{BCC} = \left(\frac{1}{\sqrt{3}}\right) \sum_{k=1}^{n^3} (C_{Ak} * C_{Bk} * C_{Ck}) * (r_{Ak} + 2r_{Bk} + r_{Ck}) \tag{5.4}$$

Where a is the lattice parameter, n is the number of elements in the system, k is a unique permutation of three elements A, B, and C in the system, which may include repeats, C is the concentration of an element in atomic fraction, and r is the reported atomic radius of an element. The calculated lattice parameter for the simulated compositions of the prospective BCC phase is included in Figure 5.3(a). As indicated in Figure 5.1, this model for estimating the lattice parameter of a solid solution of undocumented composition is critical for assessing the presence of such a phase in XRD experiments.

5.3.2 Simulated X-Ray Diffraction Patterns for Prospective Phases

The composition information output from the thermodynamic simulations, such as that displayed in Figure 5.3, was used to inform the input crystal structure used to simulate an XRD pattern for each prospective phase. The strategy for selecting the input crystal structure differed for solid-solution and non-solid-solution phases as shown in Figure 5.1 and described in the following sections. Once an input structure was selected, all pattern simulations were performed using GSAS-II software [117] with powder-pattern assumptions. The 2θ coordinate was converted to the wavelength-independent reciprocal lattice vector q, where $q = 2\pi/d$, with d representing the

atomic interplanar spacing. Figure 5.4 summarizes the input crystal structures and resultant simulated patterns.

5.3.2.1 Solid-Solution Phases

As indicated in Figure 5.1, because the compositions of the solid solution prospective phases are undocumented in the literature, the lattice parameter calculated via the simulated composition data and Equations 5.3-5.4 was essential to simulate their XRD patterns. Every composition across the range of dilution conditions has a unique calculated lattice parameter, as demonstrated in Figure 5.3(a), and the peak positions for each composition vary correspondingly. Figure 5.4(a) and (b) show renderings of example compositions of the FCC (matrix) and BCC prospective phases and the accompanying simulated patterns. Two unit cells in each dimension are illustrated in the renderings, to demonstrate the disordered nature of the phases, but a single unit cell with lattice parameter calculated via Equations 5.3 and 5.4 was used to simulate the patterns.

5.3.2.2 Non-Solid-Solution Phases

As shown in Figure 5.1, existing literature data, summarized in Table 5.1, was primarily used to construct input structures for non-solid-solution phases. Despite the variations in composition shown in Figure 5.3 (b-d), crystal lattice parameters were fixed at reported literature values. For the γ' phase (Fig. 5.4c), the cubic ordered $L1_2$ Ni_3Al structure [119] was input, with the lattice parameter *a* adjusted to the reported value of 3.58857 Å in Alloy 738LC [138]. For the η phase (Fig. 5.4d), the hexagonal close-packed ordered $D0_{24}$ Ni_3Ti structure [139] was input, and lattice parameters were not adjusted from the reported values. It has been reported that η has very low solubility for elements other than Ni and Ti [10], so any substitutional uptake of extrinsic elements affecting the lattice parameters would be minimal. Based on the simulated composition of the MC carbide in Figure 5.3(b), the TiC structure [119] was input for this phase, with the consideration that some deviation from the simulated peak positions (Fig. 5.4e) would be possible in experiments due to substitution of Nb, Ta, and W for Ti. Under similar logic, $Cr_{23}C_6$ [119] was selected as the representative structure for the $M_{23}C_6$ phase (Fig. 5.4f).

Table 5.1: Summary of input parameters for simulated XRD patterns for each prospective phase

Phase	Input Structure Formula	Space Group	Lattice Parameter(s)	References
FCC Matrix	Variable	$Fm\bar{3}m$ (#221)	Calculated	-
BCC	Variable	$Im\bar{3}m$ (#229)	Calculated	-
γ'	Ni_3Al	$Pm\bar{3}m$ (#225)	a = 3.589 Å	[119, 138]
η	Ni_3Ti	$P6_3/mmc$ (#194)	$a = b$ = 5.096 Å c = 8.304 Å	[10, 139]
MC	TiC	$Fm\bar{3}m$ (#225)	a = 4.336 Å	[119]
$M_{23}C_6$	$Cr_{23}C_6$	$Fm\bar{3}m$ (#225)	a = 10.552 Å	[119]
σ	$Cr_{53}Co_{47}$	$P4_2/mnm$ (#136)	$a = b$ = 8.78 Å c = 4.54 Å	[134, 140]
μ	Ta_6Co_7	$R\bar{3}m$ (#166)	$a = b$ = 4.755 Å c = 2.583 Å	[133, 134]
Laves	$TaNi_2$	$P6_3/mmc$ (#194)	$a = b$ = 4.85 Å c = 7.93 Å	[133, 134]

For the three TCP phases, simulated composition data informed structure selection. Hall and Algie summarize the common, known binary σ-phase compositions and their ordering schemes [140]. Based on the simulation output in Figure 5.3(d), the prospective σ-phase most closely resembles $Cr_{53}Co_{47}$, with significant substitution of Co by Ni and Mo. The input structure for σ (Fig. 5.4g) was therefore constructed based on the ordering scheme for $Cr_{53}Co_{47}$ [140], with lattice parameters taken from Wilson [134]. The μ-phase has stoichiometry A_6B_7 with the ordering scheme given by Sinha [133] and lattice parameters given by Wilson [134]. Simulated composition data provide a stoichiometry consistent with Ta, W, Nb, Mo, and Fe occupying "A" sites, and Co, Ni, and Cr occupying "B" sites in the prospective simulated μ-phase. To simplify the input structure (Fig. 5.4h), the stoichiometry was approximated as Ta_6Co_7. For the Laves phase, the predicted superlattice structure in ThermoCalc was C14, which corresponds to the $MgZn_2$ prototype with ordering scheme as described by Sinha [133]. Typical lattice parameters in a Ni-alloy environment are provided by Wilson [134]. The stoichiometry of the Laves phase is AB_2, and simulated composition data in Figure 5.3(d) is consistent with Ta occupying "A" sites and Ni and Co occupying "B" sites along with minor concentrations of Mn and Cr. For the input structure (Fig 5.4i), the stoichiometry was simplified to $TaNi_2$.

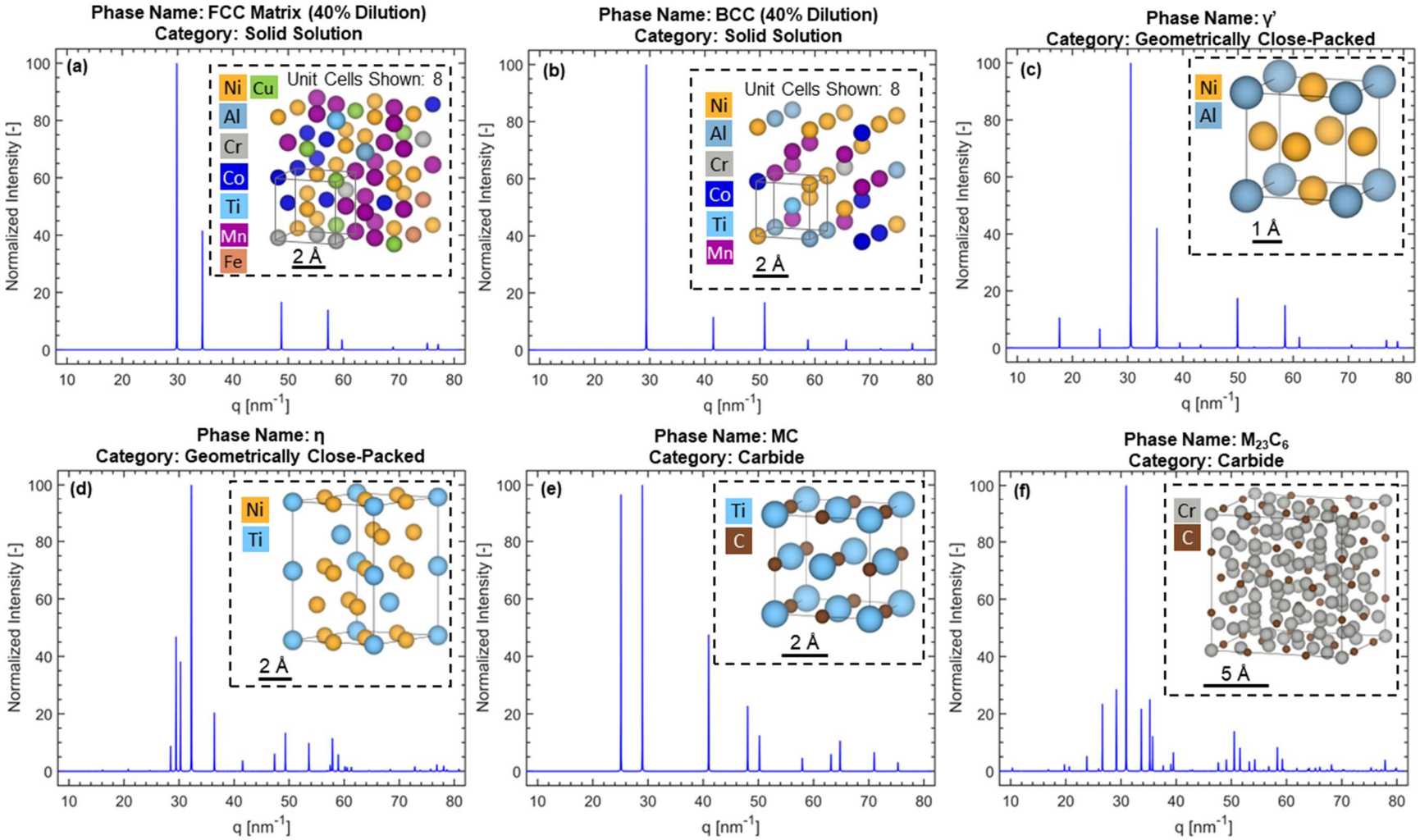

Figure 5.4: Summary of crystal structures and simulated XRD patterns for (a-i) prospective phases output from the thermodynamic simulations, and (j-l) prospective oxide phases in the system (continued on next page). (a) FCC matrix. (b) BCC solid solution phase. (c) γ'. (d) η. (e) MC carbide. (f) $M_{23}C_6$ carbide.

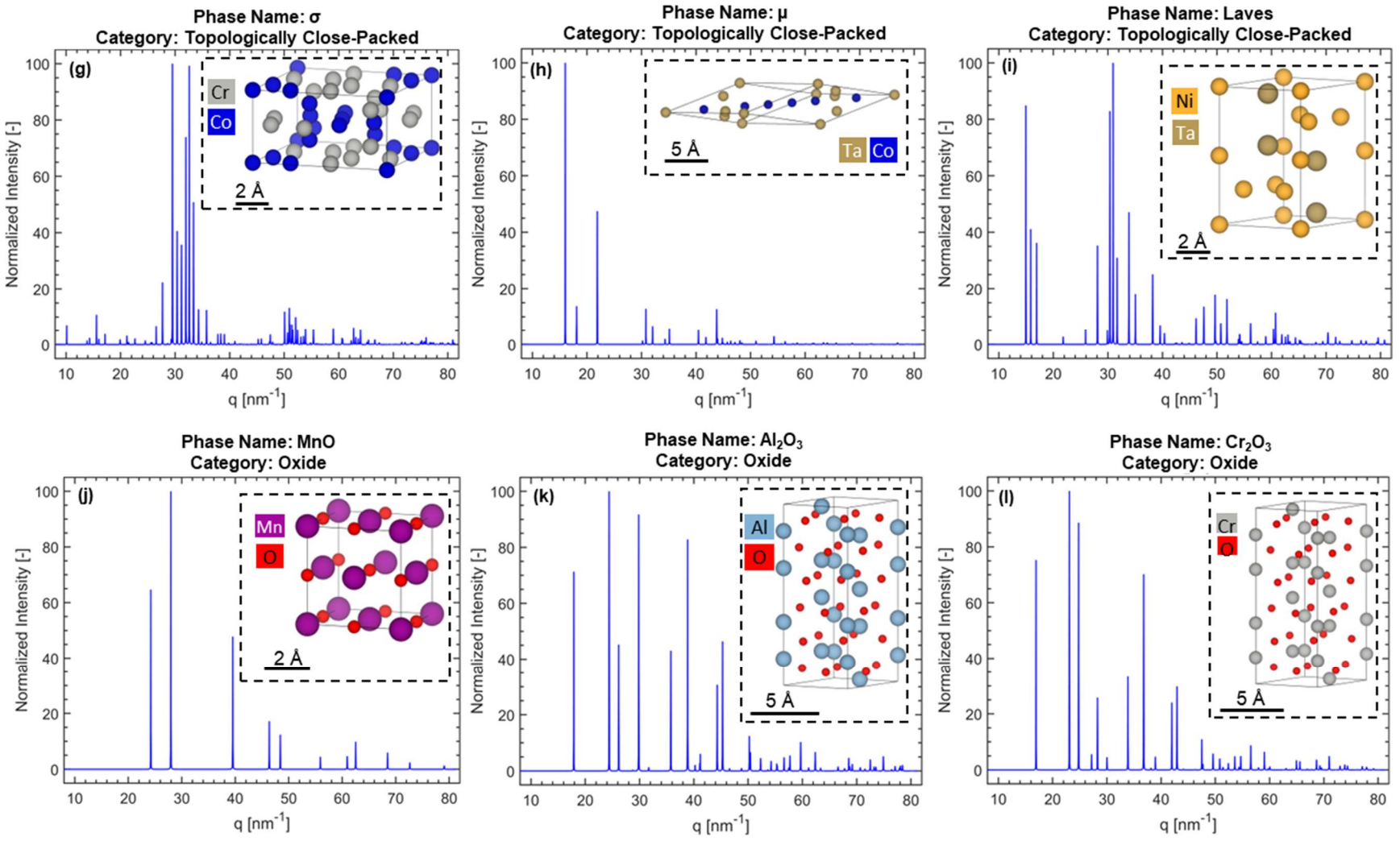

Figure 5.4 (continued): Summary of crystal structures and simulated XRD patterns for (a-i) prospective phases output from the thermodynamic simulations, and (j-l) prospective oxide phases in the system (continued from previous page). (g) σ. (h) μ. (i) Laves. (j) MnO. (k) Al_2O_3. (l) Cr_2O_3.

5.3.2.3 Oxides

Although oxygen was not included in the thermodynamic simulations to avoid a confounding variable in the prediction of prospective phases, the cast MnFeCoNiCu-type MPEA was found to have sufficient oxygen content that consideration of prospective oxide phases in the material system was required, based on the findings in Chapter 4. Figure 5.4(j-l) illustrate graphical renderings and simulated XRD patterns for three oxides likely to form in the material system – cubic MnO, hexagonal Al_2O_3, and hexagonal Cr_2O_3. Input structures for each of these phases were taken from [119] with the lattice parameters unaltered. In subsequent analysis, the simulated peak positions for the twelve prospective phases summarized in Figure 5.4 served as a library specific to the MPEA/Alloy 738LC material system for the purpose of comparison with experimental data.

5.4 Experimental Procedures

To experimentally validate the thermodynamic predictions of the constituent phases that form in the MnFeCoNiCu-type MPEA/Alloy 738LC material system, a laser-welding setup was employed to mix the two materials to varying degrees and thus achieve variable levels of dilution according to Equation 5.1. After the resultant, mixed composition re-solidified, site-specific XRD was performed using a synchrotron X-ray beam, and the compositions were characterized further by scanning electron microscopy (SEM) and energy-dispersive spectroscopy (EDS). Essential aspects of the laser-mixing/synchrotron XRD experiment are illustrated schematically in Figure 5.5 and described in the following sections.

5.4.1 Material Preparation

The MPEA of approximate composition $Mn_{35}Fe_5Co_{20}Ni_{20}Cu_{20}$ was cast via button arc-melting from pieces of its pure constituent elements as described in [2]. Cast buttons were subsequently machined by milling to remove all visible surface oxide, although the oxygen content of the bulk filler remained above 1000 ppm (Chapter 4), necessitating the consideration of oxide phases discussed in Section 5.3.2.3. Alloy 738LC was received in its as-cast state from an external supplier.

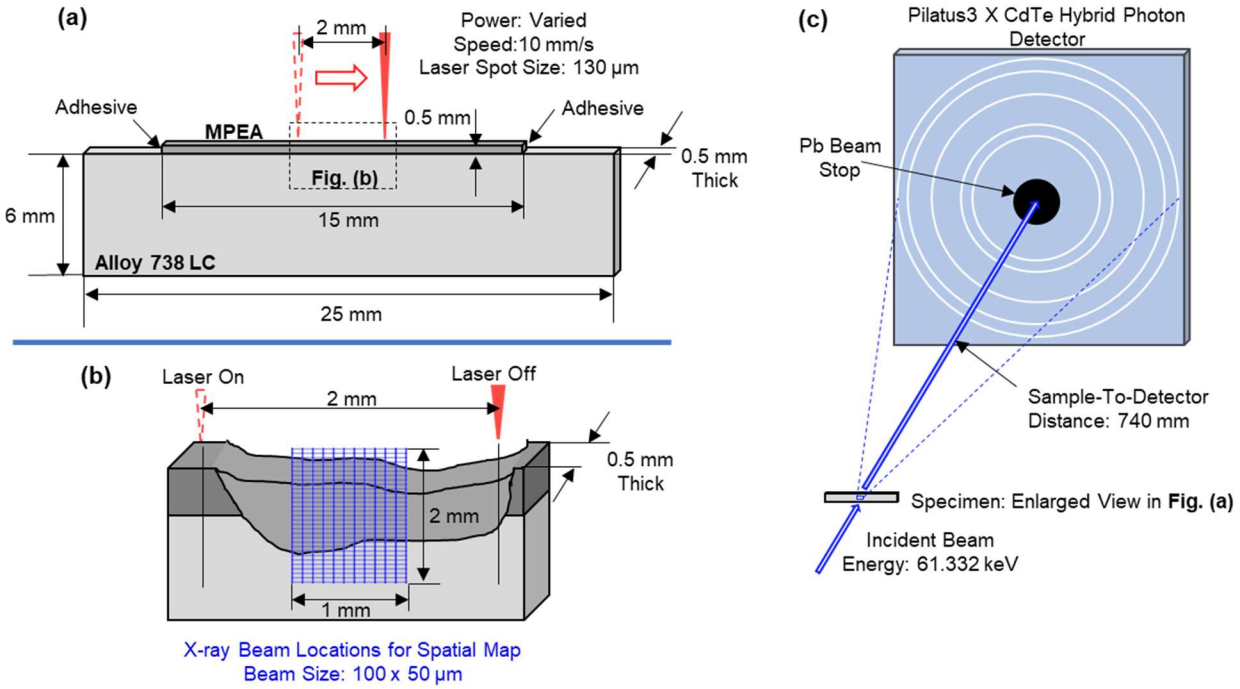

Figure 5.5: Schematic illustrations of the experiment setup for synchrotron XRD to assess the constituent phases across a range of CCA compositions. (a) Thin-walled specimen geometry including Alloy 738LC substrate and a strip of MnFeCoNiCu-type MPEA on top. (b) Close-up view of specimen after mixing the two alloys by laser welding and the corresponding incident X-ray beam locations for spatial mapping of diffraction patterns. (c) Macroscopic view of the far-field diffraction detection setup.

Both materials were subjected to a recrystallization treatment to reduce the grain size compared to the as-cast condition, to increase the diffracting grain population and allow for easier observation of XRD peaks caused by minor constituent phases. Epitaxial growth from the Alloy 738LC substrate in the solidifying pool made it particularly important to reduce the grain size in the substrate to achieve a sufficient diffracting grain population in the melt pool. The recrystallization treatment for the Alloy 738LC involved solutionizing at 1180°C for 24h, followed by cold-rolling to 10% reduction in thickness, and recrystallizing at 1180°C for 15 min. The recrystallization temperature was selected to be above the predicted γ' solvus temperature. The cast MnFeCoNiCu MPEA was rolled at 400°C to 50% reduction in thickness, and subsequently recrystallized at 850°C for 2h. These thermomechanical processing routes reduced the grain size from greater than 5 mm to 100 - 200 µm for Alloy 738LC, and from greater than 100 µm to 10 – 40 µm for the MPEA.

Following the recrystallization treatments, each material was cut to the dimensions depicted in Figure 5.5(a) using a slow-speed saw to accurately limit the specimen thickness to 0.5 mm. Limiting this dimension to 0.5 mm allowed the laser to melt the entire thickness, such that site-specific XRD data could be collected solely from fully melted material. After cutting, the Alloy 738LC pieces were heat-treated at 843°C for 24h to re-introduce γ' into the material, as recommended by [18]. Specimens were then assembled as shown in Figure 5.5(a), using adhesive to affix a strip of MPEA atop the thin edge of the Alloy 738LC substrate piece.

5.4.2 Synchrotron XRD Laser Mixing Experiments

Both laser-melting and synchrotron XRD data collection were performed at Beamline 1-ID-E of the Advanced Photon Source. Laser-melting with an IPG YLR-500-AC-Y11 ytterbium fiber laser was carried out in an argon environment using a 2mm linear scan to melt the two materials together, as shown in Figure 5.5(a-b). The travel speed was constant at 10 mm/s for all experiments, but the laser power was varied from 160W to 220W to achieve varying degrees of material mixing. A laser was also used to melt solely the Alloy 738LC, with no MPEA mixed in, for comparison. The constituent phases and solidification behavior of the MPEA alone were characterized in previous work [80].

After laser melting, site-specific XRD patterns were collected from the melt pool and adjacent substrate material, as shown in Figure 5.5(b-c). More details pertaining to how the samples were aligned and how the location of the fully melted material was determined can be found in Appendix A. For comparison, patterns were also collected from un-melted MPEA and Alloy 738LC materials prior to laser melting. For pattern collection, a monochromatic beam with energy of 61.332 keV was directed in transmission through the samples, with incident beam dimensions of 100 μm horizontally by 50 μm vertically. A Pilatus3 X CdTe 2M hybrid photon counting detector with a sample-to-detector distance of 740 mm was used to collect patterns. The laser welds were translated horizontally and vertically in increments equal to the dimensions of the incident beam, creating a continuous spatial map of XRD patterns that extended 1 mm laterally and 2 mm below the original top surface of the specimen, as detailed in Figure 5.5(b). Patterns were integrated using fit2D software and averaged over each row indicated in Figure 5.5(b) to eliminate any noise contained in singular patterns. Detectable peaks of any intensity were fit with a Pearson VII function [116], whose center was taken as the peak position and height was taken

as the peak intensity. Pearson VII was selected over the conventional pseudo-Voigt function [141] because it proved more robust at programmatically fitting low-intensity peaks, and accuracy of peak shape was not an important consideration in this analysis.

5.4.3 Scanning Electron Microscopy Characterization

Following the laser-mixing experiments and characterization by synchrotron XRD, samples were prepared for microscopy by standard metallographic polishing with a final step of 0.05 μm colloidal silica on a vibratory polisher. No additional chemical etching was performed following vibratory polishing, as the colloidal silica polish offered sufficient imaging contrast in scanning electron micrographs. Subsequently, electron microscopy and EDS characterizations were performed using a Tescan S8252G SEM. Imaging was performed using an accelerating voltage of either 2kV or 5kV, and a beam current of either 100 pA or 300 pA. EDS was performed using an accelerating voltage of 20 kV and a beam current of 10 nA. Low-magnification EDS line-scans were performed across the weld pool/base material interface to assess the bulk composition of the melt pool and calculate the dilution achieved in each laser-mixed sample via Equation 5.1. Higher magnification EDS maps were collected to identify the composition of particles in the microstructure and corroborate the identification of prospective phases made by analysis of the synchrotron XRD data. EDS data was quantified using the ZAF correction method. If particles were too small to be assessed by EDS-mapping, SEM images were used to corroborate the phase identification.

5.5 Results and Discussion

5.5.1 Determining Dilution Level

For the sake of comparing to the simulated data in Figure 5.2, the dilution level achieved in each laser-mixing experiment was determined by assessing the bulk composition of each melt pool. Figure 5.6 shows an example of composition data from an EDS line scan taken across the interface between the melt pool and the un-melted Alloy 738LC for the weld performed using a power of 180 W. The bulk composition of each melt pool was fairly homogeneous, although dendritic/interdendritic segregation [80] resulted in local fluctuations in the concentration of Cr, Mn, Fe, Co, and Cu, as indicated in Figure 5.6. Ni, which displays little tendency for segregation

in the system [80], consistently demonstrated the greatest homogeneity in concentration throughout each melt pool. For this reason, Ni was selected as the basis element for calculating the dilution level via Equation 5.1, and subsequent values of dilution are reported as $(Dil)_{Ni}$. Measured $(Dil)_{Ni}$ levels ranged from 8.1% at a laser power of 160W to 55.3% at a laser power of 220W, while the specimen where Alloy 738LC was melted alone without mixing any MnFeCoNiCu-type MPEA represented a $(Dil)_{Ni}$ value of 100%.

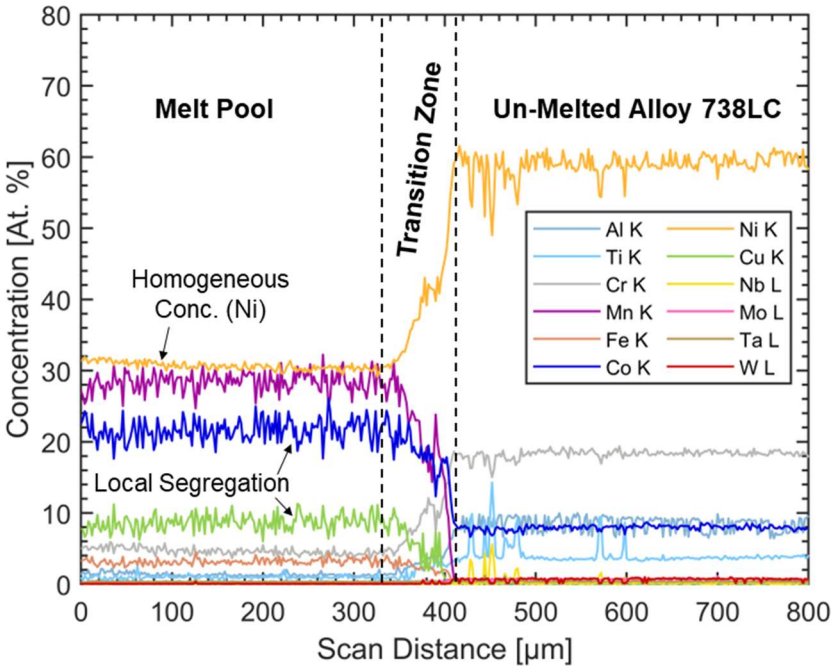

Figure 5.6: Example of composition data collected via an EDS line scan to determine $(Dil)_{Ni}$ level; laser power 180 W.

5.5.2 Phase Identification Methodology

Figure 5.7 shows representative synchrotron XRD patterns from the two, separate un-melted (UM) materials, and from fully-melted (FM) samples spanning the full range of $(Dil)_{Ni}$ values achieved experimentally. As clearly indicated in the patterns, the peaks corresponding to the major, disordered FCC solid solution phase were easily identifiable due to their high relative intensity and positions approximately matching the simulated data in Figure 5.4(a).

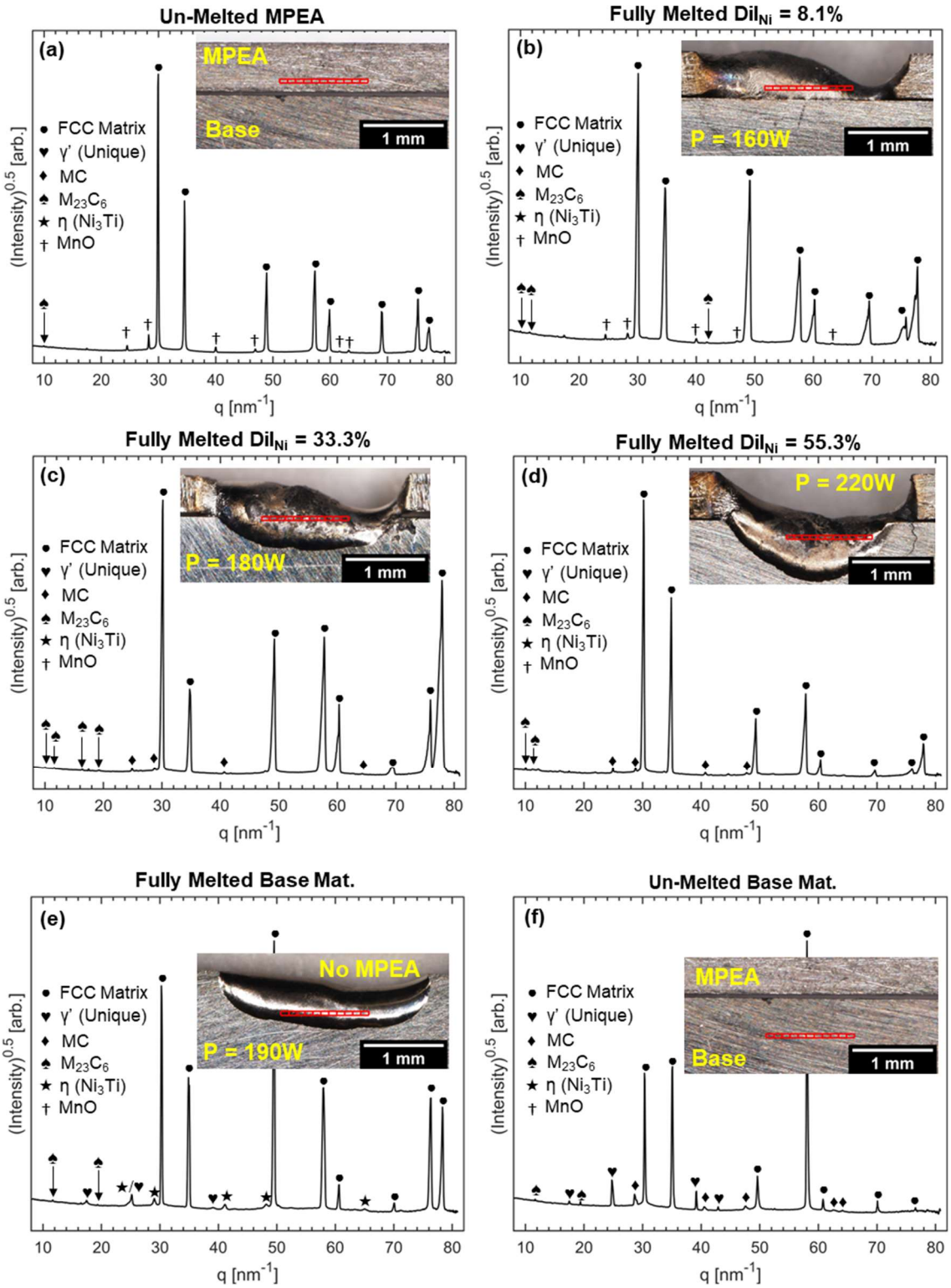

Figure 5.7: Representative XRD patterns averaged over the locations indicated by the red rectangles in the inset macroscopic images. (a) Un-melted MnFeCoNiCu MPEA. (b-d) Fully melted zones of laser welds with a measured $(Dil)_{Ni}$ of (b) 8.1%, (c) 33.3%, (d) 55.3%. (e) Fully melted Alloy 738 LC alone ($(Dil)_{Ni}$ = 100%). (f) Un-melted Alloy 738LC.

As shown in Figure 5.1, the remainder of the complete set of experimental XRD peaks was systematically assigned to minor constituent phases via an iterative process. First, the likelihood of a given phase being present and detectable by XRD at the experimentally measured dilution/melting condition was assessed based on the simulated phase fraction data in Figure 5.2. For FM material, the constituent phases were expected to match Scheil data more closely, although it was necessary to consider evolution toward equilibrium that occurred as the material cooled. For the individual UM materials, it was expected that the material would closely match equilibrium conditions at 843°C, as the final steps of the preparation routes described in Section 5.4.1 were heat treatments at 850°C for the MPEA and 843°C for Alloy 738LC. If a phase was determined from Figure 5.2 to be probable, the fitted experimental peak positions were directly compared to the simulated peak positions for that phase in Figure 5.4. Because of solidification texture and large grain size, peak position was the most critical attribute in assigning experimental peaks to a constituent phase. However, other attributes such as peak intensity and consistency of occurrence among patterns taken from a given melt pool, along with potential lattice parameter shift due to element substitution based on composition data in Figure 5.3, were also considered. If multiple diffraction peaks matching simulated data for a given phase were consistently presented for a given experimental condition, the phase was determined to be present and the corresponding peaks assigned. If not, the phase was determined to be absent and the next-most-probable phase assessed. Using this strategy, 96.7% of fitted peaks with an absolute intensity greater than 0.01 and 99.0% of those with an absolute intensity greater than 0.1 were assigned to a phase. For comparison, the absolute intensity values of major-phase peaks usually fell between 10 and 100.

To illustrate how the consistency of peak occurrence was incorporated in the phase identification methodology, Figure 5.8 shows a binned peak-frequency diagram for selected regions of the XRD spectrum. The color bar represents the number out of ten assessed patterns for a given dilution/melting condition in which a peak was positioned within a bin of size 0.025 nm^{-1} in q space. Peaks with an absolute intensity of less than 0.001 are excluded. Note that the color bar in Figure 5.8 does not reflect the value of peak intensity, but relative intensities of peaks corresponding to each phase can be gleaned from the representative patterns in Figure 5.7.

Figure 5.8(a), showing q = 9 – 14 nm^{-1}, clearly indicates the presence of (111) and (200) $M_{23}C_6$ peaks spanning the full range of experimental $(Dil)_{Ni}$ values, even though the intensity of these peaks is so low that they are almost indiscernible in Figure 5.7. Figure 5.8(a) highlights the

utility of the peak-frequency diagram in delineating consistently occurring low-intensity peaks from other, randomly occurring low-intensity peaks that are likely experimental artifacts, i.e., the unlabeled stray lines in the figure. Additionally, Figure 5.8(b) and (c) more clearly show discrepancies between nearly overlapping peaks than Figure 5.7 does. Examples include the (200) peak for both MnO and MC carbide and the (201) η-phase peak, all three of which lie between q = 28.3 – 29.1 nm^{-1} in Figure 5.8(b). Figure 5.8(b) also illustrates that for FM material in which the MPEA and Alloy 738LC were mixed to any extent, each major-phase FCC peak was usually best fit using two separate Pearson VII functions to accommodate peak asymmetry. This asymmetry is most visible in high-index major-phase peaks such as those in the right-hand portion of Figure 5.7(b), and it is caused by dendritic/interdendritic segregation of compositions with disparate lattice parameters, described in detail in [80]. The interdendritic segregation corresponds to a lower-intensity shoulder peak that appears on the left-hand side of the main peak; the corresponding fitted peak centers are labeled in the frequency diagram in Figure 5.8(b).

Imaging and EDS data collected via SEM also served to corroborate the XRD peak analysis and validate the phase identification methodology. Figure 5.9 shows a representative image of the experimentally presented phases in selected specimens, and Figure 5.10 shows corresponding EDS mapping data. Figures 5.9(a) and 5.10(a) confirm the presence of MnO particles exceeding 10 μm in length when $(Dil)_{Ni}$ = 8.1%. Figures 5.9(b) and 5.10(b) demonstrate the presence of Ti-rich particles on the order of 1 μm in diameter when $(Dil)_{Ni}$ = 55.3%, which the composition data in Figure 5.3(b) indicate correspond to the MC carbide phase identified in Figure 5.7(d). The features present in Figure 5.9(c), showing FM Alloy 738LC, are too small to map with EDS in an SEM. However, the features labeled as η-phase in Figure 5.9(c) lie along the Ti-rich segregation identified in Figure 5.10(c), which is consistent with the Ni_3Ti η-phase stoichiometry. The XRD data in Figures 5.7 and 5.8 indicate some γ' precipitation in this FM Alloy 738LC, and very fine precipitates are identified in regions away from the η-phase in Figure 5.9(c). Finally, Figures 5.9(d) and 5.10(d) offer a clear picture of both large, intragranular, Ti-rich MC carbides in UM Alloy 738LC, as well as networks of smaller Cr-rich $M_{23}C_6$ carbides along grain boundaries. The γ' precipitates contained in the FCC (γ) matrix in UM Alloy 738LC are also clearly visible in Figure 5.9(d).

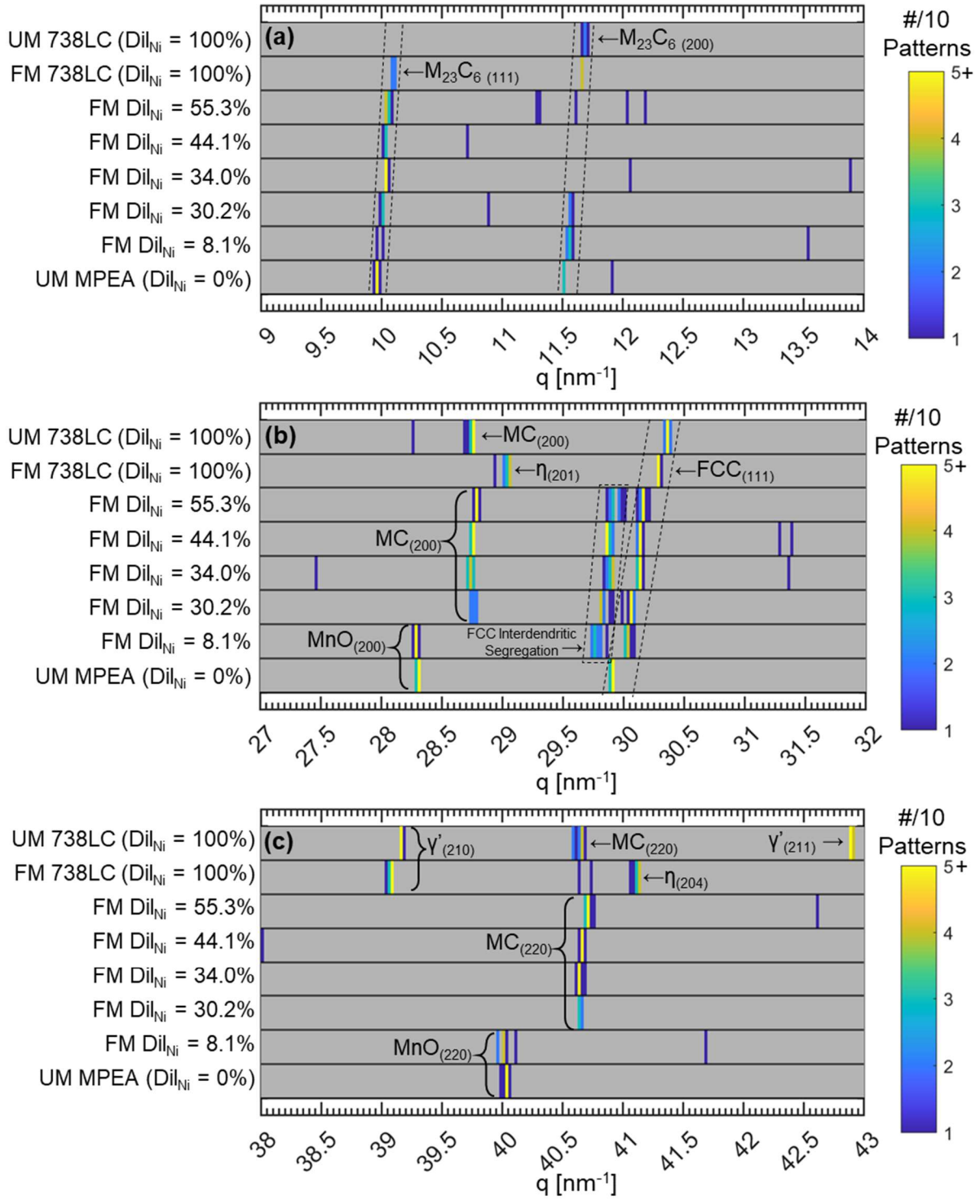

Figure 5.8: Statistical peak-frequency diagrams for select regions of the XRD spectrum displaying the number out of ten patterns for which a peak of absolute intensity greater than 0.001 was centered within a bin of 0.025 nm^{-1} in q-space. (a) q = 9 – 14 nm^{-1}. (b) q = 27 – 32 nm^{-1}. (c) q = 38 – 43 nm^{-1}.

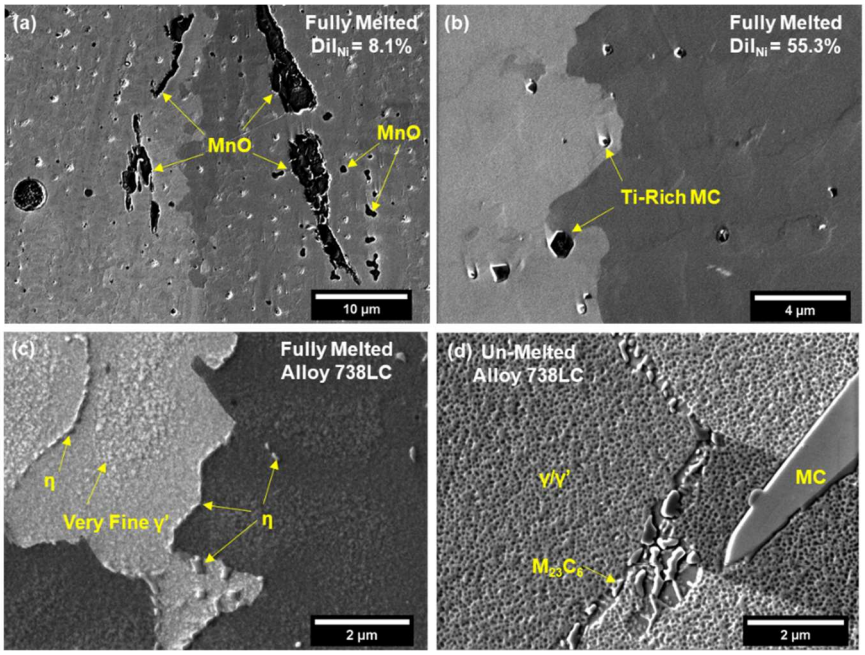

Figure 5.9: Secondary electron images of each phase detected in the synchrotron XRD data, in selected specimens. (a) MnO in the FM $(Dil)_{Ni}$ = 8.1% condition. (b) MC carbides in the FM $(Dil)_{Ni}$ = 55.3% condition. (c) η and fine γ' in the FM Alloy 738LC base material. (d) Intragranular MC carbide and grain-boundary $M_{23}C_6$ carbides in the precipitate-hardened γ/γ' matrix of the UM Alloy 738LC base material.

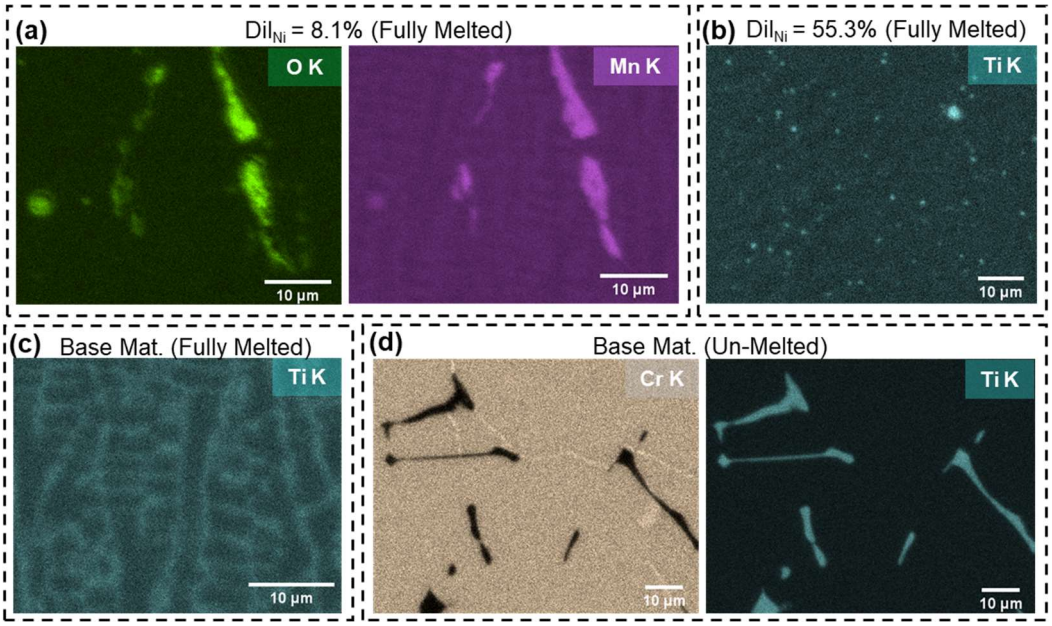

Figure 5.10: EDS data corresponding to the specimens in Figure (9). (a) MnO in the FM $(Dil)_{Ni}$ = 8.1% condition. (b) Ti-rich MC particles in the FM $(Dil)_{Ni}$ = 55.3% condition. (c) Ti-segregation in the FM Alloy 738 LC base material, corresponding to the locations of the η-phase. (d) Intragranular Ti-rich MC carbide and grain-boundary Cr-rich $M_{23}C_6$ carbides in the UM Alloy 738LC base material.

5.5.3 Summary and Discussion: Constituent Phases as a Function of Dilution Level

Together, Figures 5.7-5.10 show that six out of the twelve prospective phases from Figure 5.4 were determined from XRD analysis to be present in at least one experimental condition: the major-phase FCC solid-solution, MnO, both MC and $M_{23}C_6$ carbides, and both GCP phases (γ' and η). Table 5.2 summarizes the dilution/melting conditions for which each constituent phase was present. Across the range of experimental conditions, fewer phases were generally found to be present than predicted by the simulated dataset in Figure 5.2. None of the three TCP phases was detectable by XRD, and no experimental evidence of the BCC solid solution predicted to exist across many dilution conditions in Figure 5.2 was found. The presence of both γ' and η in FM Alloy 738LC ($(Dil)_{Ni}$ = 100%) suggests that postmortem conditions lay between pure Scheil and pure equilibrium conditions, indicating that some evolution toward equilibrium occurred as the material cooled. Both γ' and η were only found in the unaltered Alloy 738LC composition, although the next-highest dilution level achieved experimentally was 55.3%. Figure 5.2 indicates that this is only just above the minimum dilution level for the precipitation of γ' in equilibrium conditions, and well below the minimum level for the precipitation of η in Scheil solidification, so the absence of these two phases in diffraction data for any experiments with $(Dil)_{Ni} < 100\%$ agrees with simulated data.

The presence of low-temperature $M_{23}C_6$ carbides in every experimental condition is further evidence that evolution toward equilibrium occurred as each laser-weld cooled. These carbides also indicate that carbon is present in the UM MPEA, although this material is nominally carbon-free. However, the absence of MC carbide below $(Dil)_{Ni}$ = 30.2% indicates that a critical level of strong MC-carbide formers (primarily Ti) must be introduced to the MnFeCoNiCu-type MPEA before the MC phase is precipitated under laser-melting conditions. MC is also largely absent in FM Alloy 738LC ($(Dil)_{Ni}$ = 100%), as indicated by the absence of the (200) MC peak in Figure 5.8(b) and low frequency of occurrence of the (220) peak in Figure 5.8(c), as well as the clear absence of Ti-rich particles in Figure 5.10(c). In this condition, the Ti-rich η-phase is thought to inhibit MC carbide formation by binding Ti in the system. Finally, MnO particles, present in the UM MPEA due to insufficient environmental control during arc-casting, remained present in the relatively low heat-input laser weld when $(Dil)_{Ni}$ = 8.1%, but were fully re-dissolved into the matrix at higher weld heat-inputs.

Table 5.2: Summary of experimental conditions in which constituent phases were found to be present

$(Dil)_{Ni}$	Condition	FCC Matrix	γ'	η	MC Carbide	$M_{23}C_6$ Carbide	MnO
0% (MPEA)	Un-Melted (UM)	✓				✓	✓
8.1%	Fully Melted (FM)	✓				✓	✓
30.2 – 55.3%	Fully Melted (FM)	✓			✓	✓	
100% (738LC)	Fully Melted (FM)	✓	✓	✓		✓	
100%	Un-Melted (UM)	✓	✓		✓	✓	

As indicated by the angled dashed lines in Figure 5.8, the $M_{23}C_6$ carbide and the FCC matrix experienced a significant shift in lattice parameter as a function of dilution level (i.e., composition). For the $M_{23}C_6$ carbide, this shift indicates that this phase can accommodate a variety of metallic elements depending on the bulk composition in which it exists, consistent with reports on the relative stability of various binary and ternary $M_{23}C_6$ manifestations [142]. Because $M_{23}C_6$ was not widely predicted in simulation data (Figure 5.2), the observed shift in lattice parameter could not be correlated to simulated composition data. However, Figure 5.8(b) and (c) show that the observed lattice parameter of the MC phase was constant across dilution levels, consistent with the near-constant composition of MC predicted in Figure 5.3(b). This example demonstrates how simulated composition data can inform the analysis of experimental XRD, as indicated in Figure 5.1.

For the FCC matrix, Figure 5.11 compares the experimentally observed lattice parameters with those calculated via Equation 5.3 for the simulated matrix compositions in both equilibrium and Scheil conditions. Simulated equilibrium compositions are those at 843°C, and simulated Scheil compositions are those calculated via Equation 5.2. For experimental conditions in which an interdendritic segregation was observed (see Figure 5.8b), the lattice parameters shown are averages of the main dendrite peak and interdendritic shoulder peaks, weighted according to peak intensity. Figure 5.11 shows that all three datasets have downward trends with increasing dilution level. Of the two simulated datasets, the equilibrium data has a steeper downward trend in lattice parameter because γ' precipitation at high dilution levels (Figure 5.2) depletes the FCC matrix of

Al and Ti, elements with relatively large atomic radii [1]. While the constituent phases present indicated that experimental conditions lay between pure Scheil and pure equilibrium, the experimental dataset in Figure 5.11 more closely matches the behavior of the Scheil simulation, indicating that the Scheil model is a better predictor of matrix composition for this experiment.

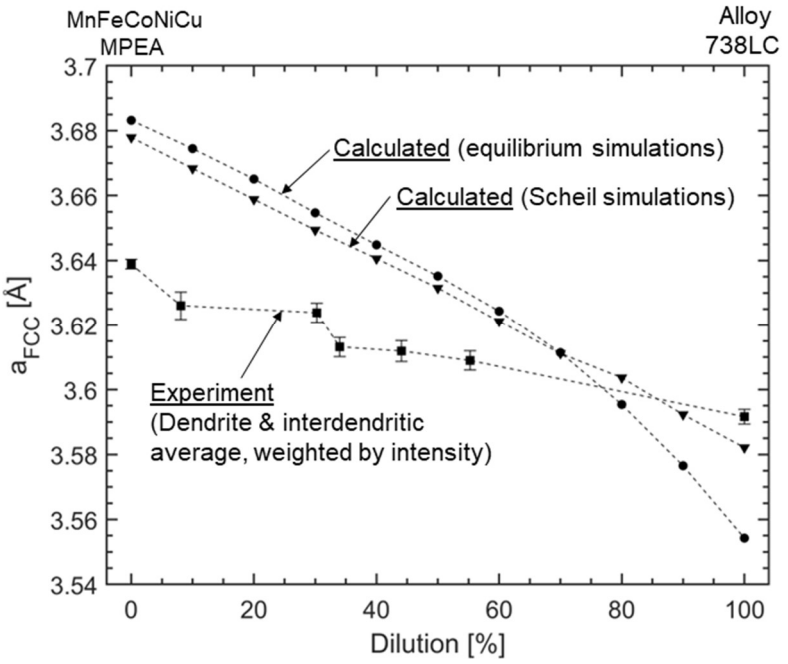

Figure 5.11: Comparison of experimental and calculated lattice parameters of the FCC matrix as a function of dilution level. Calculated lattice parameters were found by employing Equation 5.3 on composition data from equilibrium and Scheil simulations.

Furthermore, the experimental dataset in Figure 5.11 never deviates from the calculated lattice parameter for the Scheil-predicted compositions by more than 0.04 Å in either direction. At a dilution level of 100%, the experimental lattice parameter is 3.592 Å, the literature-reported lattice parameter is 3.586 Å [138], and the lattice parameter predicted by Equation 5.3 and Scheil composition data is 3.582 Å. Considering that factors other than composition that affect lattice parameter, such as residual stresses imparted by laser welding, are ignored in this analysis, this agreement is strong. A more detailed assessment incorporating estimated residual stresses in the laser welds could offer insights pertaining to the discrepancy in slope between the experimental and calculated datasets. Additionally, the analysis does not consider experimental deviations from uniform dilution in every element, *e.g.*, excess losses of volatile elements such as Mn during laser melting, which may also affect the slope of the experimental dataset in Figure 5.11. Overall, the agreement across a range of alloy compositions validates the use of the statistical hard-sphere

model in Equations 5.3 and 5.4 for the production of a composition-specific simulated XRD pattern for a disordered solid solution (e.g. Figure 5.4a) as an essential component of the presented methodology for phase identification in complex alloy systems.

5.6 Conclusions

1. A strategy alternative to conventional techniques based in the powder-diffraction file is presented for phase-identification by XRD in concentrated alloy systems. The strategy is demonstrated on a material system consisting of a MnFeCoNiCu MPEA, Ni-alloy 738LC, and a range of intermediate compositions produced by mixing the two materials via laser melting.
2. Thermodynamic simulation data using ThermoCalc's TCNI 11.0.1 and TCHEA 5.1 databases guided the creation of a system-specific diffraction library that consisted of twelve prospective phases, including three oxides found in prior study.
3. Six of the twelve prospective phases were found to be experimentally present at some point in the system composition space, which did not include any of the three detrimental TCP phases or the BCC solid solution. This finding suggests Thermo-Calc's databases may over-predict formation of TCP phases and BCC solid solutions for this material system. The presence of both non-equilibrium η-phase and equilibrium γ' in laser-melted Alloy 738LC indicates experimental conditions following solidification and cooling lay between pure Scheil and pure equilibrium. No unexpected phases were present in the experimental data, validating the use of thermodynamic simulations to construct a diffraction library of prospective phases.
4. Strong agreement between calculated and experimental lattice parameters for the disordered FCC solid solution matrix phase validates the use of the statistical hard-sphere atomic model to simulate an XRD pattern for solid solutions in concentrated alloy systems, as a critical component of the phase identification strategy.

5.7 Chapter Acknowledgments

This research is supported by the National Science Foundation with Award No. 1847630. This research used resources of the Advanced Photon Source, a U.S Department of Energy (DOE) Office of Science User Facility operated for the DOE Office of Science by Argonne National

Laboratory under Contract No. DE-AC02-06CH11357. Data was collected at Beamline 1-ID-E. Support from beamline staff was greatly appreciated. Use of the Tescan S8252G SEM was supported by the National Science Foundation Division of Materials Research Award No. 1828454. The authors would like to thank PCC-Structurals, Inc. for providing the Alloy 738LC material used in this study.

CHAPTER 6
RELATIVE EFFECTS OF DILUTION AND INTERDIFFUSION ON MULTI-PRINCIPAL ELEMENT ALLOY BRAZES OF NI-BASE SUPERALLOYS

6.1 Abstract

Multi-principal element alloys (MPEAs) are being explored as an alternative to conventional transient liquid phase Ni-base fillers for brazing Ni-base superalloys. During brazing, both filler categories will experience a degree of dilutive mixing with the base material due to progressive liquation at the solid/liquid interface. However, this dilution will have a greater impact on the composition of an MPEA filler, because its composition is initially more disparate from that of the base material. As demonstrated on brazes of Alloy 600 and Alloy 738LC using nominal $Mn_{35}Fe_5Co_{20}Ni_{20}Cu_{20}$ MPEA filler, the dilutive composition changes experienced during brazing far outmatch those resulting from interdiffusion during subsequent short-term heat treatments at industrially relevant temperatures. In Alloy 600 brazes, dilution introduces Cr to the MPEA filler zone, while this phenomenon also introduces Al, Ti, Nb, Mo, Ta, and W to the filler when brazing Alloy 738LC. Although the initial MPEA composition has been shown to display a single-phase FCC microstructure, the uptake of these non-native elements by the MPEA filler renders critical an evaluation of its single-phase microstructural stability at the resultant as-brazed composition and following both short-term and long-term interdiffusion heat treatments. This evaluation was carried out for brazes of Alloy 738LC using site-specific synchrotron X-ray diffraction and scanning electron microscopy. In the Alloy 738LC base material and in the filler/substrate transition zone, a γ/γ' + MC carbide microstructure was observed in the as-brazed condition, and a γ + Al_2O_3 contaminant oxide microstructure was observed in the MPEA filler. The oxides are a result of atmospheric contamination in laboratory-scale MPEA manufacturing conditions. A high-throughput implementation of equilibrium thermodynamic calculations accurately predicted the occurrence of γ' across the braze composition profile. The only microstructural evolution observed following a short-term interdiffusion treatment at 843°C for 24h was the precipitation of a band of Cr_2O_3 particles in the filler/substrate transition zone. No detrimental topologically close packed phases were detected in the microstructures, indicating short-term accommodation of the non-native elements introduced by dilution in the ductile disordered FCC phase of the MPEA filler. While extended heat treatments are necessary to confirm long-term compatibility, high-throughput

thermodynamic calculations indicate the MPEA filler is expected to outperform the Alloy 738LC base material in the suppression of detrimental phases such as σ after prolonged high-temperature exposure.

6.2 Introduction

Ni-base superalloys are employed as high-temperature members in gas turbine engines, corrosion-critical oil and gas components, and in certain cryogenic applications [5, 7-9]. When these alloys suffer cracking during service, braze repairs – performed by melting only a filler material and allowing it to flow into a crack or gap via surface wetting and capillary action – offer a minimally invasive salvage alternative [25]. Transient liquid phase (TLP) processes represent one of the most widespread methodologies by which braze repairs of Ni-base superalloys are accomplished in a contemporary industry setting [39]. TLP processes are designed to employ a filler material whose melting point is depressed by one or more fast-diffusing elements, such as boron. To achieve a homogenous resultant microstructure, these processes rely on isothermal solidification at a selected bonding temperature, driven by a local composition change caused by the migration of fast-diffusing element(s) into the base material.

Though there is some variability among authors in how TLP process stages are delineated, all recognize three major phenomena that are theorized to occur in series in an ideal process [39, 45, 50]. Stage I consists of substrate dissolution, in which solid base material immediately adjacent to the molten filler is progressively consumed until the composition of the liquid phase matches the liquidus at the bonding temperature. Stage II comprises the abovementioned isothermal solidification driven by melt-point depressant element diffusion. Lastly, Stage III involves continued diffusion in the solid-state to fully homogenize the concentration profile of these elements. As theorized, these three stages should result in a microstructure nearly indistinguishable from that of the parent material [39]. However, practically, a diffusion-affected zone (DAZ) characterized by boride precipitation is commonly observed [45, 52-59], resulting from boron diffusion outpacing the establishment of equilibrium in the system [59]. These details are discussed further in Chapters 2 and 3 of this thesis.

In conventional TLP literature, Stages II and III are the primary areas of focus, because the extent of isothermal solidification and subsequent homogenization directly impact performance of the braze-repaired microstructure by governing the extent of brittle phases therein. Additionally,

the formation of a DAZ is likely to occur during these stages [54]. By comparison, substrate dissolution during Stage I is given relatively little attention. Certain authors [50, 54] discuss the mathematics and calculate the time required for substrate dissolution to occur, which is usually rapid in comparison to the full TLP process duration. However, the dilutive effect of substrate dissolution and its resultant composition change of the molten filler is almost never considered beyond its impact on the concentration of melt-point depressants. This is understandable, because fillers for TLP processes, such as the *BNi* series, are designed to closely mimic the composition of many Ni-superalloys in all the other alloying elements (*e.g.,* Cr, Fe, etc.). TLP fillers are designed in this manner because the objective is to create a compositionally homogeneous microstructure following complete isothermal solidification [39]. Thus, substrate dissolution only dilutes the melt-point depressants to the liquidus composition, and it does not result in a large concentration change in the other constituent elements of the melt pool.

In contrast, a multi-principal element alloy (MPEA) filler will inherently have significantly different concentrations of all constituents than the base material, owing to the variety of elements considered in the design of an MPEA and the lack of a single basis element such as Ni [1]. This relative disparity in initial concentration is illustrated in Figure 6.1. This figure provides an example, comparing the difference in initial composition between Ni-base Alloy 600 substrate [13] and two different fillers: commonly employed TLP filler BNi-2 [40], and the $Mn_{35}Fe_5Co_{20}Ni_{20}Cu_{20}$ MPEA [2, 79, 80, 115]. Except for Fe, the Alloy 600/MPEA pair displays a much greater disparity in every shared constituent element than the Alloy 600/BNi2 pair. Because the concentrations are more disparate, the dilutive effect of any substrate dissolution that occurs will have a more profound influence on the composition of the molten pool when using the MPEA filler than in the case of fillers for TLP processes. The resultant concentration of any constituent element for a given dilution level can be calculated by rearranging the conventional weld dilution equation [5, 130]:

$$C_{Filler,\ Resultant} = C_{Filler,\ Initial} + (Dil) * (C_{Base\ Material} - C_{Filler,\ Initial}) \qquad (6.1)$$

Where *C* represents concentration of an element in the material described in the subscript, and *Dil* represents the dilution level. For example, 20% dilution in the Alloy 600 substrate does not alter

the concentration of any BNi-2 constituent by more than 2 – 3 at. %, but it results in an increase of over 10 at. % in the Ni concentration of the MPEA filler, among other changes.

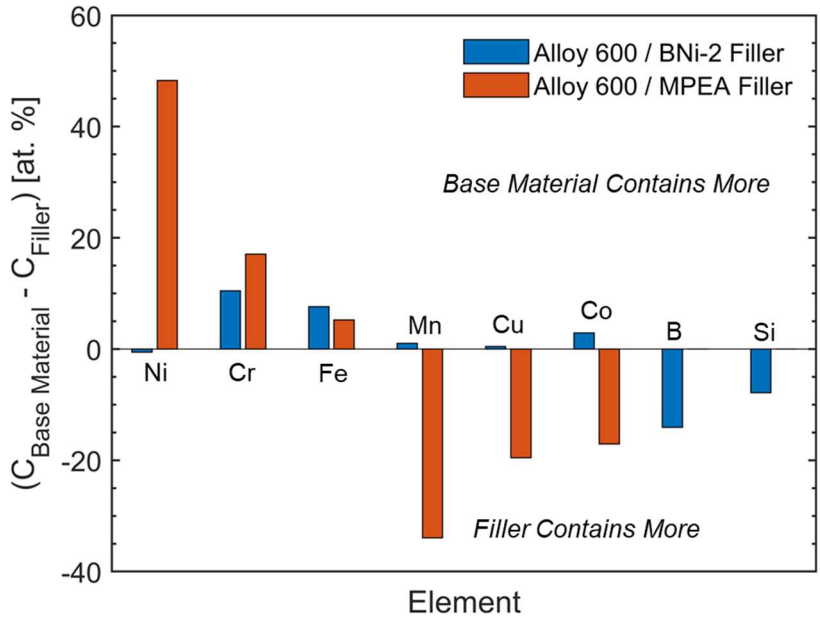

Figure 6.1: Disparity in initial composition between the following alloy pairs: Alloy 600/BNi-2, and Alloy 600/$Mn_{35}Fe_5Co_{20}Ni_{20}Cu_{20}$.

MPEAs have only been rigorously investigated as potential braze fillers for the last five years, and previous work on MPEA braze fillers does not consider dilutive effects. Chapter 3 of this thesis [115] notes that when brazing at a fixed temperature above the MPEA liquidus, thermodynamics dictate that some extent of substrate dissolution should occur, as it does in TLP processes, but this prior study does not rigorously examine dilution. The initial study investigating furnace brazes of Alloy 600 using $Mn_{35}Fe_5Co_{20}Ni_{20}Cu_{20}$ MPEA discusses the effects of Cr introduction to the filler, but it does not distinguish between the effects of liquid-state dilution and solid-state interdiffusion during brazing and cooling [2]. Some additional studies of MPEA fillers [66, 67] target equiatomic initial filler compositions to maximize configurational entropy, but they do not consider that this metric is likely to change appreciably as the result of a dilutive composition change during brazing. This paper aims to fill each of these knowledge gaps by directly examining the dilutive composition change of an MPEA filler when brazing two superalloy substrates: solid solution strengthened Alloy 600 and γ'-precipitate strengthened Alloy 738LC. The effects of the dilutive composition change are compared to the effects of solid-state

interdiffusion that occurs during short-term exposure to elevated temperatures encountered by these Ni-base alloys in service, and the implications of the resultant composition profiles on γ'-precipitation and the other constituent phases in the Alloy 738LC braze are explored.

6.3 Experimental Procedures

6.3.1 Fabrication of MPEA Filler

MPEA ingots of approximate composition $Mn_{35}Fe_5Co_{20}Ni_{20}Cu_{20}$ were arc-cast directly from pieces of the pure constituent elements on a water-cooled copper hearth in an argon-backfilled stainless-steel chamber using a tungsten inert gas welding electrode and power source. The chamber was evacuated and backfilled three times prior to each melt, and a piece of commercially pure titanium was melted prior to the MPEA ingot to bind residual oxygen within the chamber. Each ingot was flipped and melted three times to ensure bulk compositional homogeneity. More details on the fabrication process can be found in [2]. Following casting, ingots were machined by milling to remove visible surface oxide and casting defects. Preform filler foil of approximate thickness 300 μm was subsequently produced via cold rolling.

6.3.2 Brazing and Interdiffusion Heat Treatments

Rolled plate of Alloy 600 and castings of Alloy 738LC were obtained from external suppliers. Each material was cut in its as-received condition using a Leco MSX-series abrasive cut off saw to produce rectangular prismatic coupons measuring 10 mm x 6.5 mm x 6.5 mm. Faying surfaces were finished to 600 grit, and subsequently vacuum-furnace brazed in a sandwich configuration using the MPEA preform filler foil with unfixed joint clearance. Brazing was performed at a vacuum level of 10^{-5} torr or better as measured using an ion gauge. Both materials were brazed at 1200°C for a hold duration of 90 minutes followed by furnace cooling without any inert gas quench, based on the optimized process for Alloy 600 brazes reported in [2].

After brazing, some specimens were kept in the as-brazed state to assess the pure effects of dilution that occurred during the brazing treatment. Other coupons were aged in an open-air furnace to evaluate the subsequent effects of short-term solid-state interdiffusion on the composition profile. Alloy 600 brazes were aged at 800°C for 100 hours, and Alloy 738LC brazes were aged at 843°C for 24 hours, followed by air cooling. These time-temperature combinations

were selected based on the strengthening mechanisms and industrial use of each respective alloy. Alloy 600, a solid-solution strengthened alloy, has no industrial aging procedure, so 800°C was selected because it is on the high end of service temperatures typically encountered by this alloy [13]. 100 hours was selected to represent a short service interval of a duration frequently employed in creep testing [31]. The heat treatment for Alloy 738LC, a γ'-precipitate strengthened alloy was taken directly from the final step of the recommended aging procedure for this alloy to achieve maximum strength [18].

6.3.3 Characterization

Following brazing and heat treatments, coupons of brazed Alloy 738LC were cut to 1 mm thickness and analyzed via high energy synchrotron X-ray diffraction (XRD) for a site-specific assessment of the constituent phases with variation in the composition profile of the filler zone. The constituent phases in the Alloy 600 brazes were previously characterized in Chapter 4. For the Alloy 738LC brazes, an X-ray beam with energy 61.332 keV was directed in transmission through the specimens, and patterns were collected using a GE Revolution 41RT flat-panel detector [143] positioned at a working distance of 750 mm. To map the constituent phases as a function of the composition profile, a series of five line-scans were taken at the positions indicated in Figure 6.2. The incident beam dimensions were 100 µm horizontally by 50 µm vertically, and for each line scan, the sample was translated vertically in 50 µm increments, creating a continuous linear map of site-specific XRD patterns. A description of sample alignment techniques including how the braze centerline was located is available in Appendix A. There was 1 mm lateral spacing between each line scan. Patterns were integrated using the fit2D software, and data from equivalent positions among the five line-scans was averaged, to better discern low-intensity peaks from noise in the data.

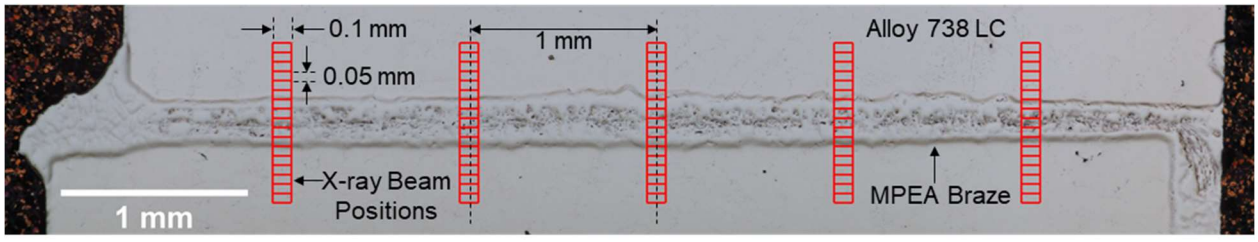

Figure 6.2: Macroscopic view of an Alloy 738LC braze coupon with the beam positions at which synchrotron XRD patterns were collected indicated.

To supplement the site-specific XRD patterns, scanning electron microscopy (SEM) was used to image constituent phases in the Alloy 738LC brazes. Coupons were prepared for SEM via standard metallographic polishing with a final step of 0.05 μm colloidal silica on a vibratory polisher. Imaging was performed on a Tescan S8252G SEM at an accelerating voltage of 5 keV and a beam current of 300 pA. To obtain the composition profile across both Alloy 600 and Alloy 738LC brazes in the as-brazed and heat-treated conditions, energy dispersive spectroscopy (EDS) line-scan data was also collected using a JEOL 7000F field emission SEM at an accelerating voltage of 20 keV. EDS line-scan datasets were quantified using the ZAF correction method in the EDAX-TEAM software. To obtain statistical composition data, line scans were collected from a minimum of three distinct locations for each brazed alloy in each condition.

6.3.4 Thermodynamic Calculations

To compare experimentally observed phases with those predicted by thermodynamic simulations across the composition profile, quantified composition data from an Alloy 738LC braze EDS line-scan were input into a high-throughput implementation of the single-axis equilibrium module of the ThermoCalc software. The TCHEA 5.1 database was employed for these calculations. The Alloy 738LC braze was selected for this comparison so that the predicted and observed γ' phase fraction across the composition profile could be evaluated, along with the predicted equilibrium volume fraction of any potentially detrimental phases. Simulation data were assessed at a temperature of 843°C and compared with the experimental specimens that had been aged at this temperature for 24 hours.

6.4 Results

6.4.1 Bulk Composition Change of Filler Zone

To illustrate how the composition of the filler zone was determined, Figure 6.3 shows representative SEM micrographs and EDS line scans taken from both an Alloy 600 braze and an Alloy 738LC braze, both in the as-brazed condition. Figure 6.3 shows that the concentration profile can be broken down into three zones: base-material, a transition zone, and the filler zone. The elements detected and quantified in the Alloy 600 braze are Cr, Mn, Fe, Co, Ni, and Cu, while Al, Ti, Nb, Mo, Ta, and W are additionally detected and quantified in the Alloy 738LC braze. Because

they are difficult to quantify accurately using EDS, light interstitial elements such as carbon and oxygen are not included in the composition profile, but the experimental detection of carbide and oxide phases is discussed in later sections. As previously reported [2], Mn and Cu are prone to centerline segregation at the expense of Fe and Co, which is observed in both composition profiles. Except for where the scan passed over an oxide inclusion particle in Figure 6.3(d), the Ni concentration profile is essentially flat in the filler zone of both brazes. For this reason, the transients in the Ni profile were used to delineate the filler zone from the transition zone between the two materials, as denoted in Figure 6.3(b) and (d). The composition of the filler zone was determined by averaging the quantified EDS data over the shaded regions shown. To compare the effects of dilution and short-term interdiffusion on the MPEA filler composition, Figure 6.4 shows the net change in concentration of all the major alloying elements in the filler zone relative to the nominal initial composition of the $Mn_{35}Fe_5Co_{20}Ni_{20}Cu_{20}$ MPEA, in both the as-brazed and heat-treated conditions, for both the Alloy 600 and Alloy 738LC brazes.

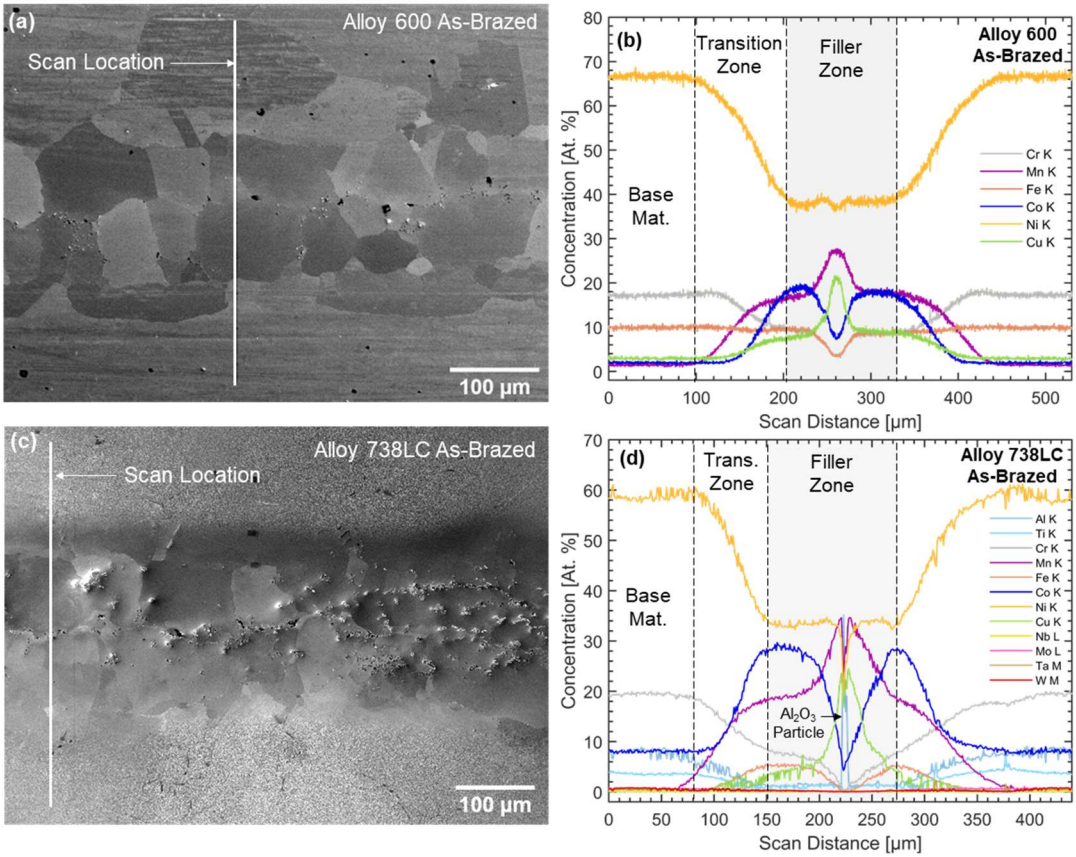

Figure 6.3: SEM micrographs and quantified EDS line-scan data from (a-b) Alloy 600 braze using the MPEA filler, and (c-d) Alloy 738LC braze using the MPEA filler

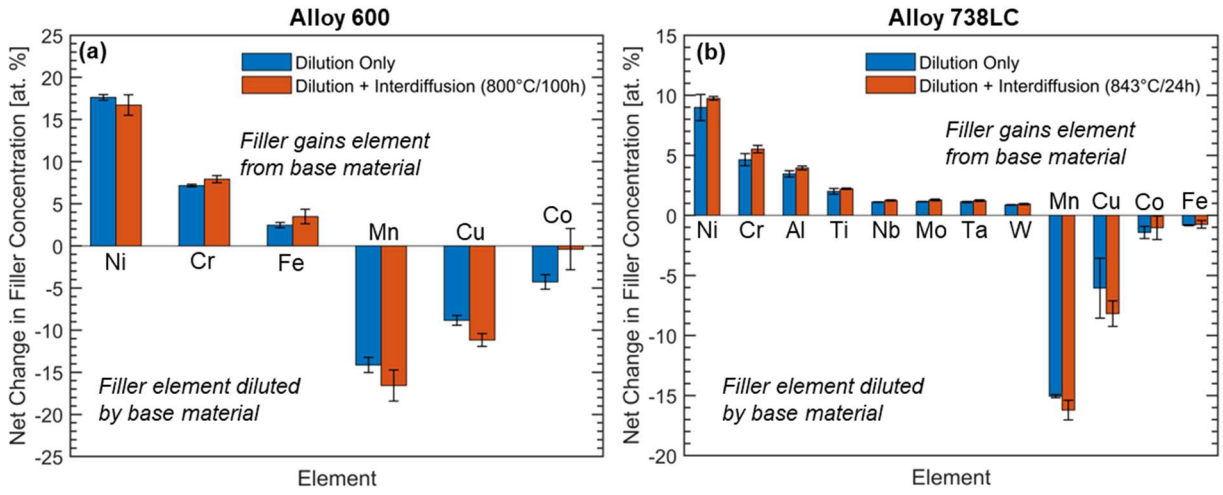

Figure 6.4: Net change in composition of the constituent elements in the filler zone following either brazing only or brazing plus heat treatment, relative to the initial nominal composition of $Mn_{35}Fe_5Co_{20}Ni_{20}Cu_{20}$ MPEA. (a) Alloy 600 brazes, and (b) Alloy 738LC brazes.

Figure 6.4(a) shows that the dilutive composition change in the Alloy 600 braze leads to a gain of approximately 18 at. % Ni, 7 at. % Cr, and 2 at. % Fe, which are all present in greater concentrations in Alloy 600 than in the initial MPEA composition. In contrast, Mn, Cu, and Co, which are nearly absent in Alloy 600, become increasingly dilute in the filler zone because of dilutive mixing with the base material during brazing. The measured concentration losses in the filler zone are 14 at. % for Mn, 9 at. % for Cu, and 4 at. % for Co. Continued interdiffusion during heat treatment should serve to promote some extent of homogenization of the composition profile, and thus further the gains or losses in concentration of each element in the same direction as experienced during dilution. The data in Figure 6.4(a) reflect this for Cr, Fe, Mn, and Cu, which all exhibit a mild further shift (no greater than 2.5 at. %) away from the initial concentration of the MPEA filler. The data for Ni and Co reflect the opposite of the expected trend, demonstrating a reversion back toward the initial concentration, albeit with relatively large scatter in the data (reflected by the error bars representing one standard deviation among the scans analyzed). This reversion is likely not phenomenological, but rather a reflection of variability among scan locations. Chapter 4 discusses that the thickness and strength of segregation of the filler zone both may vary considerably among samples, and the specimens heat treated in this study were different specimens from those left in the as-brazed condition. The abovementioned variations were observed among the scan locations assessed in this study, demonstrating that to assess the effects

of interdiffusion more rigorously, a tracked, site-specific characterization of composition evolution would be necessary.

Nevertheless, an important takeaway from Figure 6.4(a) is that the dilutive composition change from brazing definitively outmatches the interdiffusion-driven change brought about by subsequent exposure to 800°C for 100h. As discussed in Section 6.5, this heat treatment is relatively short in duration, and the effects of continued interdiffusion in the long term should not be ignored. However, the dilutive composition change alone represents a large enough *transit in composition space* that a single-phase FCC microstructure in the *initial* filler does not guarantee that the same microstructure will exist after dilution. Chapter 4 rigorously examined the constituent phases in Alloy 600 brazes, and it was found that, barring some uptake of nitride and carbide phases from the base material and the formation of contaminant oxides, the dilutive composition change in these brazes did not impact the single-phase stability of the MPEA filler.

Because of the relatively greater compositional complexity of Alloy 738LC, the impact of the dilutive composition change on the microstructure in brazes of this base material must be even more critically evaluated. Chapter 5 provides an account of the calculated and observed phases across varying dilution (mixing) levels between the MPEA filler and Alloy 738LC, but the dilutive composition change under furnace brazing conditions was not assessed. Figure 6.4(b) indicates that, in addition to gaining 9 at. % Ni from the base material, the filler zone also experiences uptake of Cr, Al, Ti, Nb, Mo, Ta, and W in appreciable quantities during brazing, none of which are native to the MPEA filler. In the as-brazed condition, Cr is introduced at roughly 5 at. %, Al at 3.5 at. %, Ti at 2 at. %, and each of the four refractory elements approach 1 at. % in the filler zone. Meanwhile, Mn, Cu, Co, and Fe are diluted relative to the initial MPEA composition. Of these, only Co is native to Alloy 738LC, but it is at lower concentration in the base material than in the filler alloy, so mixing with the base material results in a loss of concentration. As a result of dilution alone, the concentration of Mn decreases by 15 at. %, Cu by 6 at. %, Co by 1.5 at. %, and Fe by 1 at. %. While these data are only an estimate resulting from quantification of EDS spectra, this analysis provides a working approximation for the effects of the dilutive composition change in Alloy 738LC brazes. The composition data following the interdiffusion heat treatment at 843°C for 24h lie further from the initial MPEA composition than in the as-brazed condition – which is expected – for every element except for Co and Fe. However, as with the Alloy 600 brazes, the relative contribution of short-term interdiffusion to the overall composition change is small in

comparison to the dilutive composition change, again highlighting the importance of considering dilution when brazing with an MPEA filler.

6.4.2 Microstructure Assessment for Alloy 738LC Braze

Chapter 4 of this thesis offered a comprehensive assessment of the constituent phases and microstructure of Alloy 600 brazes in the as-brazed state and following a heat-treatment at 800°C for 100h. The effect of the composition changes reported in Figure 6.4(a) on the single-phase stability of the MPEA filler has therefore been thoroughly characterized. The following sections provide a similar assessment of the effects of the measured composition changes in Figure 6.4(b) for the Alloy 738LC brazes. Because Alloy 738LC contains appreciable MC carbides and a high volume fraction of γ' precipitates, it is necessary to assess the single-phase stability of the MPEA in the context of the extent to which these beneficial phases can be incorporated into the microstructure of the filler zone.

6.4.2.1 Predicted Microstructure

Figure 6.5(a-b) display an SEM micrograph and quantified EDS line scan dataset that were input into a high-throughput implementation of ThermoCalc to predict constituent phases across the composition profile of the Alloy 738LC braze. This sample was subjected to the interdiffusion treatment at 843°C for 24h, but as Figure 6.4(b) indicates, there is little difference in the bulk composition of the filler zone before and after this heat treatment. Recall that light elements such as carbon and oxygen are not included in the EDS quantification, so any carbide or oxide phases were not evaluated in this calculation.

Predicted phases were evaluated at equilibrium conditions at the interdiffusion temperature of 843°C. Other than the FCC (γ) matrix, the only two phases predicted to form at this temperature with any degree of consistency were beneficial γ' and the detrimental topologically close-packed (TCP) σ-phase, which is mainly predicted to occur in the base material and not the filler zone. Chapter 5 suggests that the TCHEA 5.1 database may over-predict σ-phase formation in this system, and no appreciable σ-phase was observed experimentally via SEM or XRD techniques (section 3.2.2). However, the absence of TCP phases is assessed more critically in Section 6.5.3. Unlike σ-phase, γ' is observed experimentally, and the variation of the predicted γ' phase volume fraction is shown in Figure 6.5(c). As indicated, the volume fraction is predicted to be

approximately 0.45 – 0.5 in the base material, consistent with literature for Alloy 738LC [144]. Moving along the composition profile, this base-material level is followed by a steep drop-off in predicted γ' volume fraction in the transition zone. Note that the γ' phase fraction is predicted to drop to zero before the flat region of the Ni concentration profile that characterizes the filler zone begins, and the entire filler zone is predicted to be devoid of γ'.

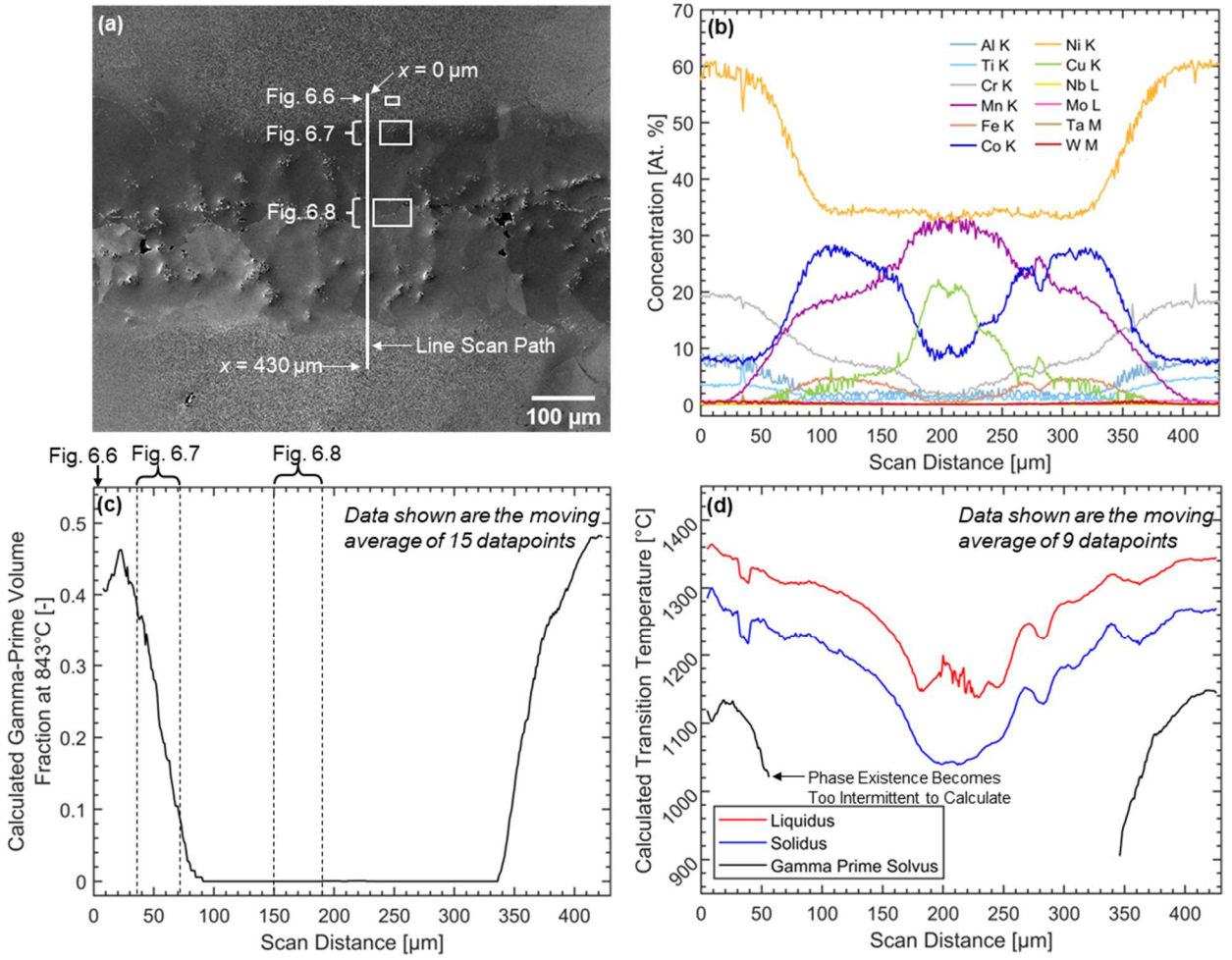

Figure 6.5: (a) SEM micrograph of Alloy 738LC braze, displaying the location of an EDS line-scan and the adjacent locations of site-specific constituent phase assessments summarized in Figures 6.6 – 6.8, for reference. (b) Quantified EDS line-scan data from the location indicated in (a), which was input into a high-throughput implementation of ThermoCalc's single-axis equilibrium calculator module, with key outputs shown in (c-d). (c) Variation of the predicted γ' volume fraction at 843°C along the composition profile. (d) Variation of the predicted liquidus, solidus, and γ'-solvus temperatures along the composition profile.

Figure 6.5(d) shows the variation of the calculated phase transition temperatures across the composition profile. The γ' solvus temperature drops from approximately 1140°C in the base

material into the range of 900 – 1000°C before the existence of the phase in the thermodynamic simulations becomes too intermittent to report the solvus. The solidus and liquidus are also reported, and the effect of the (Mn, Cu) centerline segregation in suppressing these temperatures is evident. In addition to those reported in Chapter 4, this behavior provides another reason why it is desirable to mitigate this centerline segregation, to have a more uniform solidus and liquidus profile throughout the filler zone.

Overall, the calculations summarized in Figure 6.5 show that when interstitial elements are not considered, the single-phase stability of the MPEA filler is largely predicted to extend to the composition space spanning the changes resulting from dilution reported in Figure 6.4(b). To assess the validity of these predictions, site-specific experimental characterizations were performed at the locations indicated in Figure 6.5(a).

6.4.2.2 Observed Microstructure

Figures 6.6, 6.7, and 6.8 illustrate site-specific microstructural characterizations at key locations spanning the composition profile, as indicated in Figure 6.5. Each figure contains electron micrographs of the braze in both the as-brazed and heat-treated conditions, alongside synchrotron XRD data at the corresponding distance from the braze centerline. It is important to note that the XRD patterns displayed do not represent powder data, as the diffracting grain population was low, due to the filler grains exceeding 100 μm as shown in Figure 6.3(c). The Alloy 738LC substrate was received in its as-cast condition with grains that were even larger. Because of the non-powder nature of the data, the relative intensities of the peaks corresponding to each phase cannot be inferred to correspond with phase fraction. Additionally, certain individual peaks may have high intensity due to the favorable orientation to a Bragg condition of a particular grain in a given scan, while other peaks may be nearly absent. Despite these considerations, the peak position data and the application of the methodology outlined in Chapter 5 still allow for a comprehensive constituent phase assessment, especially when supplemented by SEM imaging and EDS data.

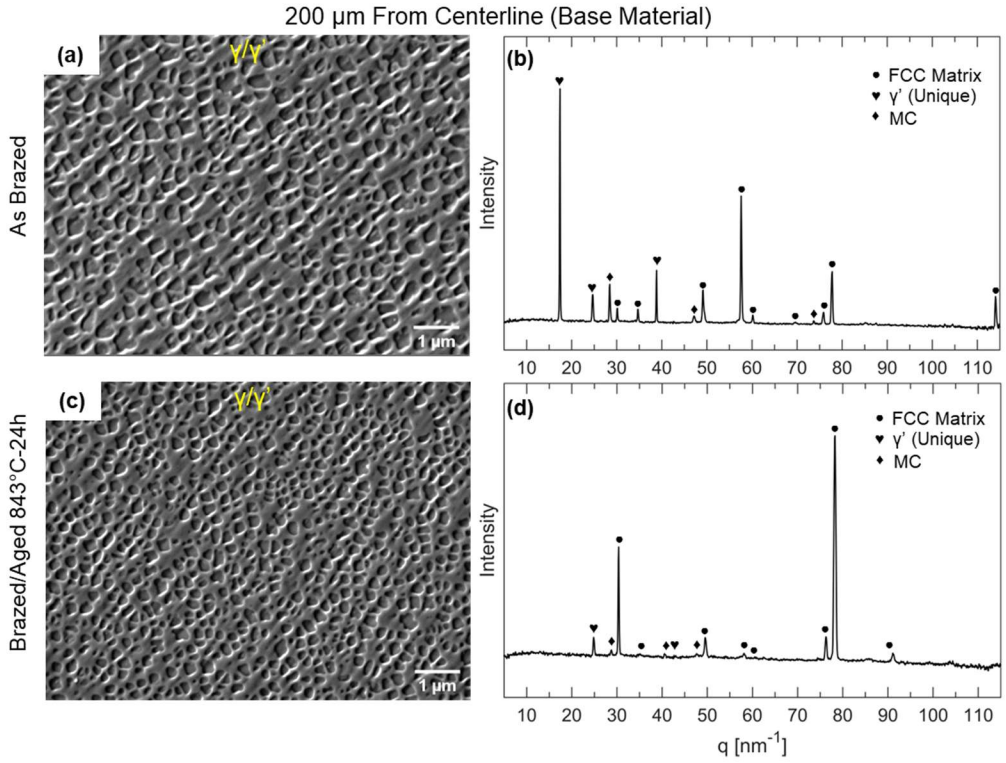

Figure 6.6: Characterization of the Alloy 738LC braze microstructure 200 µm from the centerline, in the base material zone. (a-b) The as-brazed condition, (c-d) after heat treatment at 843°C for 24h. (a, c) SEM micrographs at 30,000x magnification, showing the γ/γ' structure in detail. (b, d) Site-specific synchrotron XRD patterns from the same location ± 25 µm.

Figure 6.6 shows the microstructure 200 µm from the braze centerline, which lies near the edge of the base-material zone at the location indicated in Figure 6.5(a) and (c). The SEM micrographs are taken at 30,000x magnification to show the γ/γ' microstructure in detail. In these and following synchrotron XRD patterns, the peaks labeled "FCC matrix" correspond to the γ phase. Since γ and γ' have a very similar lattice parameter, both phases contribute to diffracted intensity at these peaks; however, for clarity regarding the presence or absence of γ' in a pattern, only the superlattice reflections unique to γ' are labeled with the corresponding symbol. The results in Figure 6.6 indicate that the constituent phases at the edge of the base-material zone include only γ, γ', and MC carbide particles that are native to Alloy 738LC. No non-native phases are detected at this location, either in the as-brazed condition or following the interdiffusion heat treatment. Since the brazing temperature of 1200°C is well above the γ' solvus temperature (Figure 6.5d), the presence of γ' in the as-brazed microstructure is most likely accounted for by re-precipitation from the solutionized condition, which develops in the braze holding step, during the slow furnace

cooling cycle. These findings indicate that when slow furnace cooling is employed, it is not necessary to employ a conventional two-step solutionizing-and-aging treatment after brazing to re-introduce γ' to the material in a general. However, it is still necessary to employ a two-step aging treatment of 1120°C-2h followed by 843°C-24h to achieve an optimum γ' morphology and mechanical properties, as described in [18, 144].

Figure 6.7 provides a microstructural assessment 150 μm from the braze centerline, which is in the transition zone between the base and filler materials, as shown in Figure 6.5 (a) and (c). A lower magnification of 6,000x was selected for the SEM micrographs at this location. This scale provides an image of larger particles, such as the MC carbides previously detected in Figure 6.6(b) and (d), and it illustrates the gradient in γ' content in this region. This gradient is indicated by the gradually diminishing etched appearance of the SEM micrographs in the downward direction, toward the braze centerline. In agreement with the calculated data in Figure 6.5(c), the γ' content falls sharply throughout the transition zone and diminishes entirely by the location at which the Ni-concentration profile flattens. The SEM and XRD data in Figure 6.7 also show the precipitation of Cr_2O_3 during the 843°C-24h interdiffusion treatment, which marks the only significant change in microstructure brought about by this heat treatment. These particles, with a needle-like morphology, were identified in the SEM micrographs and distinguished from the blockier Ti-rich MC-carbide particles by evaluating the corresponding EDS-map data depicted in Figure 6.7(e-g). Figure 6.7(f) and (g) show coincident concentration of chromium and oxygen in the needle-like particles, like that observed in particles on the fracture surfaces of Alloy 600 brazes heat-treated at 800°C, as described in Chapter 4. Like the oxides detailed in that chapter, these chromium oxides precipitate during heat treatment due to supersaturation of dissolved oxygen in the MPEA filler, resulting from poor atmosphere control during the MPEA manufacturing process.

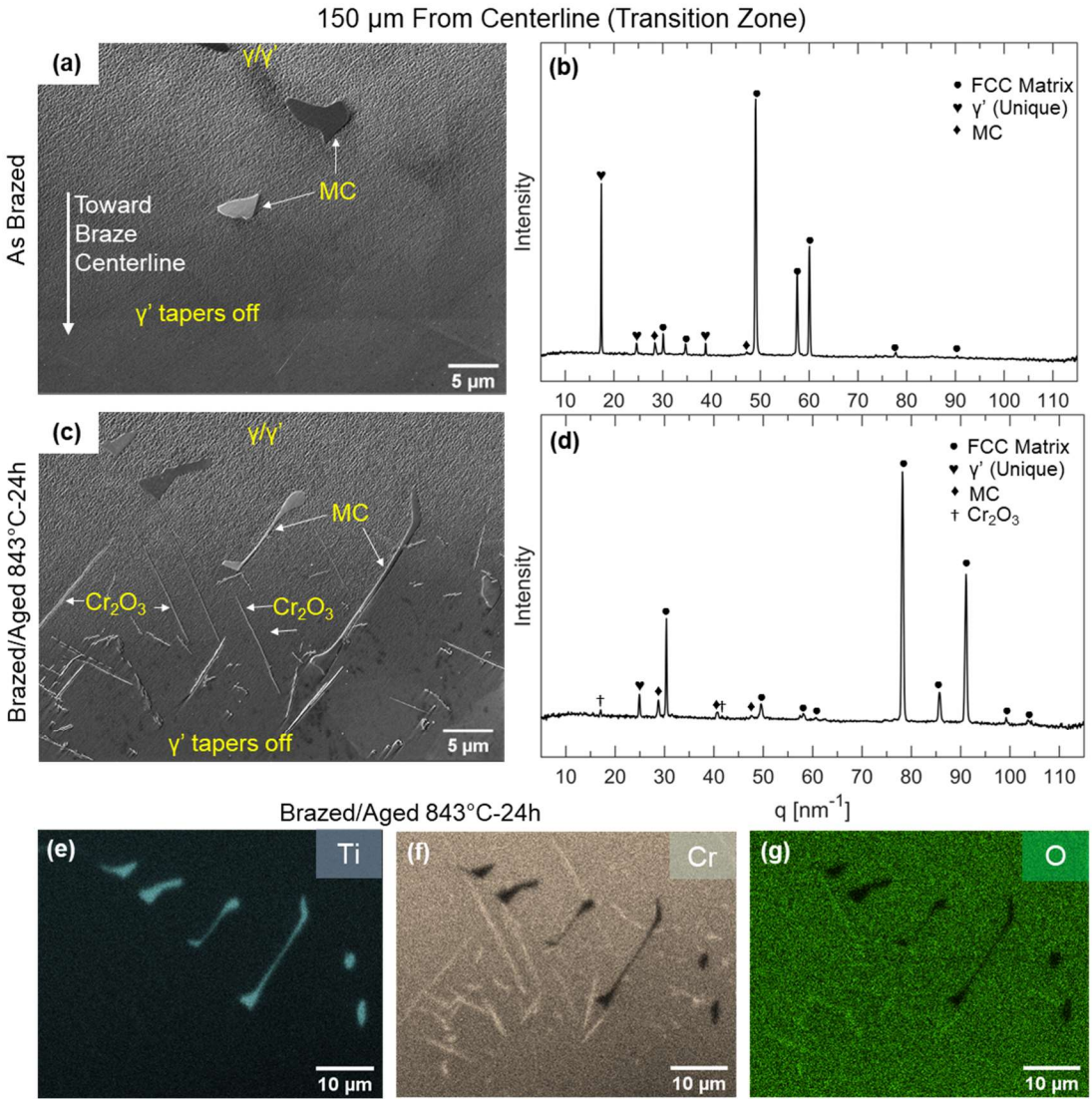

Figure 6.7: Characterization of the Alloy 738LC braze microstructure 150 µm from the centerline, in the transition zone between base and filler zones. (a-b) The as-brazed condition, (c-g) after heat treatment at 843°C for 24h. (a, c) SEM micrographs at 6,000x magnification, showing the gradient in the γ'-content, and larger particles contained in the matrix. (b, d) Site-specific XRD patterns from the corresponding locations. (e-g) EDS element maps for Ti, Cr, and O from the location shown in (c), which assisted with the identification of particles.

Figure 6.8 shows the microstructure within 25 µm of the braze centerline, wholly within the filler zone, at the location indicated in Figure 6.5(a). As indicated by the SEM micrographs and XRD data, the FCC matrix (γ) and Al_2O_3 particles are the only two phases detected at this location; as predicted by Figure 6.5(c), there is no γ'. The Al_2O_3 particles do not appear in the XRD data in the heat-treated condition in Figure 6.8(d), despite being clearly visible in the corresponding SEM micrograph (Figure 6.8c) and being detectable throughout the work on the

Alloy 600 brazes in Chapter 4. This is likely because the GE 41RT detector used to assess the Alloy 738LC brazes has a lower dynamic range (14bit counter with approximately 1.7k counts background) than the Pilatus3X CdTe 2M detector (20 bit counter with zero background) employed in Chapter 4. The GE 41RT detector is therefore less suitable for detecting low-volume-fraction phases in non-powder data as done in this work.

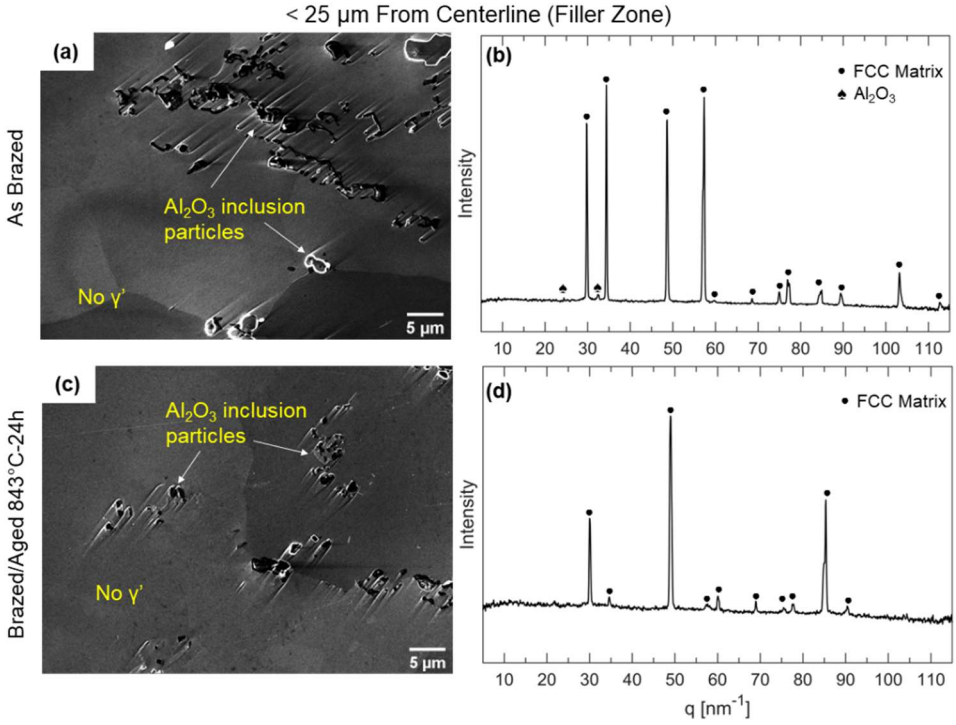

Figure 6.8: Characterization of the Alloy 738LC braze microstructure within 25 µm of the centerline, in the filler zone. (a-b) The as-brazed condition, (c-d) after heat treatment at 843°C for 24h. (a, c) SEM micrographs at 5,000x magnification, a microstructure free of γ' and containing aluminum oxide inclusions. (b, d) Site-specific XRD patterns from the corresponding locations.

The more macroscopic views of the Alloy 738LC braze in Figure 6.3(c) and 6.5(a) show the extent of Al_2O_3 particles in the filler zone, which often appear with a white edge effect in the SEM micrographs due to charging because of their low electrical conductivity. Though there is some variation in the concentration of Al_2O_3 particles in the lateral dimension in Figures 6.3(c) and 6.5(a), the concentration is generally greater than in the Alloy 600 brazes in Chapter 4. This is expected, due to the much higher aluminum content of Alloy 738LC (3.4 wt %) compared to Alloy 600 (trace amounts). As discussed in Chapter 4, only ppm levels of aluminum are necessary to form Al_2O_3, but Figure 6.4(b) shows that dilution alone introduces approximately 3.5 at. % Al (which is far less than 3.4 wt. % because Al is light) to the filler zone. The lack of Cr_2O_3

precipitation at the centerline in these Alloy 738LC brazes during heat treatment indicates that this introduced Al concentration is sufficient for Al_2O_3 to locally out-compete Cr_2O_3 as the preferred oxide at the centerline, which was not the case for Alloy 600 brazes that were subjected to heat treatment. However, as the Cr concentration rises more steeply than the Al concentration in the transition zone (see Figure 6.5b), Cr_2O_3 precipitation during heat treatment can dominate in this region, where there is abundant Cr available and still a high local dissolved oxygen content from the MPEA filler. This explanation is why a localized band of Cr_2O_3 precipitation is observed during heat treatment in the transition zone in Figure 6.7, but the filler zone is largely devoid of Cr_2O_3.

6.5 Discussion

The results presented above carry three important implications for the use of the MPEA filler in brazing Ni-base alloys. These implications include the importance of considering dilutive composition changes relative to the kinetics of interdiffusion-driven changes, the effect of dilutive composition changes on the configurational entropy of the filler, and the likelihood of forming detrimental phases during long-term high-temperature exposure. Each of these is discussed in further detail in the following sections.

6.5.1 Relative Magnitude of Dilution- and Interdiffusion-Driven Composition Changes

Figure 6.4 highlights the importance of considering the dilutive composition change when brazing Ni-base alloys using an MPEA filler. Because of the disparity between the initial compositions of filler and substrate, dilution substantially changes the composition of the filler zone. Subsequent interdiffusion treatments should drive the composition profile toward homogenization. The data in Figure 6.4 generally reflect this trend, although compositional scatter among line-scan sites precludes isolating and quantifying the effects of the interdiffusion treatment. Furthermore, the durations of the 800°C-100h and 843°C-24h interdiffusion treatments applied in this work do not constitute an appreciable fraction of the uptime of a gas turbine engine between standard maintenance intervals, which is typically on the order of 20,000 equivalent operating hours [4]. Therefore, it is important to consider the role of interdiffusion in more industrially relevant thermal histories, in addition to the heat treatments employed in this work.

A simplified analytical assessment of the kinetics of homogenization in the brazes can therefore offer important supplemental insights. Consider the homogenization of the Ni

composition profile in the Alloy 738LC braze as an example, summarized by Figure 6.9. The schematic in Figure 6.9(a) shows that prior to brazing, the composition profile exists as a step function between approximately 20 at. % Ni in the un-melted filler and approximately 60 at. % Ni in the base material. As illustrated in Figure 6.4(b), dilution alone raises the Ni concentration in the filler zone by an average of 9 at. %. The concentration of Ni in the filler zone is uniform, and the transition zone is relatively narrow, as illustrated by the solid blue line in the schematic profile in Figure 6.9(b). To a first approximation, the composition profile after brazing can therefore be modelled as a revised step function between approximately 29 at. % Ni in the filler zone and 60 at. % in the base material, as indicated by the dashed blue line in Figure 6.9(b).

While the subsequent interdiffusion of Ni and other elements between the base material and filler zone is a kinetically complex problem, an analytical estimate of the Ni composition profile can be obtained by assuming (1) the initial profile is a step function, (2) Ni diffusivity is only a function of temperature, and (3) the base material is semi-infinite and the filler material is a finite interlayer of width 2h [54, 145]. Under these assumptions, the composition *at the filler centerline* as a function of time is given by the solution to the diffusion equation

$$C(t) = (C_{BM} + C_{FZ}) * \operatorname{erf}\left(\frac{h}{\sqrt{4Dt}}\right) \tag{6.2}$$

Where C represents the variable concentration of Ni, C_{BM} and C_{FZ} are the concentrations prior to interdiffusion in the base material and filler zone, respectively, h is half-width of the filler zone (see Figure 6.9b), D is the diffusivity of Ni, and t is the interdiffusion time [145]. Note that this equation is a specific case of Equation 2.1 in which the variable x is fixed at zero to analyze the behavior at the position of the filler zone centerline.

Equation 6.2 can be used in conjunction with Ni diffusivity data to estimate the interdiffusion time required for the Ni concentration at the braze centerline to be elevated by 9 at. %, *i.e.*, for interdiffusion to have as great of an effect on the composition at the centerline as dilution does. This condition is illustrated schematically in Figure 6.9(c). The required interdiffusion time to achieve this degree of homogenization depends strongly on temperature, since diffusivity (D) is governed by the Arrhenius law:

$$D = D_0 \exp\left(-\frac{Q}{RT}\right) \tag{6.3}$$

Where D_0 is an exponential pre-factor with the same units as diffusivity, Q is the activation energy, R is the gas constant and T is the absolute temperature.

Jin et al. compiled Ni diffusivity data in several MPEA systems and developed an Arrhenius law for each [86]. The documented system most closely matching the Alloy 738LC braze is NiCoFeCrMn, which has a reported exponential pre-factor of 9.5 x 10^{-4} m^2/s, and a reported activation energy of 308 kJ/mol [86]. Using these parameters, and approximating the value of h as 100 μm based on line-scans such as those in Figures 6.3 and 6.5, Equations 6.2 and 6.3 were employed to calculate the time needed to reach the homogenization condition in Figure 6.9(c). The resultant curve is plotted in Figure 6.9(d) and spans many orders of magnitude in the interdiffusion temperature range shown. Two temperatures of interest are indicated. At 1120°C, a temperature commonly employed for 2 hours as the first-step of a double-age heat treatment for Alloy 738LC [18], an estimated duration of 1430 hours is required to reach the homogenization condition in Figure 6.9(c). Hence, the extent of homogenization during this heat-treatment step is expected to be far less than the dilution-driven composition change resulting from brazing. At 843°C, the interdiffusion temperature employed in this work, the estimated duration is on the order of one million hours.

This analytical approach has several limitations. The Ni diffusivity is a function of the overall material composition in addition to temperature, and the other constituent elements do not exhibit a flat profile in the filler zone (*e.g.*, Figure 6.3), so these variations are not considered. Furthermore, the Ni diffusivity data compiled by Jin et al. is not for this specific MPEA material system and is therefore only an approximation. While the geometrical assumptions of a finite filler zone and semi-infinite base material underlying Equation 6.2 are the most reasonable of any of the analytical solutions to the diffusion equation, variations in the value of h among different braze sites are not captured in Figure 6.9(d). Extended experimental heat treatments and site-specific tracking of composition profile evolution are necessary to gain a better understanding. Nevertheless, this calculation shows that the time required for interdiffusion to compete with dilution in magnitude of composition change is likely orders of magnitude greater than the durations employed in this study, even at a high temperature of 1120°C. This finding emphasizes the magnitude of the dilutive composition change in MPEA brazes of Ni-superalloys.

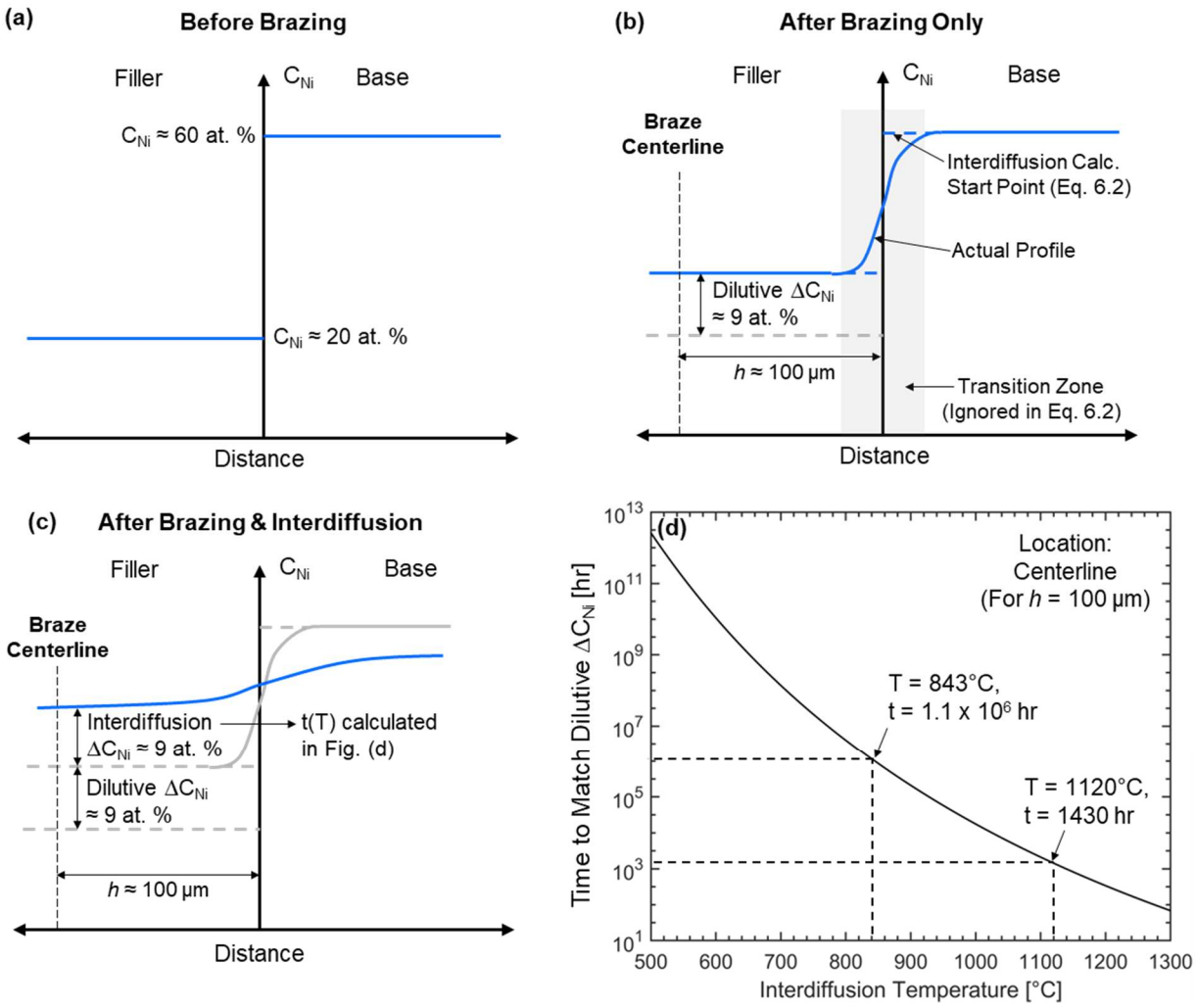

Figure 6.9: (a-c) Schematic profiles of the Ni-concentration in an Alloy 738LC braze (a) before brazing, (b) after brazing only, and (c) after brazing and extended homogenization via interdiffusion. (d) Calculated time required, as a function of temperature, for homogenization by interdiffusion to cause the same change in Ni-concentration at the braze centerline as dilution does.

6.5.2 Effect of Dilutive Composition Changes on Configurational Entropy

As discussed in Chapter 2, the postulate of a cross-cutting entropy effect that stabilizes single-phase microstructures in MPEAs regardless of constituent element identity has been largely debunked [1, 78]. Despite these conclusions, a significant subset of the community studying MPEAs has continued to focus on equiatomic compositions, citing the maximization of configurational entropy as a design objective with varying degrees of acknowledgement. This tendency is reflected by two of the leading research groups studying MPEAs as braze fillers, which both explore equiatomic compositions that require extrinsic additions of melting-point depressants. Hardwick et al. employ equiatomic NiFeCrGe with boron additions as a filler [66],

while Tillmann et al. employ equiatomic CoCrCuFeNiGa [67]. The former study acknowledges that the NiFeCrGe filler was selected "in the style of a high entropy alloy" [66], while the latter study expressly invokes the 'entropy effect' idea to justify the consideration of three equiatomic alloys, from which CoCrCuFeNiGa was selected [67].

Considering the dilutive composition changes illustrated in Figure 6.4 for the brazes studied in this work, it is especially important to critically assess entropy maximization as a filler material design objective. Regardless of the validity of the 'entropy effect' postulate, current literature does not consider that dilutive composition changes will have substantial influence on the resultant value of configurational entropy in the filler zone of a braze. A simple comparison of a few pertinent values of configurational entropy, summarized in Table 6.1, is sufficient to illustrate this point. An equiatomic quinary composition, which has configurational entropy of 13.381 J/mol*K, is generally taken as a standard definition of a high entropy alloy [146], and many studies exist on the prototypical equiatomic quinary Cantor alloy [63] and its derivatives. By deviating from the equiatomic composition, the MPEA filler employed in this work has a lower configurational entropy of 12.329 J/mol*K at the nominal composition. However, the introduction by dilution of appreciable quantities of elements not native to the initial MPEA filler increases the configurational entropy. For an Alloy 600 braze, in which Cr is the only non-native element introduced to the filler zone, the configurational entropy of the resultant composition is elevated to 13.410 J/mol*K, slightly surpassing that of an equiatomic quinary alloys. For an Alloy 738LC braze, which introduces seven significant non-native elements to the filler zone, the increase in configurational entropy is much greater, to a value of 16.057 J/mol*K.

Table 6.1: Comparison of calculated configurational entropy values for selected compositions

Composition Description	**Number of Elements**	**Calculated Configurational Entropy (J/mol*K)**
Equiatomic quinary alloy (hypothetical)	5	13.381
Nominal MPEA filler in this work	5	12.329
Measured filler zone of Alloy 600 braze (as -brazed)	6	13.410
Measured filler zone of Alloy 738LC braze (as-brazed)	12	16.057

This illustration emphasizes the idea that selection of an MPEA composition to act as a braze filler should be minimally guided by the configurational entropy of the composition. The dilutive composition change causes the resultant entropy of the as-brazed filler zone in this study to surpass that of a standard quinary alloy, despite a lower initial configurational entropy for the MPEA employed in this work. While this finding is composition-specific and not guaranteed for every potential MPEA filler, a dilutive composition change, especially when brazing compositionally complex Alloy 738LC, will usually increase the entropy of the resultant filler zone by introducing non-native elements. This idea renders moot any design objective of maximizing the configurational entropy of the *initial* MPEA filler composition, regardless of the value of this objective.

6.5.3 Critical Assessment of the Absence of TCP Phases in Alloy 738LC Brazes

The summary of the observed microstructure of the Alloy 738LC brazes presented in Section 6.4.2.2 indicates the absence of many potentially detrimental phases in detectable concentrations. Particularly, the three TCP phases common in Ni-alloy systems – σ, μ, and Laves phases [10] – are not observed. The presence of only an FCC matrix and contaminant oxide particles in Figure 6.8 indicates that all seven appreciable alloying elements in Alloy 738LC which are not native to the MPEA filler – namely Cr, Al, Ti, Mo, Ta, W, and Nb – are accommodated in the disordered FCC solid solution matrix with no intermetallic phase precipitation in the short-term. This accommodation extends to the degree at which these elements are introduced via dilution and interdiffusion (Figure 6.4b). This finding represents an important extension of the filler/substrate compatibility first demonstrated for this MPEA on Alloy 600 in Chapter 3 and earlier work [2, 3], as Alloy 600 only introduces Cr to the MPEA as a non-native element, while Alloy 738LC introduces more compositional complexity. This accommodation of base material elements in a ductile microconstituent indicates that the as-brazed ductility of the MPEA braze, demonstrated in Chapter 3 on Alloy 600 substrate, is likely to extend to Alloy 738LC brazes employing this filler. Further improvements are realizable if oxygen contamination in the MPEA production step can be mitigated.

However, the kinetics of TCP phase formation in Ni-superalloy systems are typically sluggish. Recent studies on this topic acknowledge the complexity of precipitation kinetics in superalloy systems [147, 148]. These investigations often limit their focus to the competing effects

of Re and Ru, two elements with potent influence on TCP phase formation that are often added to newer-generation superalloys, but which are not nominally included in Alloy 738LC [147, 148]. Nevertheless, Rettig et al. developed a multicomponent precipitation model to predict TCP precipitation kinetics in superalloy systems [148]. When this model was applied to a simplified Ni-12Cr-16W system at 1050°C, 1000 hours were required for the σ-phase volume fraction to reach its peak, before dissolving and being replaced by μ-phase after 10,000 hours [148].

As acknowledged in Section 6.5.1, the 843°C-24h interdiffusion heat treatment applied in this work is much shorter in duration than the typical uptime of a genuine Ni-superalloy component in industrial service between standard maintenance periods [4]. Extended heat treatments representing an appreciable fraction of a typical maintenance interval were beyond the scope of this work, and the lack of TCP phase precipitation in the conditions presented in this study does not guarantee that precipitation will never occur. Despite this uncertainty, it is possible to assess the relative ability of both the Alloy 738LC base material and the filler zone composition to suppress TCP phase formation by examining equilibrium thermodynamic predictions, like those in Figure 6.5. The same high-throughput implementation of ThermoCalc used to predict the presence of γ' can also be employed to evaluate TCP phases. While these calculations do not consider kinetics, they represent an endpoint for precipitation, and authors such as Matuszewski et al. acknowledge the value of considering thermodynamic calculations alone as a relatively simpler means of predicting TCP phase formation [147].

As discussed in Section 6.4.2.1, the only TCP phase that was consistently predicted to form in simulations was σ. Figure 6.10 shows the predicted equilibrium volume fraction of σ at 843°C and 600°C across the same composition profile as in Figure 6.5(b), with the locations of the base material, transition zone, and filler zone indicated. Recall that these zones are delineated by the transients in the Ni concentration profile as indicated in Figure 6.3(d). As shown in Figure 6.10(a), the entire filler zone is predicted to be devoid of σ-phase at equilibrium at 843°C, and this σ-free zone extends part-way across the transition zone before the σ volume fraction climbs to an average value of approximately 0.05 in the base material. A similar trend is shown in Figure 6.10(b) at a calculation temperature of 600°C. Relative to 843°C, the entire σ volume fraction profile is shifted upwards because lower temperatures are more favorable to the equilibrium formation of ordered intermetallic phases like σ. Figure 6.10(b) shows that at 600°C, the filler zone is predicted to precipitate up to about 0.01 volume fraction of σ, but the equilibrium volume fraction again rises

steeply in the transition zone to an average of approximately 0.1 in the base material. Furthermore, the points at which the profile begins to rise correspond almost exactly with the edges of the filler zone, indicating that this region has the lowest propensity for σ phase precipitation.

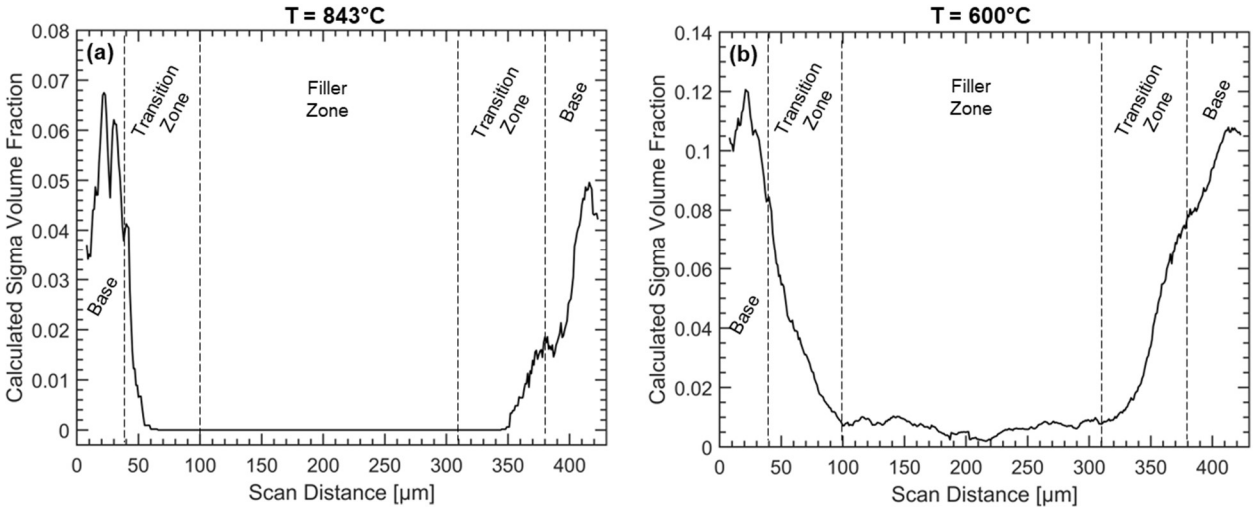

Figure 6.10: Variation of the calculated equilibrium volume fraction of σ-phase across the composition profile indicated in Figure 6.5(b), from a high-throughput implementation of ThermoCalc with the TCHEA5.1 database. (a) T = 843°C, and (b) T = 600°C. Data shown are the moving average of 15 datapoints from the EDS line scan in Figure 6.5(b).

The calculations in Figure 6.10 are a clear indicator that the MPEA filler material is predicted to outperform the adjacent base material in the suppression of TCP phases. While some σ-phase is predicted to form at equilibrium in the filler zone at 600°C, the precipitation kinetics would be slow at this low of a temperature. Extended aging experiments would be required to fully validate the conclusions from these thermodynamic predictions.

6.6 Conclusions

1. The composition change stemming from dilution during brazing of Ni-superalloys is more important to consider when employing an MPEA filler than a conventional Ni-based TLP filler due to the larger disparity in initial composition between filler and base material.
2. For brazes of Alloy 600 and Alloy 738LC subjected to the respective interdiffusion treatments of 800°C-100h and 843°C-24h, the dilutive composition change from brazing far outmatched the evolution of the composition profile stemming from short-term interdiffusion. The dilutive composition change alone represents a sufficient transit in

composition space that the microstructure of the resultant composition must be considered independently from that of the initial MPEA.

3. In the as-brazed condition, an evaluation of the microstructure of Alloy 738LC brazes indicated a γ/γ' + MC carbide microstructure in the base material and transition zone, and a γ + Al_2O_3 contaminant oxide microstructure in the filler zone. The only microstructural change engendered by heat treatment at 843°C for 24h was the precipitation of a band of Cr_2O_3 contaminant oxides in the transition zone, where both chromium and dissolved oxygen were readily available. No TCP phases were detected in the microstructural evaluations.
4. A high-throughput implementation of ThermoCalc's equilibrium module based upon quantified EDS line-scan composition data proved to be a good predictor of the presence of γ' across the braze profile. The same set of calculations indicates that the MPEA filler zone is expected to outperform the adjacent base material in the suppression of the TCP σ-phase during extended high-temperature exposure.

6.7 Chapter Acknowledgements

This research is supported by the National Science Foundation with Award No. 1847630. This research used resources of the Advanced Photon Source, a U.S Department of Energy (DOE) Office of Science User Facility operated for the DOE Office of Science by Argonne National Laboratory under Contract No. DE-AC02-06CH11357. Data was collected at Beamline 1-ID-E. Support from beamline staff was greatly appreciated. Use of the Tescan S8252G SEM was supported by the National Science Foundation Division of Materials Research Award No. 1828454. Thanks to Dr. David Diercks for his assistance with quantifying EDS spectra. Additional thanks to PCC-Structurals, Inc. for donating the Alloy 738LC material used in this work.

CHAPTER 7
CONCLUSIONS

This chapter summarizes the conclusions drawn from Chapters 3-6 as they pertain directly to the research questions presented in Chapter 1. Supplemental remarks on the implications of these conclusions to the relevance of entropy in the design of MPEA fillers are also included.

7.1 Research Questions Revisited

Research Question 1: When brazing either Alloy 600 or Alloy 738LC with the MPEA filler, how is the phase stability of the FCC solid solution affected by the *immediate* introduction of additional elements (i.e. composition-space transits) through interaction with the base materials?

When brazing either of the base materials, the immediate-term composition-space transits are primarily a result of liquid-phase dilution that occurs during the brazing process, which far outmatch the composition-space transits induced by short-term interdiffusion treatments. These dilution-driven composition changes are sufficiently large that the resultant composition of the filler zone following brazing must be considered as a unique MPEA independent from the initial filler composition. Because of the compositional complexity of Alloy 738LC, this base material introduces seven elemental species to the filler zone which are not present in the initial MPEA. Though Alloy 600 introduces only Cr, the changes in concentration of each of the original MPEA constituents are nonetheless significant.

Despite the magnitude of these dilution-driven composition changes, brazes of both Alloy 600 and Alloy 738LC retain phase stability of the ductile disordered FCC solid solution microconstituent in the immediate term, which is demonstrably reflected by the as-brazed ductility of the Alloy 600 brazes. Brazes of both base materials exhibit a multi-phase microstructure in the filler zone, but no intermetallic compounds are detected, and none of the minor phases result present from the decomposition of the solid solution.

In as-brazed Alloy 600 brazes, the filler zone includes titanium nitride, chromium carbides, and oxides of Cr, Al, and Mn. Among these, the only phases not native to the base material are the oxides. However, the introduction of these oxide phases is not inherent to the use of the MPEA filler, but rather a signature of poor environmental control during MPEA manufacturing. The

presence of the oxides is therefore the result of an engineering issue and does not constitute a falsification of the governing scientific hypothesis.

In as-brazed Alloy 738LC brazes, the filler zone was only detected to include un-melted MC carbide particles from the base material, aluminum oxides, and the FCC solid solution. The oxides represent the only phase not native to the base material, and they are present by the same mechanism as for the Alloy 600 brazes. However, both computational and experimental investigations indicated the immediate-term loss of beneficial γ' precipitates in the filler zone. This loss is an undesirable side-effect of the phase stability of the FCC solid solution.

Under rapid solidification conditions imposed by laser welding experiments, the only additional observed phase in the Alloy 738LC/MPEA filler material system was the η-phase, which is an ordered hexagonal Ni_3Ti intermetallic. However, among the investigated compositions spanning the space between these two materials, the only laser-melted composition that exhibited the η-phase was the Alloy 738LC base material itself. This finding indicates that mixing the MPEA filler with Alloy 738LC serves only to suppress the formation of η-phase under laser-melting conditions.

Research Question 2: Over *short-term* (< 100 hr) exposures to industrially relevant operating temperatures, does precipitation of any non-native phases occur in the braze microstructures? If so, by what mechanisms?

For brazes of Alloy 600, Chapter 4 provides a detailed account of the microstructural evolution during short-term heat treatments at both 600°C and 800°C for 100 hours. Non-native phase precipitation is manifest in the formation and rapid growth of new chromium oxide particles. Some growth of existing aluminum and manganese oxide particles also occurs, but the chromium oxide precipitation represents the most profound microstructural evolution. These chromium oxide particles form from the readily available chromium introduced to the MPEA filler by a dilution-driven composition change, and by the high supersaturated dissolved oxygen content stemming from MPEA manufacturing conditions. Because the chromium oxide size is not a function of distance from the specimen surface, it is believed that dissolved oxygen is the primary source for precipitation, rather than oxygen diffusing into the structure from the open-air heat-treating environment. Therefore, a dramatic reduction or complete elimination of short-term precipitation of oxide phases is expected if the MPEA filler is manufactured more cleanly.

A similar finding is presented in Chapter 6 for brazes of Alloy 738LC treated for 24 hours at 843°C; however, the chromium oxide precipitation is more regionally limited to a band which forms in the filler/substrate transition zone. This finding is reflective of the relatively higher aluminum concentration introduced to the filler by dilution when brazing Alloy 738LC. In these brazes, aluminum more effectively binds dissolved oxygen in the filler zone than in Alloy 600 brazes, and chromium oxide precipitation only occurs in the transition zone where the chromium content rises steeply. Again, this precipitation is thought to be avoidable if cleanly-manufactured MPEA filler is delivered to the Alloy 738LC brazes.

If the oxide precipitation is disregarded, the braze microstructures show relatively little evolution during short-term heat treatments. At the temperatures investigated, interdiffusion-driven composition changes are small in comparison with dilution-driven changes that occur during brazing, and simplified kinetic calculations show that homogenization is expected to require long-term exposure to high temperatures. The Mn vaporization mechanism reported in Alloy 600 brazes Chapter 4 is a notable change, but this was limited in scope to near-surface regions displaying continuous Mn segregation, and it was not observed after heat treating Alloy 738LC brazes. Of direct relevance to Research Question 2, the FCC solid solution did not display detectable decomposition or precipitation of intermetallic phases during the short-term heat treatments investigated, for brazes of either base material.

Research Question 3: To what extent can thermodynamic modelling effectively predict constituent phases of the braze microstructures, and how does it characterize the relative ability of the filler and base materials to avoid detrimental phase precipitation in the *long term*?

Thermodynamic modelling is employed as an integral part of the methodology for phase identification in concentrated alloys presented in Chapter 5. In the laser-melting experiments, a mixture of Scheil solidification and equilibrium simulations was necessary to predict the constituent phases at the compositions generated. While the experimental data did not constitute a perfect match to the constituent phase predictions, discrepancies took the form of the absence of predicted phases; i.e., there were no unexpected phases presented experimentally. The level of agreement was sufficient to show that thermodynamic simulations are effective in the construction of a system-specific diffraction library of prospective phases. Experimental synchrotron diffraction

data and supplemental electron microscopy characterizations can then be assessed against this library.

In Chapter 6, single-axis equilibrium simulations were instrumental in evaluating all the predicted microconstituents in a site-specific assessment along the Alloy 738LC composition profile. For γ', the predictions proved accurate in identifying the approximate volume fraction as a function of position. The detrimental TCP phases were also assessed in the computational work, and σ-phase was the only one that consistently occurred in simulations. Although the kinetics of σ-phase precipitation would require long-term experiments for validation, the simulations indicated that the MPEA filler is expected to outperform the Alloy 738LC base material in the suppression of σ. These results show that thermodynamic simulations, though not foolproof, represent a useful tool in microstructure prediction for MPEA fillers, and that the long-term phase stability of the FCC solid solution is predicted.

7.2 Remarks on the Relevance of Entropy Postulates in Design of MPEA Fillers

The work contained in this thesis shows that the design of MPEA compositions for use as Ni-base superalloy braze fillers is less interwoven with the 'high entropy alloy core effects' detailed in Chapter 2 than originally conceptualized. Chapter 6 explicitly explores the change in configurational entropy brought about by dilution-driven composition changes in brazes of both Alloy 600 and Alloy 738LC. The conclusion is that the extent of the composition change renders the configurational entropy of the initial MPEA filler composition irrelevant, regardless of the overall role of entropy in stabilizing solid solution phases. This finding accentuates the idea that the design of an initial MPEA filler composition, which will necessarily be constrained by properties such as melting behavior and substrate compatibility, should not be unduly constrained by the configurational entropy parameter.

The argument in Chapter 6 that dilution-driven composition changes far outmatch subsequent short-term interdiffusion-driven changes in the solid state also renders the 'sluggish diffusion' effect irrelevant to an extent. If sluggish diffusion is invoked to argue that the compositional interaction between an MPEA filler and a Ni-base alloy substrate will be limited in the filler zone itself, then the dilution-driven interaction that occurs in the liquid state renders this a moot point. If sluggish diffusion is instead invoked to argue that the MPEA filler will subsequently have limited influence on the base material in regions proximal to the repair site

during high-temperature exposure, then considering sluggish diffusion has more validity. It is desirable to avoid the migration of certain filler material elements to appreciable distances into the base material during service to avoid changing its microstructure and properties over a large area. However, an entropy-driven sluggish diffusion effect is not necessary for the MPEA filler to outperform boron-and silicon-suppressed fillers in this regard. By excluding rapid interstitial diffusers such as boron from its composition, the MPEA will inherently be slower to promote migration of non-native elements in the base material than a conventional filler. This is reflected by the absence of any clear diffusion-affected zone in brazes employing the MPEA.

The role of the severe lattice distortion postulate is also of questionable relevance when brazing precipitate-strengthened superalloys such as Alloy 738LC. Chapter 6 concludes that the MPEA filler promotes the dissolution of γ' in the filler zone. Regardless of the extent of solid-solution strengthening offered by severe lattice distortion, this mechanism is unlikely to compete with precipitate strengthening in contributing to the overall strength of the material. While the filler zone of Alloy 738LC brazes is expected to have ductile behavior, the absence of γ' nonetheless makes it likely to remain the lowest-strength region of the repaired microstructure. Rather than exploring the extent of solid-solution strengthening offered by lattice distortion, the research focus for an MPEA filler in an applied setting should instead be on means of re-introducing γ' to portions of the filler zone as a strengthening phase. This is identified as an area of future work in Chapter 8.

Chapter 2 describes the growing skepticism surrounding each of these postulates of high entropy alloys. The above arguments demonstrate that this skepticism should not be taken as cause to abandon future research directions in MPEA filler materials. Even if entropy effects are not cross-cutting, the work contained in this thesis shows that significant composition subspaces favorable to the suppression of detrimental microstructural constituents exist.

CHAPTER 8
FUTURE WORK

This thesis focuses on a constituent phase assessment of braze joints of both Alloy 600 and Alloy 738LC produced using a single MPEA as the initial filler composition. This work encompassed a transition from brazing solid-solution Ni-base alloys (e.g., Alloy 600) to more industrially relevant precipitate strengthened superalloys (e.g., Alloy 738LC), which represented an important stride in the development of the MPEA filler. Nevertheless, several areas of future work remain for scientific study, and future work is required from an industrial perspective if the MPEA is to become a viable braze alloy for practical application to real-world turbine blade repairs.

Firstly, as Chapter 4 explicitly details, the MPEA produced for experimental study throughout this work was manufactured under imperfect conditions, allowing an industrially unacceptable level of contamination of atmospheric elements. The resultant oxide inclusions convoluted the constituent phase assessment in this work in at least two ways. First, diffraction peaks stemming from the presence of oxides may mask similarly positioned peaks from other low volume-fraction microconstituents. Secondly, oxide-bound elemental species such as Cr and Al may behave differently than observed in this work in a low-oxygen alloy. Repeating a characterization similar to that outlined in Chapters 4 and 6 with brazes produced using low-oxygen MPEA would assist in deconvolving the presence of oxides.

To delve even more deeply into the constituent phase assessment for this MPEA filler than this thesis does, a transition toward a transmission electron microscopy (TEM) based characterization should be strongly considered. Synchrotron XRD was selected as the core assessment technique for this work because of its unique ability to combine site-specificity with a large assessed region, and thus map constituent phases over an entire braze and offer a comprehensive spatial account of the filler's microstructural influence. However, this characterization method may fail to detect extremely low volume-fraction phases and cannot identify the structure of specific particles observed in electron micrographs. A combination of TEM diffraction and atom probe tomography (APT) could form the basis for a project to probe the microconstituents of the brazes in this work even more rigorously. An additional means by which

to extend the thermal phase stability assessment presented in this work would be to explore accelerated aging treatments designed using an equivalent time-temperature parameter.

From the perspective of MPEA filler performance, Chapter 3 concludes that oxide inclusions in the as-brazed microstructure likely influenced tensile ductility and caused variability among individual test specimens. Chapter 4 significantly advances this idea, demonstrating that after short-term heat treatment at simulated service conditions, oxide inclusions are a key factor limiting ductility and causing inconsistent behavior. Improving the manufacturing method for the MPEA to limit atmospheric contamination should therefore be a prerequisite to any additional mechanical testing or further microstructural evaluation. This improvement may be accomplished through the implementation of vacuum induction melting or other industry-proven manufacturing techniques. While Chapter 3 concludes that the MPEA shows marked improvement in ductility over a conventional TLP filler, it is likely that the full potential of the MPEA performance has not been achieved in the work presented in this thesis and will not be realized until the material is cleanly produced.

After clean MPEA production is achieved, tensile testing such as that demonstrated in Chapters 3 and 4 should be conducted on brazes of Alloy 738LC. The constituent phase assessment in Chapters 5 and 6 rigorously demonstrates that the MPEA filler avoids introducing non-native phases to the repair site Alloy 738LC in both the immediate term and the short term. This finding indicates that the ductility of these brazes should also be significantly greater than that conventionally achieved. However, as highlighted in Chapter 6, the Alloy 738LC brazes are also free of γ', and solid solution strengthening in the MPEA braze likely cannot compensate for the loss of this strengthening precipitate. Nonetheless, the uptake of some MC carbides or other inert particles (*e.g.*, TiN) from the base material into the filler zone (Chapter 4 and Chapter 6) could offer strengthening contributions. To better assess how both strength and ductility compare to conventional brazes, tensile testing of Alloy 738LC brazed with the MPEA in its current formulation must be performed.

Due to the loss of γ', it is anticipated that some measure of modification would need to be undertaken to achieve requisite strength specifications. Guided by a suite of computational strategies developed in this and prior work, compositional alterations to the MPEA to re-introduce γ' to the filler zone microstructure could be considered. Alternatively, a change in the filler delivery method to powder/paste delivery could be employed. This change would allow particles

of the superalloy base material to be mixed with the MPEA powders in a blended ratio that would require optimization. The incorporation of base material powder that would not fully melt during the braze would introduce local γ'-strengthened microstructural regions that would improve the overall strength. Given that powder/paste delivery is common in industry, as it allows for the best conformation to as-cracked material geometries, this second alternative is desirable. Furthermore, the incorporation of base material powder with the filler in a blended delivery is already commonly employed in TLP infiltration processes (Chapter 2). However, this delivery strategy requires overcoming the additional manufacturing challenge of gas atomization for production of the MPEA in powder form, which is a highly oxygen-sensitive process due to the extensive particle surface area created.

The thermal history applied to the Alloy 738LC brazes in Chapter 6 of this work does not precisely match that which is common in industry prior to re-commissioning repaired parts. While brazes are commonly aged at 843°C for 24 hours as performed in Chapter 6, they are usually also previously subjected to a shorter aging treatment near the γ'-solvus temperature (e.g., ~ 1100°C), which was not performed. This heat treatment step is often coincident with the diffusion treatment for the application of a thermal barrier coating designed to protect the superalloy part from damage by corrosion. While the behavior reported in Chapter 6 suggests that this step will not introduce detrimental microconstituents, it will be important to verify this experimentally by conforming with the typical thermal history. This can be done prior to tensile testing brazes that use the MPEA in its current formulation.

Control of the (Mn, Cu) segregation observed in the MPEA filler zone must be more thoroughly investigated, particularly because of the Mn-vaporization mechanism reported in Chapter 4. It is desirable for the microstructure to have as little segregation as possible, so unmitigated directional solidification from the base material inward to a continuous centerline should be avoided. The incorporation of base material powder particles in the microstructure could make significant progress in preventing this, by providing more nucleation sites in the filler zone and interrupting uni-directional solidification. Microstructural examination of specimens produced via a mixed paste/powder delivery is required to verify this hypothesis.

Finally, either in parallel with or following the items above, creep and fatigue testing to provide a complete picture of the mechanical performance metrics of the MPEA braze is critical. While tensile tests will provide good baseline mechanical data, most industrial applications require

creep resistance and fatigue performance. If data in these arenas prove favorable, the ductility offered by the MPEA would render it an attractive candidate for genuine braze repairs in industry.

REFERENCES

[1] D.B. Miracle, O.N. Senkov, A critical review of high entropy alloys and related concepts, Acta Materialia 122 (2017) 448-511.

[2] M. Gao, B. Schneiderman, S.M. Gilbert, Z. Yu, Microstructural Evolution and Mechanical Properties of Nickel-Base Superalloy Brazed Joints Using a MPCA Filler, Metallurgical and Materials Transactions A (2019).

[3] B. Schneiderman, Solidification Mechanisms of a Multi-Principal-Component Alloy for Filler Applications, Department of Metallurgical and Materials Engineering, Colorado School of Mines, Golden, CO, 2020.

[4] M. Bohlin, K. Doganay, P. Kreuger, R. Steinert, M. Wärja, Searching for Gas Turbine Maintenance Schedules, AI Magazine (2010) 21-36.

[5] J.N. DuPont, J.C. Lippold, S.D. Kiser, Welding metallurgy and weldability of nickel-base alloys, John Wiley & Sons, Hoboken, N.J., 2009.

[6] F.C. Campbell, Manufacturing Technology for Aerospace Structural Materials, Elsevier Ltd.2006.

[7] S. Mannan, S. Patel, A New Ni-Base Superalloy for Oil and Gas Applications, Superalloys (2008) 31-39.

[8] S. Patel, J. deBarbadillo, S. Coryell, Superalloy 718: Evolution of the Alloy from High to Low Temperature Applications, 9th International Symposium on Superalloy 718 & Derivatives: Energy, Aerospace, and Industrial Applications, 2018, pp. 23-49.

[9] N.R. Jaladurgam, S. Kabra, M.H. Colliandera, Macro- and Micro-Mechanical Behaviour of a Gamma-Prime-Strengthened Ni-Based Superalloy at Cryogenic Temperatures, Materials and Design 209(109954) (2021).

[10] J. Belan, GCP and TCP phases presented in nickel-base superalloys, Materials Today: Proceedings 3 (2016) 936-941.

[11] A. Kracke, Superalloys, The Most Successful Alloy System of Modern Times - Past, Present and Future, TMS: 7th International Symposium on Superalloy 718 and its Derivatives, 2010.

[12] A.K. Jena, M.C. Chaturvedi, Review: The Role of Alloying Elements in the Design of Nickel-Base Superalloys, Journal of Materials Science 19 (1984) 3121-3139.

[13] Inconel Alloy 600 Technical Brochure, Special Metals Corporation, 2008.

[14] Inconel Alloy 718, Special Metals Corporation, 2007, p. Inconel 718 Manufacturer Datasheet.

[15] P. Sharma, A. Tripathy, N. Sahoo, Evaluation of surface integrity of WEDM processed inconel 718 for jet engine application Materials Science and Engineering 323 (2018).

[16] J.A. Heaney, M.L. Lasonde, A.M. Powell, B.J. Bond, C.M. O'Brien, Development of a New Cast and Wrought Alloy (Rene 65) for High Temperature Disk Applications, 8th International Symposium on Superalloy 718 and Derivatives, TMS, 2014, pp. 67-80.

[17] L.M. Pike, Development of a Fabricable Gamma-Prime Strengthened Superalloy, Superalloys (2008).

[18] Alloy IN-738 Technical Data, The International Nickel Company.

[19] R. Baldan, R.L.P. Rocha, R.B. Tomasiello, C.A. Nunes, A.M.S. Costa, M.J.R. Barboza, G.C. Coelho, R. Rosenthal, Solutioning and Aging of MAR-M247 Nickel-Based Superalloy, Journal of Materials Engineering and Performance 22(9) (2013) 2574-2579.

[20] M.A. Gonzalez, D.I. Martinez, A. Perez, H. Guajardo, A. Garza, Microstructural Response to Heat Affected Zone Cracking of Prewelding Heat Treated Inconel 939 Superalloy, Materials Characterization 62(12) (2011) 1116-1123.

[21] D.W. Seaver, A.M. Beltran, Nickel-Base Alloy GTD-222, A New Gas Turbine Nozzle Alloy, Journal of Engineering for Gas Turbines and Power 115(1) (1993).

[22] C.Y. Su, W.C. Lih, C.P. Chou, H.C. Tsai, Activated Diffusion Brazed Repair for IN738 Hot Section Components of Gas Turbines, Journal of Materials Processing Technology 115 (2001) 326-332.

[23] X. Yao, Q. Ding, X. Wei, J. Wang, Z. Zhang, H. Bei, The effects of key elements Re and Ru on the phase morphologies and microstructure in Ni-based single crystal superalloys Journal of Alloys and Compounds 629(166835) (2022).

[24] A. Harte, M. Atkinson, A. Smith, C. Drouven, S. Zaefferer, J. Quinta da Fonseca, M. Preuss, The Effect of Solid Solution and Gamma Prime on the Deformation Modes in Ni-Base Superalloys, Acta Materialia 194 (2020) 257-275.

[25] X. Huang, W. Miglietti, Wide Gap Braze Repair of Gas Turbine Blades and Vanes—A Review, Journal of Engineering for Gas Turbines and Power 134 (2012).

[26] M.E. Kassner, J.S. Tiley, Gamma/Gamma Prime Nickel Based Superalloys, Fundamentals of Creep in Metals and Alloys, Elsevier2015.

[27] W. Miglietti, A Comparison of the Mechanical Properties of Two Ni-Based Braze Alloys Containing Only B Versus B and Si as Melt Point Depressants, Turbine Joining Forum, Golden, CO, 2021.

[28] S. Rani, A.K. Agrawal, V. Rastogi, Failure analysis of a first stage IN738 gas turbine blade tip cracking in a thermal power plant, Case Studies in Engineering Failure Analysis 8 (2017) 1-10.

[29] E. Poursaeidi, M. Aieneravaie, M.R. Mohammadi, Failure analysis of a second stage blade in a gas turbine engine, Engineering Failure Analysis 15 (2008) 1111-1129.

[30] L. Witek, Failure analysis of turbine disc of an aero engine, Engineering Failure Analysis 13 (2006) 9-17.

[31] G.E. Dieter, Mechanical Metallurgy, McGraw-Hill Book Company1988.

[32] R. Viswanathan, Damage Mechanisms and Life Assessment of High-Temperature Components, ASM International1989.

[33] C.Y. Su, C.C. P., W.B. C., W.C. Lih, Plasma Transferred Arc Repair Welding of the Nickel-Base Superalloy IN-738LC, 6 (1997) 619-627.

[34] M. Prager, C.S. Shira, Welding of Precipitation Hardening Nickel-Base Alloys, Weld Research Council Bulletin 6 (1968) 128-155.

[35] X. Zhang, H. Chen, L. Xu, J. Xu, X. Ren, X. Chen, Cracking mechanism and susceptibility of laser melting deposited Inconel 738 superalloy Materials and Design 183 (2019).

[36] O. Ojo, N. Richards, M. Chaturvedi, Contribution of constitutional liquation of gamma prime precipitate to weld HAZ cracking of cast Inconel 738 superalloy, Scripta Materialia 50(5) (2004) 641-646.

[37] M. Montazeri, F.M. Ghaini, O. Ojo, Heat input and the liquation cracking of laser welded IN738LC superalloy, Weld. J 92(9) (2013) 258s-264s.

[38] K.-C. Chen, T.-C. Chen, R.-K. Shiue, L.-W. Tsay, Liquation Cracking in the Heat-Affected Zone of IN738 Superalloy Weld Metals 8(387) (2018).

[39] W.F. Gale, D.A. Butts, Overview: Transient Liquid Phase Bonding, Science and Technology of Welding and Joining 9(4) (2004) 283-300.

[40] AMS 4777 (BNi2) Technical Data, Prince and Izant Company.

[41] AMS 4778: BNi-3 Technical Data, Prince and Izant Company.

[42] AMS 4779: BNi-4 Technical Data, Prince and Izant Company.

[43] AMS 4782: BNi-5 Technical Data, Prince and Izant Company.

[44] AMS 4776: BNi-1a Technical Data, Prince and Izant Company.

[45] M. Pouranvari, A. Ekrami, A.H. Kokabi, Microstructure development during transient liquid phase bonding of GTD-111 nickel-based superalloy, Journal of Alloys and Compounds 461 (2008) 641-647.

[46] S.K. Tung, L.C. Lim, M.O. Lai, Microstructural Evolution and Control in BNi-4 Brazed Joints of Nickel 270, Scripta Materialia 33(8) (1995) 1253-1259.

[47] W. Miglietti, M. DuToit, High Strength, Ductile Braze Repairs for Stationary Gas Turbine Components—Part I, Journal of Engineering for Gas Turbines and Power 132 (2010) 082102-1 - 082102-12.

[48] W. Miglietti, M. DuToit, High Strength, Ductile Braze Repairs for Stationary Gas Turbine Components—Part II, Journal of Engineering for Gas Turbines and Power 132 (2010) 082103-1 - 082103-10.

[49] D.S. Duval, W.A. Owczarki, D.F. Paulonic, TLP Bonding – A New Method for Joining Heat Resistant Alloy Welding Journal 53(203-214) (1974).

[50] S. Liu, D.L. Olson, G.P. Martin, G.R. Edwards, Modelling of Brazing Processes that Use Coatings and Interlayers, Welding Research Supplement (1991) 207s-215s.

[51] W. Miglietti, Reduction of Boride Phases in Brazing of Gas-Turbine Components, Turbine Forum, Columbus, OH, 2022.

[52] H. Tazikeh, S.E. Mirsalehi, A. Shamsipur, Relationship of isothermal solidification completion and precipitate formation with mechanical properties of Inconel 939 joints vacuum TLP bonded by an amorphous Ni-Cr-Fe-Si-B filler alloy, Journal of Materials Research and Technology 18 (2022) 4762-4774.

[53] V. Jalilvand, H. Omidvar, H.R. Shakeri, M.R. Rahimipour, Microstructural Evolution During Transient Liquid Phase Bonding of Inconel 738LC Suing AMS 4777 Filler Alloy, Materials Characterization 75 (2013) 20-28.

[54] W.F. Gale, E.R. Wallach, Microstructural Development in Transient Liquid Phase Bonding, Metallurgical Transactions A 22A (1991) 2451-2457.

[55] Q. He, D. Zhu, D. Dong, M. Xu, A. Wang, Q. Sun, Effect of Bonding Temperature on Microstructure and Mechanical Properties during TLP Bonding of GH4169 Superalloy, Applied Sciences 9 (2019).

[56] A.D. Jamaloei, A. Khorram, A. Jafari, Characterization of microstructure and mechanical properties of dissimilar TLP bonding between IN718/IN600 with BNi-2 interlayer, Journal of Manufacturing Processes 29 (2017) 447-457.

[57] N. Sheng, X. Hu, J. Liu, T. Jin, X. Sun, Z. Hu, M3B2 and M5B3 Formation in Diffusion Affected Zone During Transient Liquid Phase Bonding Single Crystal Superalloys, Metallurgical and Materials Transactions A 46A (2015) 1670-1677.

[58] S. Shakerin, H. Omidvar, S.E. Mirsalehi, The effect of substrate's heat treatment on microstructural and mechanical evolution of transient liquid phase bonded IN-738 LC, Materials and Design 89 (2016) 611-619.

[59] O.A. Ojo, N.L. Richards, M.C. Chaturvedi, Isothermal Solidification During Transient Liquid Phase Bonding of Inconel 738 Superalloy, Science and Technology of Welding and Joining 9(6) (2004) 532-540.

[60] T. Henhoeffer, X. Huang, S. Yandt, P. Au, Fatigue Properties of Narrow and Wide Gap Braze Repaired Joints, Journal of Engineering for Gas Turbines and Power 133 (2011).

[61] C. Hawk, Wide Gap Braze Repairs of Nickel Superalloy Gas Turbine Components, George S. Ansell Department of Metallurgical and Materials Engineering, Colorado School of Mines, 2016.

[62] C.Y. Su, C.P. Chou, B.C. Wu, W.C. Lih, Microstructural characterisation of transient liquid phase zone of activated diffusion brazed nickel base superalloy, Materials Science and Technology 15(3) (1999) 316-322.

[63] B. Cantor, I. Chang, P. Knight, A. Vincent, Microstructural development in equiatomic multicomponent alloys, Materials Science and Engineering: A 375 (2004) 213-218.

[64] J.W. Yeh, S.K. Chen, S.J. Lin, J.Y. Gan, T.S. Chin, T.T. Shun, C.H. Tsau, S.Y. Chang, Nanostructured high-entropy alloys with multiple principal elements: novel alloy design concepts and outcomes, Advanced Engineering Materials 6(5) (2004) 299-303.

[65] D. Luo, Y. Xiao, L. Hardwick, R. Snell, M. Way, X.S. Morell, F. Livera, N. Ludford, C. Panwisawas, H. Dong, R. Goodall, High Entropy Alloys as Filler Metals for Joining, Entropy 23 (2021) 78.

[66] L. Hardwick, P. Rodgers, E. Pickering, R. Goodall, Development of a Novel Ni-Based Multi-principal Element Alloy Filler Metal, Using an Alternative Melting Point Depressant Metallurgical and Materials Transactions A 52A (2021) 2534-2548.

[67] W. Tillmann, T. Ulitzka, L. Wojarski, M. Manka, H. Ulitzka, D. Wagstyl, Development of High Entropy Alloys for Brazing Applications, Welding in the World 64 (2020) 201-208.

[68] D. Bridges, S. Zhang, S. Lang, M. Gao, Z. Yu, Z. Feng, A. Hu, Laser Brazing of a Nickel-Based Superalloy Using a Ni-Mn-Fe-Co-Cu High Entropy Alloy Filler Metal, Materials Letters 215 (2018) 11-14.

[69] J.-W. Yeh, Alloy Design Strategies and Future Trends in High-Entropy Alloys, JOM 65(12) (2013) 1759-1771.

[70] M.G. Nicholas, C.F. Old, Review: Liquid Metal Embrittlement, Journal of Materials Science 14 (1979) 1-18.

[71] A. Takeuchi, A. Inoue, Classification of bulk metallic glasses by atomic size difference, heat of mixing and period of constituent elements and its application to characterization of the main alloying element, Materials Transactions 46(12) (2005) 2817-2829.

[72] A. Herz, D. Wang, T. Kups, P. Schaaf, Solid-state dewetting of Au/Ni bilayers: The effect of alloying on morphology evolution, Journal of Applied Physics 116(044307) (2014).

[73] H. Okamoto, Supplemental Literature Review of Binary Phase Diagrams: Ag-Ni, Ag-Zr, Au-Bi, B-Ni, Co-Sb, Cu-Mn, Cu-Si, Cu-Zn, Fe-Zr, Li-Sb, Mg-Pu, and Si-Zr Journal of Phase Equilibria and Diffusion 39 (2018) 87-100.

[74] D. Sciti, A. Bellosi, L. Esposito, Brazing of Zirconia to Superalloy with the Active Brazing Technique, Journal of the European Ceramic Society 21(1) (2001) 45-52.

[75] M. Schwartz, Applications for gold-base brazing alloys, Gold Bulletin 8(4) (1975) 102-110.

[76] T. Zaharinie, F. Yusof, M. Hamdi, T. Ariga, R. Moshwan, Effect of brazing temperature on the shear strength of Inconel 600 joint, The International Journal of Advanced Manufacturing Technology 73(5-8) (2014) 1133-1140.

[77] A. Khorram, M. Ghoreishi, M. Torkamany, M. Bali, Laser brazing of Inconel 718 alloy with a silver based filler metal, Optics & Laser Technology 56 (2014) 443-450.

[78] F. Otto, Y. Yang, H. Bei, E.P. George, Relative effects of enthalpy and entropy on the phase stability of equiatomic high-entropy alloys, Acta Materialia 61 (2013) 2628-2638.

[79] M. Gao, Development of New High-Entropy Alloys for Brazing of Ni-base superalloys, George S. Ansell Department of Metallurgical and Materials Engineering, Colorado School of Mines, Golden, CO, 2017, p. 98.

[80] B. Schneiderman, A.C. Chuang, P. Kenesei, Z. Yu, In-Situ Synchrotron Diffraction and Modeling of Non-Equilibrium Solidification of a MnFeCoNiCu Alloy, Scientific Reports 11 (2021) 5921.

[81] J.-W. Yeh, S.-Y. Chang, Y.-D. Hong, S.-K. Chen, S.-J. Lin, Anomalous decrease in X-ray diffraction intensities of Cu–Ni–Al–Co–Cr–Fe–Si alloy systems with multi-principal elements, Materials Chemistry and Physics 103 (2007) 41-46.

[82] J.W. Yeh, Recent Progress in High Entropy Alloys, European Journal of Control (2006).

[83] B.S. Murty, J.W. Yeh, S. Ranganathan, High Entropy Alloys, Butterworth-Heinemann, San Diego, CA, 2017.

[84] K.Y. Tsai, M.H. Tsai, J.W. Yeh, Sluggish diffusion in Co-Cr-Fe-Mn-Ni high-entropy alloys, Acta Materialia 61(13) (2013) 4887-4897.

[85] E.J. Pickering, N.G. Jones, High Entropy Alloys: A Critical Assessment of Their Founding Principles and Future Prospects, International Materials Reviews 61(3) (2016) 183-202.

[86] K. Jin, C. Zhang, F. Zhang, H. Bei, Influence of Compositional Complexity on Interdiffusion in Ni-containing Concentrated Solid Solution Alloys, Materials Research Letters 6(5) (2018) 293-299.

[87] L.R. Owen, E.J. Pickering, H.Y. Playford, H.J. Stone, M.G. Tucker, N.G. Jones, An assessment of the lattice strain in the CrMnFeCoNi high-entropy alloy, Acta Materialia 122 (2017) 11-18.

[88] Tazuddin, N.P. Gurao, K. Biswas, In the quest of single phase multi-component multiprincipal high entropy alloys, Journal of Alloys and Compounds 697 (2017) 434-442.

[89] R. Sonkusare, P.D. Janani, N.P. Gurao, S. Sarkar, S. Sen, K.G. Pradeep, K. Biswas, Phase equilibria in equiatomic CoCuFeMnNi high entropy alloy, Materials Chemistry and Physics 210 (2018) 269-278.

[90] B.E. MacDonald, Z. Fu, X. Wang, Z. Li, W. Chen, Y. Zhou, D. Raabe, J. Schoenung, H. Hahn, E.J. Lavernia, Influence of phase decomposition on mechanical behavior of an equiatomic CoCuFeMnNi high entropy alloy, Acta Materialia 181 (2019) 25-35.

[91] M. Pouranvari, A. Ekrami, A.H. Kokabi, Effect of bonding temperature on microstructure development during TLP bonding of a nickel base superalloy, Journal of Alloys and Compounds 469 (2009) 270-275.

[92] Y.H. Yang, Y.J. Xie, M.S. Wang, W. Ye, Microstructure and tensile properties of nickel-based superalloy K417G bonded using transient liquid-phase infiltration, Materials and Design 51 (2013) 141-147.

[93] Y.H. Kim, I.H. Kim, C.S. Kim, Effect of Process Variables on Microstructure and Mechanical Properties of Wide-gap Brazed IN738 Superalloy, Key Engineering Materials 297-300 (2005) 2876-2882.

[94] Y.H. Kim, K.T. Kim, I.H. Kim, Effect of Mixing Ratio on Mechanical Properties of Wide-gap Brazed Ni-based Superalloy with Ni-Si-B Alloy Powder, Key Engineering Materials 306-308 (2006) 935-940.

[95] Y.H. Kim, S.I. Kwun, Microstructure and Mechanical Properties of the Wide-gap Region Brazed with Various Powder Mixing Ratios of Additive to Filler Metal Powders, Solid State Phenomena 118 (2006) 479-484.

[96] W. Hume-Rothery, H.M. Powell, On the Theory of Super-Lattice Structures in Alloys, Crystalline Materials (1935).

[97] W. Hume-Rothery, R.E.Haworth, C.W., The Structure of Metals and Alloys, The Institute of Metals London, UK, 1969.

[98] W. Hume-Rothery, Atomic theory for students of metallurgy, The Institute of Metals, London, UK, 1969.

[99] Y. Zhang, Y.J. Zhou, J.P. Lin, G.L. Chen, P.K. Liaw, Solid-solution phase formation rules for multi-component alloys, Advanced Engineering Materials 10(6) (2008) 534-538.

[100] S. Guo, C. Ng, J. Lu, C. Liu, Effect of valence electron concentration on stability of fcc or bcc phase in high entropy alloys, Journal of applied physics 109(10) (2011) 103505.

[101] A.S. Khanna, Handbook of Environmental Degradation of Materials, 2018.

[102] K.H. Song, H. Fujii, K. Nakata, Effect of welding speed on microstructural and mechanical properties of friction stir welded Inconel 600, Materials and Design 30 (2009) 3972-3978.

[103] Y.A. Alshataif, S. Sivasankaran, F.A. Al-Mufadi, A.S. Alaboodi, H.R. Ammar, Manufacturing Methods, Microstructural and Mechanical Properties Evolutions of High-Entropy Alloys: A Review Metals and Materials International 26 (2020) 1099-1133.

[104] J. He, Y. Qiao, R. Wang, Y. Tang, S. Li, X. Liu, Y. Ye, L.a. Zhu, Z. Wang, S. Bai, State and effect of oxygen on high entropy alloys prepared by powder metallurgy, Journal of Alloys and Compounds 891(161963) (2021).

[105] A. Fourmont, S. Le Gallet, K. Hoummada, M. Descoins, C. Desgranges, O. Politano, F. Baras, Effects of mechanical activation on chemical homogeneity and contamination level in dual-phase AlCoCrFeNi high entropy alloy Materials Chemistry and Physics 272(125000) (2021).

[106] I. Moravcik, A. Kubicek, L. Moravcikova-Gouvea, O. Adam, V. Kana, V. Pouchly, A. Zadera, I. Dlouhy, The Origins of High-Entropy Alloy Contamination Induced by Mechanical Alloying and Sintering Metals 10(1186) (2020).

[107] P.H. Wu, N. Liu, W. Yang, Z.X. Zhu, Y.P. Lu, X.J. Wang, Microstructure and Solidification Behaviour of Multicomponent CoCrCuxFeMoNi High-Entropy Alloys, Materials Science and Engineering A 642 (2015) 142-149.

[108] Z. Wu, H. Bei, F. Otto, G.M. Pharr, E.P. George, Recovery, recrystallization, grain growth and phase stability of a family of FCC-structured multi-component equiatomic solid solution alloys, Intermetallics 46 (2014) 131-140.

[109] S. Guo, C. Ng, C.T. Liu, Anomalous Solidification Microstructures in Co-Free AlxCrCuFeNi2 High-Entropy Alloys, Journal of Alloys and Compounds 554 (2013) 77-81.

[110] W.R. Wang, W.L. Wang, J.W. Yeh, Phases, microstructure and mechanical properties of AlxCoCrFeNi high-entropy alloys at elevated temperatures Journal of Alloys and Compounds 589 (2014) 143-152.

[111] P.D. Jablonski, J.J. Licavoli, M.C. Gao, J.A. Hawk, Manufacturing of High Entropy Alloys, JOM 67(10) (2015) 2278-2287.

[112] J.J. Licavoli, M.C. Gao, J.S. Sears, P.D. Jablonski, J.A. Hawk, Microstructure and Mechanical Behavior of High-Entropy Alloys Journal of Materials Engineering and Performance 24(10) (2015) 3685-3698.

[113] N. Choi, K.R. Lim, Y.S. Na, U. Glatzel, J.H. Park Characterization of non-metallic inclusions and their influence on the mechanical properties of a FCC single-phase high-entropy alloy Journal of Alloys and Compounds 763 (2018) 546-577.

[114] N. Choi, N. Park, J.-k. Kim, A.V. Karasev, P.G. Jönsson, J.H. Park, Influence of Manufacturing Conditions on Inclusion Characteristics and Mechanical Properties of FeCrNiMnCo Alloy Metals 10(1286) (2020).

[115] B. Schneiderman, O. DeNonno, J. Klemm-Toole, Z. Yu, Ductile Braze Repairs for Ni-Base Superalloys using Novel MPEA Filler, Welding Journal 101(3) (2022) 85-s - 95-s.

[116] S.K. Gupta, Peak Decomposition using Pearson Type VII Function, Journal of Applied Crystallography 31 (1998) 474-476.

[117] B.H. Toby, R.B. VonDreele, GSAS-II: the genesis of a modern open-source all purpose crystallography software package, Journal of Applied Crystallography 46 (2013) 544-549.

[118] C.B. Alcock, V.P. Itkin, M.K. Horrigan, Vapour Pressure Equations for the Metallic Elements: 298 - 2500K, Canadian Metallurgical Quarterly 23(3) (1984) 309-313.

[119] A. Jain, S.P. Ong, G. Hautier, W. Chen, W.D. Richards, S. Dacek, S. Cholia, D. Gunter, D. Skinner, G. Ceder, K.A. Persson, Commentary: The Materials Project: A materials genome approach to accelerating materials innovation, APL Materials 1(1) (2013).

[120] H.J.T. Ellingham, Reducibility of Oxides and Sulphides in Metallurgical Processes, Journal of the Society of Chemical Industry 63(5) (1944) 125-160.

[121] A.G. De La Torre, A. Cabeza, A. Calvente, S. Bruque, M.A.G. Aranda, Full Phase Analysis of Portland Clinker by Penetrating Synchrotron Powder Diffraction, Analytical Chemistry 73 (2001) 151-156.

[122] A.R. Yavari, J.F.R. De Castro, G. Vaughan, G. Heunen, Structural evolution and metastable phase detection in MgH –5%NbH 2 nanocomposite during in-situ H-desorption in a synchrotron beam, Journal of Alloys and Compounds 353 (2003) 246-251.

[123] F.F. Dismore, Computer Searching of the JCPDS Powder Diffraction File, Advances in X-Ray Analysis 20 (1976) 113-123.

[124] B.D. Cullity, S.R. Stock, Elements of X-Ray Diffraction, Prentice hall, Upper Saddle River, NJ, 2001.

[125] S. Gates-Rector, T. Blanton, The Powder Diffraction File: A Quality Materials Characterization Database, Powder Diffraction 34 (2019) 352-360.

[126] H.M. Rietveld, A profile refinement method for nuclear and magnetic structures, Journal of Applied Crystallography 2 (1969) 65-71.

[127] H. Gasan, E. Lökçü, A. Ozcan, O.N. Celik, I. Celikyurek, M. Ulutan, Y. Kurtulus, Effects of Al on the Phase Volume Fractions and Wear Properties in the AlxCoCrFeMoNi High Entropy Alloy System Metals and Materials International 26 (2020) 310-320.

[128] C.R. Reynolds, Z. Herl, N.A. Ley, D. Choudhuri, J.T. Lloyd, M.L. Young, Comparing CALPHAD predictions with high energy synchrotron radiation X-ray diffraction measurements during in situ annealing of $Al_{0.3}$CoCrFeNi high entropy alloy, Materialia 12(100784) (2020).

[129] R. Feng, M.C. Gao, C. Zhang, W. Guo, J.D. Poplawsky, F. Zhang, J.A. Hawk, J.C. Neuefeind, Y. Ren, P.K. Liaw, Phase stability and transformation in a light-weight high-entropy alloy Acta Materialia 146 (2018) 280-293.

[130] C.B. Dallam, B.K. Damkroger, Characterization of Welds, ASM Handbook Volume 6: Welding Brazing and Soldering1993, pp. 248-269.

[131] ThermoCalc Software: About the TCS Ni-based Superalloys Database (TCNI), ThermoCalc Software, 2022.

[132] E. Nembach, G. Neite, Precipitation Hardening of Superalloys by Ordered Gamma-Prime Particles, Progress in Materials Science 29 (1985) 177-319.

[133] A.K. Sinha, Topologically close-packed structures of transition metal alloys, Progress in Materials Science 15(2) (1972) 81-185.

[134] A.S. Wilson, Formation and effect of topologically close-packed phases in nickel-base superalloys Materials Science and Technology 33(9) (2017) 1108-1118.

[135] S. Azadian, L.-Y. Wei, R. Warren, Delta phase precipitation in Inconel 718, Materials Characterization 53 (2004) 7-16.

[136] T. Yang, Y.L. Zhao, L. Fan, J. Wei, J.H. Luan, W.H. Liu, C. Wang, Z.B. Jiao, J.J. Kai, C.T. Liu, Control of Nanoscale Precipitation and Elimination of Intermediate Temperature Embrittlement in Multicomponent High Entropy Alloys, Acta Materialia 189 (2020) 47-59.

[137] Q. Feng, T.K. Nandy, T.M. Pollock, Observation of a Ru-rich Heusler phase in a multicomponent Ni-base superalloy Scripta Materialia 50 (2004) 849-854.

[138] P. Strunz, M. Petrenec, V. Davydov, J. Polák, P. Beran, Misfit in Inconel-Type Superalloy, Advances in Materials Science and Engineering 2013(408347) (2013).

[139] D. Hicks, M.J. Mehl, E. Gossett, C. Toher, O. Levy, R.M. Hanson, G. Hart, S. Curtarolo, The AFLOW Library of Crysallographic Prototypes: Part 2, Computational Materials Science 161 (2019) S642.

[140] E.O. Hall, S.H. Algie, The Sigma Phase, Metallurgical Reviews 11(1) (1966) 61-88.

[141] T. Ida, M. Ando, H. Toraya, Extended pseudo-Voigt function for approximating the Voigt profile, Journal of Applied Crystallography 33(1311-1316) (2000).

[142] N.I. Medvedeva, D.C. Van Aken, J.E. Medvedeva, Stability of Binary and Ternary M23C6 Carbides from First Principles, Computational Materials Science 96 (2015) 159-164.

[143] J.H. Lee, C.C. Aydıner, J. Almer, J. Bernier, K.W. Chapman, P.J. Chupas, D. Haeffner, K. Kump, P.L. Lee, U. Lienert, A. Miceli, G. Vera, Synchrotron applications of an amorphous silicon flat-panel detector, Journal of Synchrotron Radiation 15 (2008) 477-478.

[144] I. Guzman, E. Granda, R. Mendez, G. Lopez, J. Acevedo, D. Gonzalez, Particle Size of Gamma Prime as a Result of Vacuum Heat Treatment of INCONEL 738 Super Alloy Journal of Materials Engineering and Performance (2012).

[145] R.W. Balluffi, S.M. Allen, W.C. Carter, Kinetics of Materials, John Wiley and Sons2005.

[146] B.S. Murty, J.W. Yeh, S. Ranganathan, High-entropy alloys, Butterworth-Heinemann2014.

[147] K. Matuszewski, A. Muller, N. Ritter, R. Rettig, K.J. Kurzydłowski, R.F. Singer, On the Thermodynamics and Kinetics of TCP Phase Precipitation in Re- and Ru- Containing Ni-base Superalloys Advanced Engineering Materials 17(8) (2015) 1127-1133.

[148] R. Rettig, A. Heckl, R.F. Singer, Modeling of precipitation kinetics of TCP-phases in single crystal nickel-base superalloys Advanced Materials Research 278 (2011) 180-185.

APPENDIX A

ALIGNMENT STRATEGIES FOR SYNCHROTRON XRD MAPPING

Braze Specimens

To construct the site-specific maps of XRD patterns on brazed specimens described in Chapter 4 and Chapter 6, it was necessary to locate the braze centerline and use it as a reference point, ideally centering the spatial map symmetrically about this location. Two strategies – (1) radiography and (2) a quick fit of the FCC solid-solution phase peaks – were employed to locate the centerline. The radiography strategy is illustrated in Figure A.1. The contaminant oxide phases, as well as some porosity resulting from brazing, appeared as visible contrast in the radiographs and served as a fiduciary mark designating the centerline.

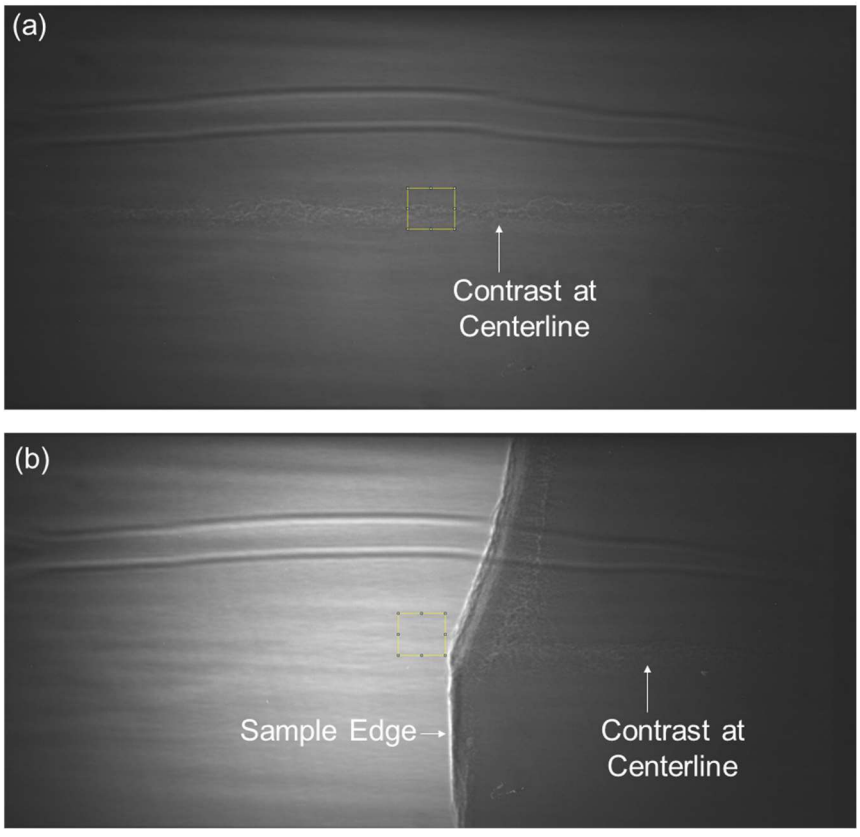

Figure A.1: Radiography images taken at (a) a laterally central location of an Alloy 600 braze coupon, and (b) the lateral edge of an Alloy 600 braze coupon. The visible centerline contrast assisted in aligning the sample and locating the braze centerline. Field of view is approximately 2mm by 1mm.

For certain braze specimens, a quick-fit strategy was employed to track the lattice parameter of the FCC (γ) solid solution, which reaches a maximum at the braze centerline. This strategy employed automated peak fitting using a pseudo-Voigt function in Matlab, which fit the FCC peaks with greater than 50% success. After quick-fitting, the results had to be filtered manually to eliminate unreasonable fits. Once this filtration was done, the lattice parameter was calculated from each scan position by averaging the calculated lattice parameter from all *hkl* peaks in the pattern, with the standard deviation from the set of *hkl* peaks representing the experimental error. This strategy created a lattice parameter profile as a function of position with error bars, as shown in Figure A.2. Scans traversing the braze profile from disparate lateral locations (see Figure 6.2) were then compared as shown in Figure A.2. For each specimen shown in this figure, the position of maximum lattice parameter (i.e., the centerline) was consistent across the lateral locations, indicating that the centerline was almost perfectly horizontal during data collection. This alignment check was essential to ensure that the patterns being averaged in the data reported in Chapter 6 were from equivalent locations with respect to the braze centerline. Sample 1 in Figure A.2 represents a case where objective of centering the scan about the braze centerline was not achieved, but the entire braze and surrounding base material is still captured in the collected data. Sample 2 in Figure A.2 displayed a scan much more symmetrical about the braze centerline.

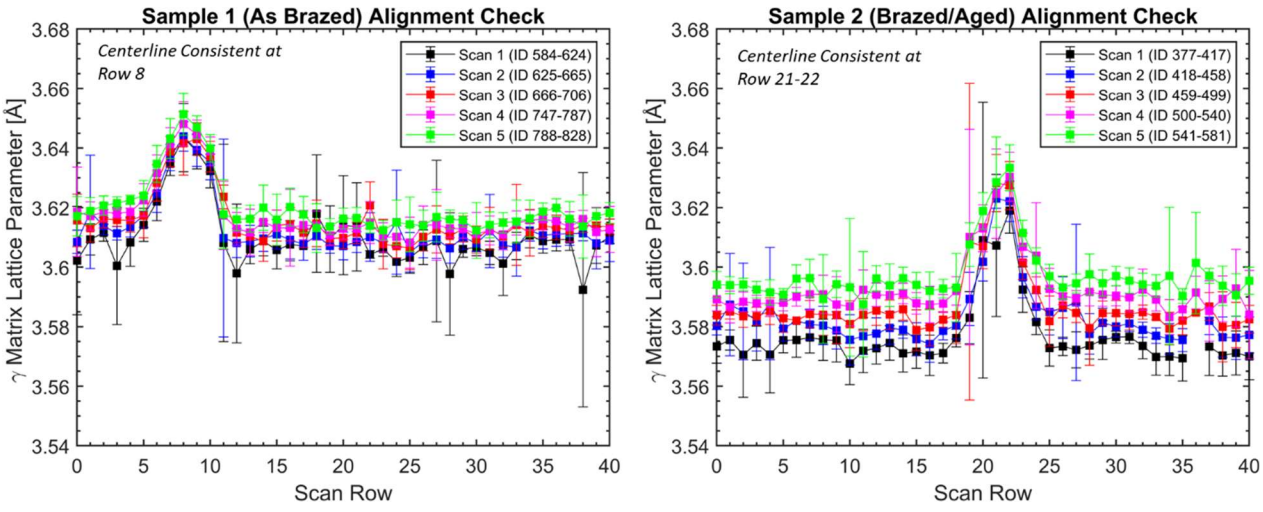

Figure A.2: Quick-fit lattice parameter calculations compared across five laterally disparate locations in an Alloy 738LC braze coupon, for two different sets of collected data. "Sample 1" represents a case in which data collection was not centered about the centerline, but data was still usable, and "Sample 2" represents a case in which data collection was nearly symmetrical about the centerline.

Laser-Melted Specimens

For the laser-melted specimens in Chapter 5 (see Figure 5.5) for geometry, the location of the original top edge of the filler material was determined via radiography before laser melting, as shown in Figure A.3(a). Following the laser-melt, this location served as the top edge for the spatial map grid imposed (see Figure 5.5), which descended 2 mm downward from this location. Material ablation caused by the laser resulted in some "blank" patterns being collected, as indicated in the radiograph in Figure A.3(b).

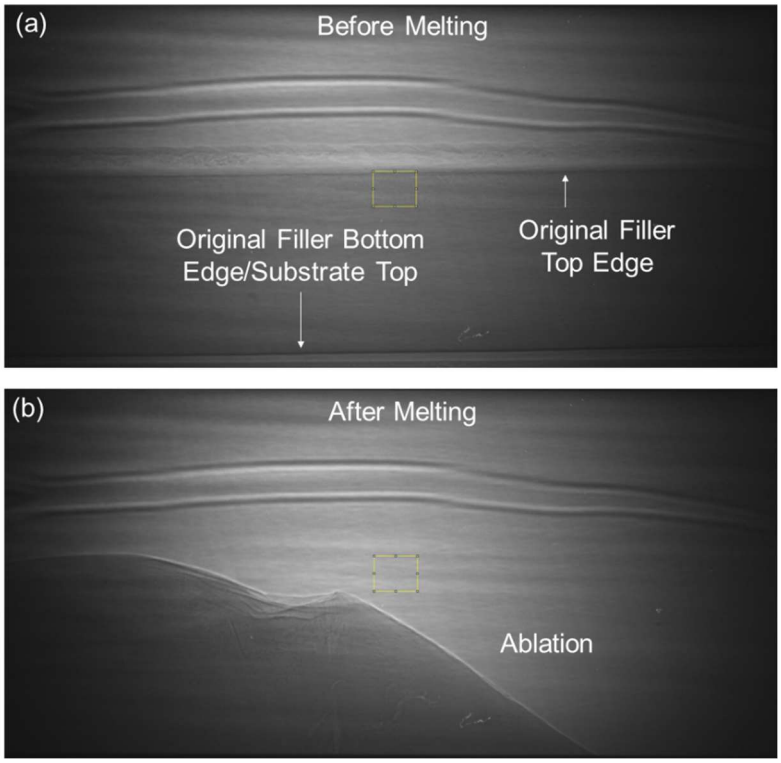

Figure A.3: Radiography images of laser-melting specimens taken at the location with the beam centered at the original top edge of the filler material. (a) Before laser melting, and (b) after laser-melting.

To assess diffraction data taken from the fully molten material as described in Chapter 5, it was necessary to map both the new upper material edge resulting from ablation, and the location at the bottom of the melt pool at which the material transitioned to being only partially melted. To effectively determine the constituent phases in the newly fabricated composition in the melt pool, it was critical to exclude patterns from partially melted material. This mapping was done by meticulously comparing individual patterns and keeping a log of their locations in space. Specifically, the three distinct types of patterns illustrated in Figure A.4 were mapped. Figure

A.4(a) shows a "blank" pattern, Figure A.4(b) shows a pattern from fully melted material, and Figure A.4(c) shows a pattern from partially melted material. As noted in Figure A.4(c), patterns from partially melted material were distinguishable by the presence of double-FCC peaks that are almost fully split. These split peaks include a broader set of peaks from molten material, and a narrower set of peaks with a slightly lower lattice parameter from un-melted base material. Fitting each peak separately and statistically analyzing the peak centers, similar to the methodology outlined for minor phases in Chapter 5, was employed to more rigorously distinguish base-material peaks from molten-material peaks, beyond the simple visual inspection of patterns like Figure A.4(c). Once a map of patterns was amassed and analyzed, the transition from patterns resembling Figure A.4(a) to patterns resembling Figure A.4(b) marked the upper edge of the material, while the transition from patterns resembling Figure A.4(b) to patterns resembling Figure A.4(c) marked the bottom edge of the fully melted zone.

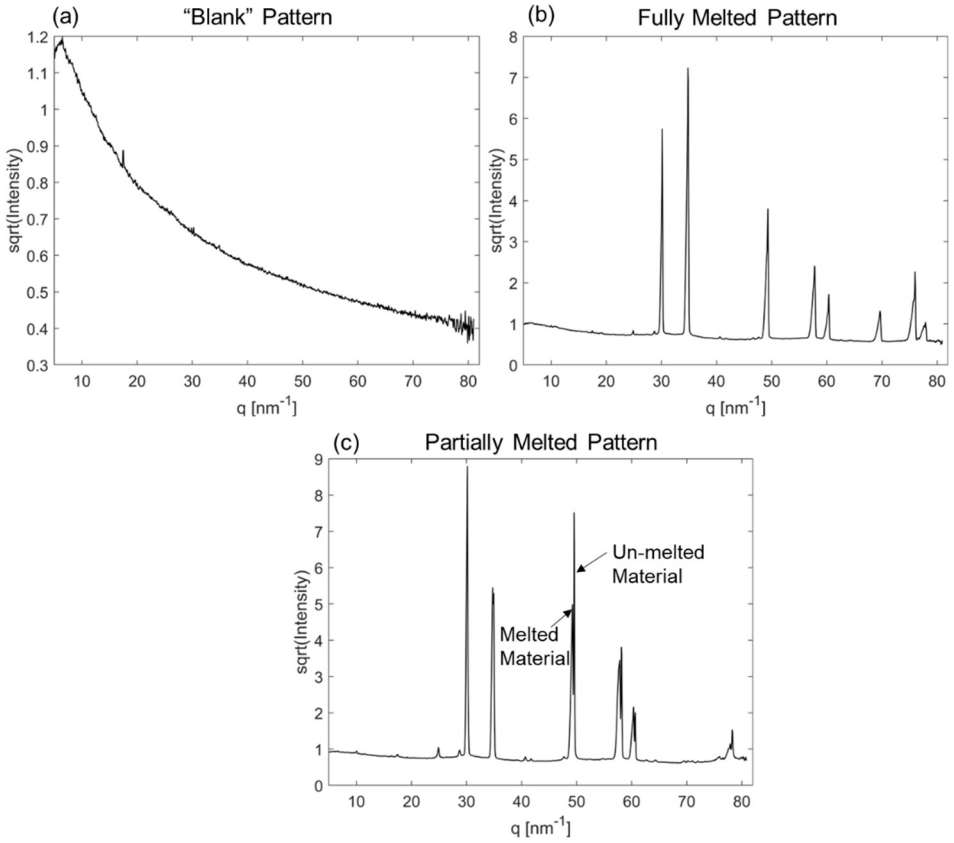

Figure A.4: Example diffraction patterns illustrating how the material edge was located after laser melting and how fully melted material was distinguished from partially melted material. (a) "Blank pattern" from ablated region. (b) Pattern from fully melted material. (c) Pattern from partially melted material with both melted and un-melted contributions to the major peaks indicated.

APPENDIX B

ADDITIONAL DIGITAL IMAGE CORRELATION DATA

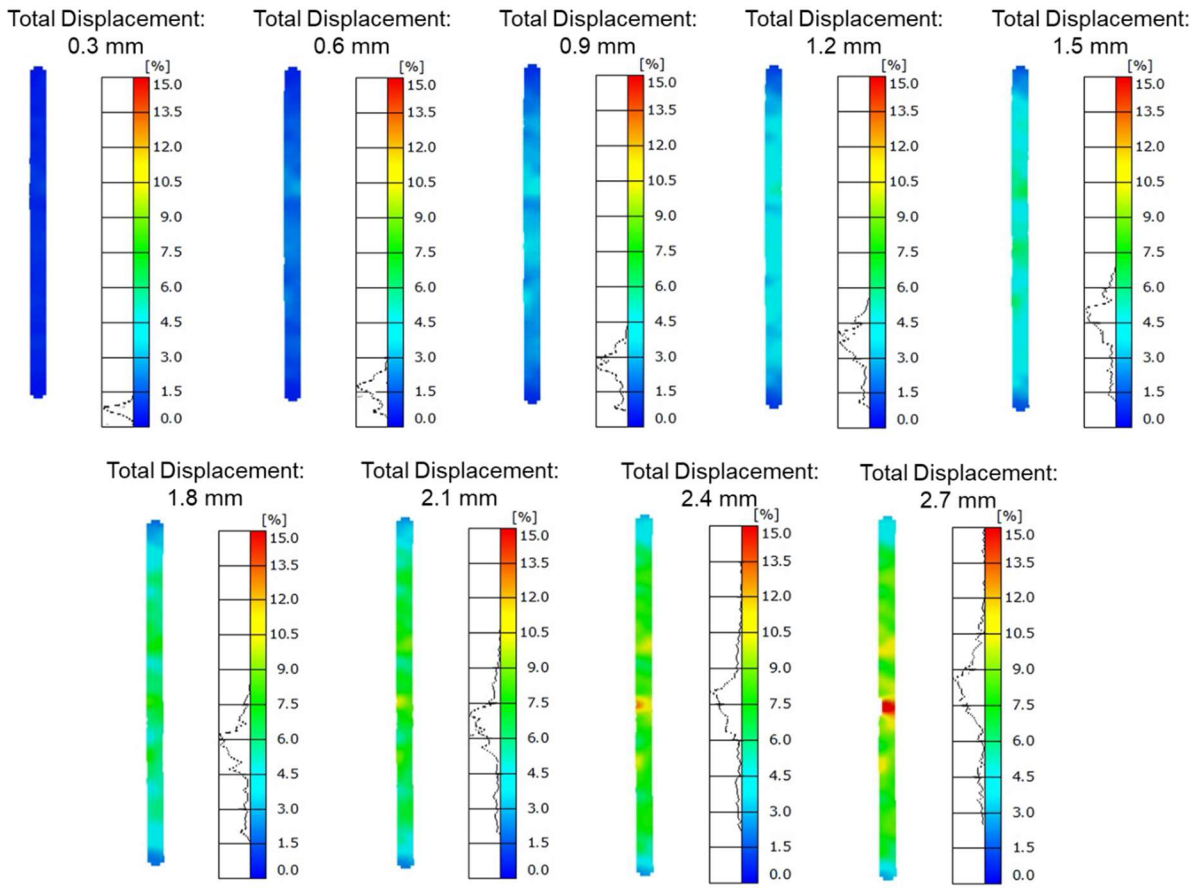

Figure B.1: Evolution of the digital image correlation map for the as-brazed specimen displaying the highest total elongation out of the room-temperature tests in Figure 3.5(a). Displacement in this figure is reported over a 30 mm gauge length. Engineering strain in Figure 3.5(a) is reported over a 10 mm extensometer gauge length encompassing the location of the braze.

APPENDIX C
COPYRIGHT PERMISSIONS

The coauthor and journal permissions for copyrighted work reproduced in this thesis are included as supplemental files.